Scanning electron microscopy investigation of bio-polymer composites morphology

A thesis submitted to the University of Sheffield in fulfilment of the requirements for the degree of Doctor of Philosophy

July 2017

Student: Quan Wan

First Supervisor: Dr C Rodenburg

Second Supervisor: Dr F Claeyssens

Content

4. Result and Discussion

List of symbols

E_0 energy of primary electron
η backscattered electron (BSE) coefficient
δ secondary electron (SE) yield
δ_{max} maximum SE yield for given material and primary energy
E_F Fermi energy
Φ work function or electron affinity
ε complex dielectric function
h Planck constant
q momentum
ω wave angular frequency
σ electron scattering cross-section
λ electron mean free path
E_I mean ionization energy
E_S stopping power
Y total electron yield
λ_m electron mean escape depth
E_{01}, E_{02} the E_0 value where $Y=1$
E_{0max} the E_0 value where Y reaches maximum
S_D electron signal strength at a given point on the detector plane
U_d SEM deceleration voltage
ϑ_D signal detection angle: angle between the incident primary beam and the straight line from emission point to detection point
ϑ_S electrons scattering angle
E_T detector energy threshold (the minimum energy that leads to a detection event which is a characteristic of the detector used)
E_{BSE}/E_{SE} electron energy of a BSE/SE when it reaches the detection point
P_{BSE}/P_{SE} absolute probability of a BSE/SE with electron energy E_{BSE}/E_{SE} landing on this detection point
U_L SEM electron landing energy

1. Summary

The development of nano-composite materials puts higher demand on morphological analysis techniques. The bio-nano-composite material systems is among the most challenging nano-composite materials for morphology characterization due to its sensitivity to damage, complex molecular conformations and nano-structures. The aim of this project is to provide a nanometer resolution and convenient chemical mapping tool based on scanning electron microscope (SEM) and electron spectroscopy for complex bio-composite systems. This would combine the backscattered electron and secondary electron techniques based on the angle-selection and energy-filtering methods. Theoretical electron behavior in the SEM is calculated using Monte Carlo simulations for reference. This SEM technique is validated and applied on representative artificial and natural bio-composite systems.

Poly(N-isopropylacrylamide) (PNIPAM) composite material is a family of widely applied temperature-responsive bio-materials. The phase separation and morphology in PNIPAM nano-composites can affect the bio-compatibility of material system. Silk fiber is a well known natural bio-material with exceptional properties as well as a model hierarchical material system. The organization of nano-repeating unit in silk is expected to be a key factor in the mechanical property formation. Direct chemical mapping of this organization was not available up to now in convenient methods. Our SEM techniques (secondary electron hyperspectral imaging, SEHI) were validated and applied for mapping of these bio-materials and provided high-resolution chemical characterization of their nano-structures.

The application of SEM techniques were further extended to different silk fibers and artificial silk materials. Such experiment validated the complex fine structure of secondary electron spectra measured on silk materials. The comparison of the electron spectra in different silk materials suggested a possible reflection of protein conformation in secondary electron spectra and this may be exploited for characterization of such complex materials in future applications.

In summary, SEM analysis technique using electron selective detection methods capable of nano-resolution chemical characterization were validated and applied on nano-bio-composite materials. These techniques show great potential for morphological analysis in complex and sensitive composite materials in the future.

2. Introduction

2.1 Introduction - analysis techniques in polymer morphological investigation

2.1.1 Morphology in polymer composite systems and requirement for analytic techniques

Polymer material systems are widely used since they have advantages in the ease of production and versatile properties. Combining the polymer system with fillers such as fibers, platelets and particles, the polymer composites could achieve properties that neither matrix nor additive phase alone can achieve [1]. The enhancement of the composite properties generally relies on parameters such as type of constituents, volume fraction of components, shape and arrangement of inclusions, and the matrix-inclusion interface[2]. Nanoscale inclusion composites[3] have been a major approach to achieving strong property enhancements due to a large matrix-inclusion interface area. However, in the study of nano-composites the dependency between properties and structures become more complicated compared to microscale composites. It has been shown that the properties of nano-composite materials do not only depend on the overall parameters such as additive fraction, but also the size, shape, distribution of local inclusion, the organization of phases from nano to micro scale and the morphology of each phase[4]. This relationship between morphology and properties is known to exist in a variety of synthetic and natural polymer nano-composite systems.

In common nano-particle composites, mechanical properties, viscoelastic behaviour and crystallinity are significantly influneced by the morphology of additives. The viscoelastic properties of composites heavily rely on a good additive-matrix interaction[5]. Thus any trend that increase this interaction such as decreasing additive size, increasing additive fraction up to ~50%, exfoliating or nano-particle-matrix cross-linking will lead to higher storage modulus[6]. Although the crystallinity of the polymer matrix, does not show significant change in overall value when changing additives/fillers, the dispersion of local crystallinity can be drastically altered. In common composites such as polypropylene/$CaCO_3$[7] and polyamide-6/Clay[8] systems, the scale of the matrix spherulites can decrease by an order of magnitude or more while the overall crystallinity value remains constant. Due to the comprehensive effect of additive-matrix interaction and matrix phase alteration caused by additives, the mechanical properties of nano-composites are heavily affected by the fraction and morphology of additives. Generally, when the

additive-matrix interaction is stronger, the elastic modulus of composite will increase in semi-crystalline materials and decrease in amorphous materials[2].

The morphology of nano-composites also plays an important role in more specific materials such as bio-compatible scaffolds[9] and organic photovoltaic (OPV) materials[10]. The bio-compatible scaffolds are commonly designed to host segregated cells or inducing substances, and support the seeding and growing of cells. Thus, these require a suitable surface morphology as well as cell-adhesive properties and relevant mechanical property. A common design in the form of nano-composites it to use additive component such as Polyglycolic acid (PGA)[11] or silk fibers[12] to reinforce the modulus and strength of scaffolds. This reinforcement relies on the composite morphology in the aspect such as orientation and lay-up of the additives in the composite scaffold[13].

The OPV materials applied in organic electronic devices such as organic solar cells often contain a bulk heterojunction of two semi-conductor components[10]. There is a difference between the energy levels of two component phases and charges are generated. The efficiency of those photovoltaic materials are defined by the charge generation and charge transportation[10], these properties are heavily influenced by the 3D nano-morphology. High charge generation and transportation properties require a finer phase separation and a continuous phase to create a pathway towards the electrode[14], thus is dependent on the fine control of nano-morphology.

The morphology, besides being important for the overall performance of composites, can also vary between different scales or structures in one material system, and this variation can further affect the material properties. An example of this type of composite systems are the hierarchical structure composites[15] such as found in natural fibers. Natural fibers adopt hierarchical structure by assembling nano-scale fibers into micro-scale structures, this structure organization show impressive mechanical performance[16]. A critical cause for this high performance is the varied components in each structure level of whole material system, with different structure covering some aspect of mechanical properties. In a natural silk, flexible disordered phases are combined with high modulus ordered phase, while in plant fibers cellulose microfibers are assembled in a multi-layer matrix structure[17]. These complex organizations of different phases from nano- to micro- scale suggest that a critical role of local morphology variation for achieving the remarkable set of mechanical properties, along with average component parameters[18].

As the morphology is very important for the performance of composite materials, many analytical techniques have been developed for the study and control of composite morphologies. In summary, in order to achieve the analytical purpose of polymer nano-composite material system morphology, there are several aspects of morphology study to cover: 1) the overall characterization of morphological parameters such as size and fraction of inclusions 2) high resolution characterization of phases' shape, distribution and composition 3) acquisition of component data from supermolecular to micrometer scale on chosen location of material sample, in 3D if necessary.

2.1.2 Vibrational spectroscopies/Microscopy

Vibrational spectroscopies are a group of analytic techniques widely applied for non-destructive material analysis. These techniques such as infra-red (IR) and raman spectroscopy probe material with light from ultra-violet to infra-red wavelength[19]. The data yielded are decided by the vibration frequency (reflected as wavenumber) and the atomic/molecular charge transfer (reflected in peak intensity) of sample material molecules. Thus information, such as chemical structures, crystallinity and molecule orientation, can be acquired depending on the location, intensity, width and polarization of the peaks yielded in vibrational spectroscopy[19].

IR spectroscopy is one of the main tools in the compositional characterization of polymer materials. Its spectrum is formed depending on the absorption bands of chemical bonds in the infra-red energy range and it is capable of both quantitative and qualitative analysis[20]. An example of quantitative IR characterization of composites is the analysis of secondary structures in silk fibroin protein[21]. Using a Fourier self-deconvolution method[22], the IR absorption band can be narrowed to resolve the amide and carbonyl vibrations determined by different hydrogen bonds. Thus the IR spectroscopy was commonly used in the measurement of secondary protein structure (β-sheet, α-helix, β-turns etc) components in silk. As the IR spectroscopy is a fast characterization tool, further application of time-resolved IR spectroscopy[23] was applied to understand the molecule conformation transitions. By collecting IR spectra with short time intervals (down to picseconds), a result data surface is formed in a time-wavenumber-intensity coordinate system. This time-resolved technique was used to understand the crystallization in spider silk and provided the insight of β-sheet formation process[24].

Raman spectroscopy, as a vibrational spectroscopy, characterizes molecule structure by measuring the molecule vibration energy. In a Raman spectrometer, laser emitted photons go through inelastic scattering processes with the sample molecules and part of the photon energy is transferred to the molecule's vibration energy[25]. The photon energy in the Raman technique can be higher than the IR technique, with energies ranging close to fluorescence and electronic absorption[19]. Raman spectroscopy also adopts the advantage of quantitative analysis of composition, conformation and orientation of polymer molecules. It is widely applied in the characterization in the field of polymer material such as silk protein.[26]

A critical disadvantage of traditional vibrational spectroscopies is their limited spatial resolution, thus more recent research conducted was focused on increasing the spatial resolution and the combination with other characterization technique. The polarized Raman/Infrared (IR) techniques can reach hundred nanometer level resolution and this "micro-spectroscopy"[27] was applied in characterization of small local area such as single fibers and carbon nanotubes. Combined with micro-tensile[28] or thermo tools[29], the transitions of molecule structure can be linked with

mechanical load or thermo processing. This "micro-spectroscopy" was applied in the understanding of mechanical property formation mechanism of many polymer fibers such as polyamide and polypropylene fibers[28].

Recently developed scanning near-field optical microscope[30] pushed the resolution of vibrational spectroscopies to tens of nanometer. Using an IR emitter and a laser-based coherent infrared continuum source, the "nano-FTIR" has been applied in the nano-scale structure mapping of polymer materials such as poly-(methyl methacrylate) and silk protein films[31]. This technique also enabled a sub-micrometer scale "hyperspectral" imaging in IR energy range[32], which was used in revealing small structures (in hundred nanometer scale) depending on its molecular conformation/orientation differences.

Despite the advantages and advancement of vibrational spectroscopies/microscopies mentioned above, there are still a few drawbacks: First, the IR/Raman techniques still mainly focus on the characterization of larger sample areas, resulting in an average data for multi-phase materials such as nano-composites. The new "nano-FTIR" sacrificed detection intensity for weaker phonon and plasmon resonances and is still not very suitable for structures below hundred nanometer. Second, the IR/Raman techniques do not provide direct visualization of local sample area on the nano-scale and do not provide topographical information. Thus when characterizing nano-structures, other microscopy techniques such as atomic force microscope to provide local information of sample is often used. Overall, the vibrational techniques provide fast and quantitative analysis of material's molecular structure, conformation and orientation, but are still not suitable for studying local structure in nano-composite materials due to limitation of resolution.

2.1.3 Atomic Force Microscopy

Atomic force microscopy (AFM), as a sort of scanning probe microscopy, is a widely applied high resolution topographical imaging technique. Unlike other scanning probe technique such as scanning tunnel microscopy, AFM is capable of imaging both conductive and insulator materials[33]. The AFM image of surface topography is formed by measuring the load on a tip scanning across the sample surface. This load is reflected in the deflection of the cantilever on which the tip is mounted. Alternatively the image can also be formed by plotting the height of the stage while maintaining a constant force between tip and sample[34].

In common situations, the cantilever system in AFM can be operated in three modes: contact, non-contact and tapping. For contact mode the tip remains in contact with the sample surface and the interaction force on the tip is monitored. This repelling force is caused by the electron clouds of the tip and sample atoms, thus contact mode is also known as repulsive mode. Constant shear force between sample and tip cause surface damage and is not preferred for soft material such as polymers[35]. The non-contact mode measures the Van der Waals force between tip and sample surface. Since the tip remains at a tens of angstrom distance of the sample surface,

the attraction force is very small, the damage to sample is minimized. Non-contact mode is preferred for soft samples but it lacks property measurement of sample surface by itself[35]. It is also sensitive to any contamination layer on the surface as the effective range of Van der Waals forces can be smaller than the thickness of contamination layer. The tapping mode applies a vibration on the tip while the tip remains a few tens of nanometer away from sample surface. The cantilever receives a change in oscillation amplitude for each sample surface irregularity in the vertical axis, thus in tapping mode AFM can plot the surface topography. Although the tapping mode can work with soft samples, there is a limitation that the surface topographical feature need to be in very small scale. Any large irregularity will cause a shear force between sample and tip, and complex shape sample can be very challenging in practice. The scale limitation of irregularity depends on the amplitude of the tip in z axis[36], which is in nanometer scale for fine structure characterization.

Since the AFM image formation is based on the force measurement on the sample, the AFM characterization techniques are commonly developed around this force measurement capability. Nanoindentation, as a major AFM based technique, is capable of mechanical testing on the nanometer scale using a diamond or silicon nitride tip[37]. Nanoindentation is widely applied in the mechanical properties measurement of semi-conductors, thin films, biological materials etc[38][39]. Its high spatial resolution enables the measurement of nano-structures in nano-composites, enabling mechanical phase identification and characterization for complex nano-composite system such as spider silk fiber[40].

Single molecule force spectroscopy is an AFM technique studying the molecular mechanism by probing the nano-mechanical properties of sample molecules. In the case of polymer composite systems, the force spectra can be measured based on the nano-mechanism such as elastic and adhesive properties of coils and chains in polymer molecules[41]. There are application of this technique in nano-composites such as to distinguish protein conformation of silk fibroin by probing the force-extension behavior of the molecule chains[42], hydrophobic effects on the protein adhesion with solid substrate[43], and β-sheet/amorphous chain cross-linking network characterization in silk filament[44].

AFM is also applied as a phase mapping tool by mapping the different interaction force between sample and tip in a nano-composite. The phase mapping mode of AFM generates a set of images based on different force on the sample surface, the mapping may yield the pattern of properties such as local compressibility and hydrophobicity [45]. The phase mapping can be more informative than normal height measurement since it plots unambiguous phase separation rather than continuous topographical change[44]. It is widely applied in the   bio-composite fields such as imaging of DNA chains[46], interaction between polysaccharides[42] and the conformation transition of spider silk in different humidity[47].

Overall, AFM techniques hold several unique advantages as a characterization tool. Both the spatial and force resolution of AFM is very high, up to sub-nanometer scale and piconewton forces. It can also provide high-resolution mechanical testing along with images. It also works with some special in-situ settings, such as imaging samples

with fluid layers or wet samples. However, due to the scanning mechanism of AFM, artifact may be introduced by contamination layers, temperature change, surface shear or complex surface topography. The AFM scanning in high-resolution also requires very small scanning steps. Along with the distance limitation of non-contact or tapping mode, the scanning of relatively large non-smooth areas or complex overall shapes can be very challenging.

2.2 Introduction - electron characterization techniques

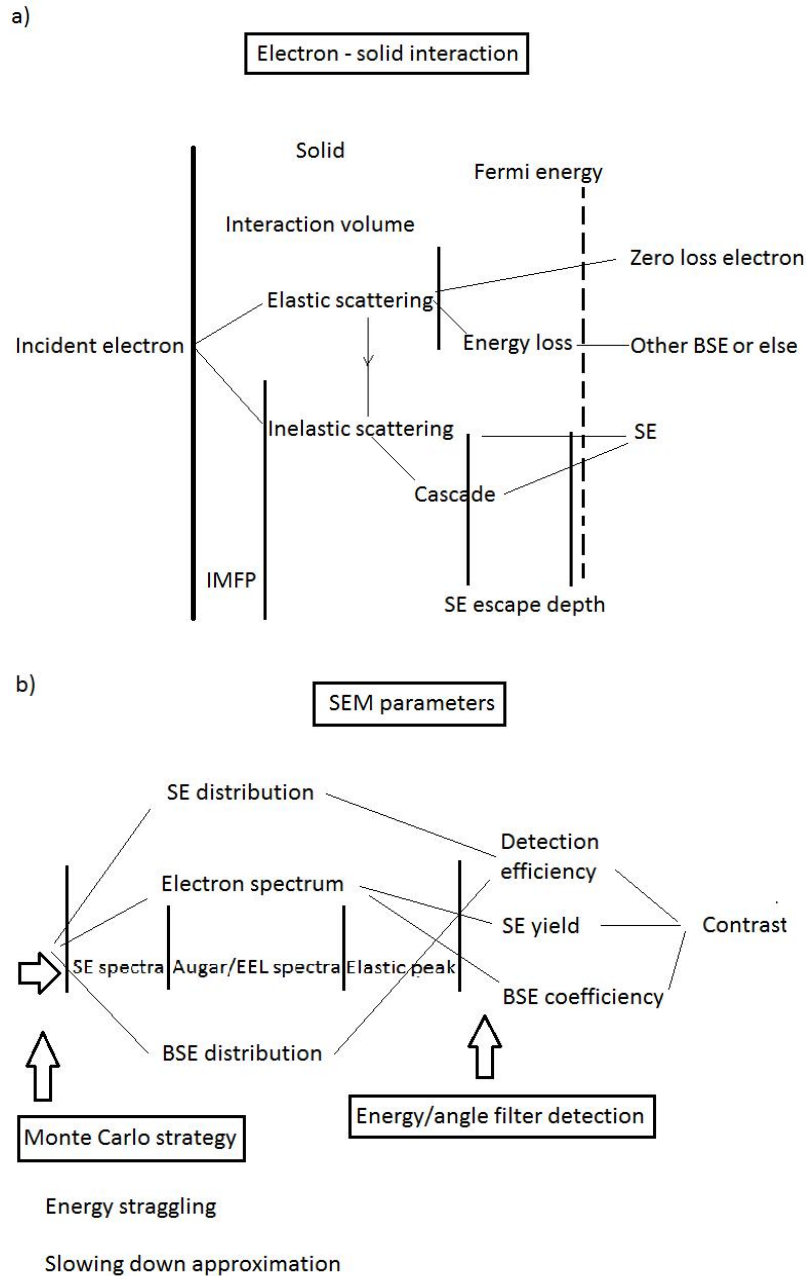### *2.2.1 Electron scattering theoretical background*

a)

b)

Figure 2.2.1: A brief schematic of the SEM image formation process and the controllable parameters for electron selective detection. The signal generation is shown in a), and the control of SEM parameter is described in b).

The SEM depends on multiple electron signal types for image formation, which are all generated from the interaction between incident primary beam with sample material as shown in figure 2.2.1. Since the electron emission of all different electron-solid interactions contribute to the whole electron signal in SEM, electrons with defined energy parameter are classed into several signal types such as secondary electron (SE). The relationship between the SEM signal and physical process is build up by solid state physic theories and relevant calculation models. In order to understand the mechanism of SEM, first we look at the electron-solid interaction briefly. The electron beam interaction with a volume of a solid sample on the scale of common material study (nanometer or larger) can be complex, but the electron emission all originates from a few types of single electron events[48]. The inelastic scattering is responsible for the emission of SE as well as some energy loss emitted in other forms. The elastic scattering is mainly responsible for the back-scattered electron (BSE) and other high-energy signals such as Auger electron (AE), but most of these signals also lose energy through interactions such as inelastic scattering.

The emission of BSE is linked to the nucleus of target atom in the solid and is usually applied for atomic number (or Z) based imaging. This interaction, elastic scattering, can deflect the incident electron with a very large angle (>90º), while having little effect on the kinetic energy of the electron due to the substantial mass difference between electron and proton/neutron[49]. The BSE can also be a result of a series of elastic scattering events with smaller deflection angles, until eventually being emitted into vacuum[50]. The BSE electron loses no, or only small amounts of energy[51], however it can suffer subsequent energy losses due to inelastic scattering when traveling through the solid, or by excitation of the system when coupling to plasmon and valence electrons is strong[52].

The most common electron signal exploited in SEM, SE, is the assembly of slow electrons emitted from inelastic scattering events[53]. Generally speaking, the inelastic scattering in SEM is an interaction event between incident electron and the electron cloud of the sample atom, in which the kinetic energy of the incident electron do not completely transfer to the scattered electron. This interaction can include electron excitation to the conductive band, electron excitation in different shells depending on atom type and plasmon excitation[54]. One or more SE may be emitted as a result of such excitation, and the low energy electron such as SE can also act as incident electron for initiating inelastic scattering with SE emission. If inelastic scattering results in more than one SE and these SE go through more scattering events (since elastic scattering of SE also produce electron in SE range, they can still be considered SE here), it is known as a cascade[55]. As a result most SE are absorbed in the solid and only SE generated close to solid surface may escape.

The electron-solid interactions are described through macro- as well as micro- scale parameters. The macro scale describes the physical behavior of a large amount of atoms or molecules, while the molecular scale here refer to the behavior of a single electron event. The macro parameters are generally summations of molecular electron behaviors. Two useful parameters for describing electron scattering are the

electron mean free path and the scattering cross-section[56]. The mean free path is the length of path an electron can travel freely in a solid before encounter a specific type of scattering event[57]. This mean free path λ shows the mobility of electron in solid and generally decreases in denser material. Since elastic scattering does not cause energy loss, inelastic mean free path is the most important parameter here. The cross-section, σ, is the area transverse to the motion of electron within which electron and atom must meet in for the scattering to happen[58]. Total cross-section is the integration of cross-section with respect to the scattering angle. Since the cross-section has a proportional relationship with scattering probability, this parameter can reflect the total electron emission/transportation[59]. For example, light atoms cause smaller elastic scattering cross-sections compared with heavier atoms as a result of fewer protons and weaker coulomb fields. The total cross-section is commonly differentiated with regards to solid angle resulting in a differential cross-section to show the angular distribution of electron emission.

As electrons travel through the solid and may eventually encounter inelastic scattering events, they lose energy and may eventually be absorbed, this is described by two other parameters. Mean ionization energy E_I is the lowest energy to initiated another inelastic scattering event[60]. If an electron has lower energy than the mean ionization energy, it is considered to be absorbed in the solid. The second parameter is the Stopping power E_S. It shows the energy loss of an electron traveling through a unit length in a solid, as consequence of the inelastic events in its path[61]. The stopping power is a summation of all excitation process initiated by the penetrating electron and can be measured through measuring the electron intensity decay in the material.

The electron scattering can be affected by many different factors, the major ones are the energy of the incident electron E_0, the density of the atom, local electron cloud and the ionization properties of the target atom. For the simplicity of calculation and interpretation, the electron scattering theory are generally derived and developed for solving situations with respect to those factors in certain limitations. For example, if we use the approximated calculation formula for high energy inelastic mean free path, it gives out lower result value when the electron energy decreases[62]. However, this trend is no longer correct when electron energy drops below ~100eV. Thus we should consider the condition of studied scattering events before adopting any particular theoretical explanation.

The material studied in this project on is polymer bio-composites, which are mainly insulating light element compounds. In this work the incident electron energy falls in range below 1keV. Most of the polymer bio-composites fall into the category of dielectric materials[63]. The fundamental parameter to quantify the responds of solid materials to external electric fields (caused by the incident electron) is the complex dielectric function ε. Which can be transformed into an energy loss function (ELF) as shown in equation 2.2.1[64].

$$\text{Im}[\frac{-1}{\varepsilon(\text{q},\omega)}] = \frac{\varepsilon_2(\text{q},\omega)}{\varepsilon_1(\text{q},\omega)^2 + \varepsilon_2(\text{q},\omega)^2} \qquad \text{equation 2.2.1}$$

This ELF describes the material's absorbing behaviour for a given energy $h\omega$ and momentum hq from an incident particle (electron in our case). $\varepsilon_1(q,\omega)$ and $\varepsilon_2(q,\omega)$ are the real and imaginary part of the dielectric function respectively. In the optical limit, where $q\rightarrow0$, the complex refractive index $n+ik$ can be measured from UV/Vis transmission spectroscopy or reflection electron energy loss spectroscopy[65]. There is relationship equation 2.2.2:

$$\varepsilon_1 = n^2 - k^2$$
$$\varepsilon_2 = 2nk$$

<div align="right">equation 2.2.2</div>

If extending the ELF measured from optical spectroscopy into a finite q region, it can be used to describe the electron behavior in the higher energy region used in electron techniques such as SEM. The ELF can then be transformed into suitable formation, with dielectric function theory using approximations and simplification accordingly[66]. The inelastic mean free path can be calculated based on equation 2.2.3:

$$\lambda^{-1}(E) = \frac{h}{a_0\pi E}\int_0^{E-E_p/h}\int_{q-}^{q+}\frac{1}{q}\text{Im}[\frac{-1}{\varepsilon(q,\omega)}]dqd\omega$$
$$q\pm = \sqrt{\frac{2mE}{h^2}} \pm \sqrt{\frac{2m(E-h\omega)}{h^2}}$$

<div align="right">equation 2.2.3</div>

The inelastic scattering cross-section can be calculated for electron electron collisions. This can be solved with a relativistic partial wave expansion method[67]. The elastic scattering cross-section is calculated by using the electron-nucleus collision. More detail is reviewed in 1.3.3.

If the electron mean free path and scattering cross-section is know, the electron generation and electron escape in the material can be simulated by computing the path of a large number of electron using Monte Carlo methods (see 1.3.2). Thus the overall electron signal can be estimated from the summation of all electrons that escaped from the solid surface.

2.2.2 Monte Carlo simulation strategy

During SEM experiments, some "classic" formulas are used to calculate the basic parameters in microscopy practice. This include the SE yield δ, BSE coeffecient η and their relationship with the primary electron (PE) energy, all of which are important for understanding the image formation in the SEM to enable correct interpretation and optimisation of the image quality. For example, the SE yield curve approached with semiempirical theory[68], can be written as an empirical equation 2.2.4.

$$\delta = 0.86\delta_{max}{}^{1.35}(\frac{E_0}{keV})^{-0.35}$$

<div align="right">equation 2.2.4</div>

δ is the SE yield
δ_{max} is the maximum SE yield for given material
E_0 is the energy of PE

Another example is the equation for a simplified SE energy distribution by Chung and Everhart[69] as shown in equation 2.2.5. The distribution is shaped by a material constant, k, Fermi energy E_f, and work function of the sample ϕ.

$$\frac{dN}{dE} = k\frac{E - E_F - \phi}{(E - E_F)^4}$$
<div align="right">equation 2.2.5</div>

These "classic" formulas generally give an estimation for a simplified situation and mostly work for homogeneous metals and high energy (over 5 keV) incident electron. They have been proven valuable for estimating and guiding standard SEM operation, and have shown the general trend of electron signal changing with simple parameters[70].

However, despite the ease of calculation, these formulas tend to break down at low energy region (below 1keV) and complex low-Z materials[71]. Solid state physics models simulation of the electron emission process has become more accessible and practical for electron microscopy researchers, thanks to the development of computing technology.

The Monte Carlo simulation is build upon the electron scattering events[72]. For elastic scattering, since the deflection process introduce very little (close to zero) energy loss, the elastic scattered electron has almost same energy as the incident electron. The energy distribution of BSE contains both elastic electrons which only depends on the incident electron energy, and other electron affected by energy loss. The energy loss can be characterized using inelastic scattering cross-sections and surface energy loss[73]. Simulation of energy loss can be done combining these parameters with the inelastic mean free path.

Thus the critical input for Monte Carlo simulation would be the inelastic and elastic cross-section, inelastic and elastic mean free path, material parameters and surface boundary parameters. In the simulations, electron will encounter scattering events based on the probability of scattering for its traveled length. All electron generated in the simulation process will end up being below the ionization energy (thus considered absorbed) or escape into the vacuum. The latter form the output of the Monte Carlo simulations in this case.

In the Low-voltage SEM (LV-SEM) these input parameters need to be valid for incident electron energies down to a few hundred eV in low-Z insulators or semi-conductors. Accordingly, the input parameters can be calculated or obtained through the following theories. The underlying math in these theories is beyond the scope of the background for microscopy application, and all the calculation detail are not reviewed below but can be found in the literature[78].

The elastic differential cross-section can be obtained through relativistic partial wave expansion method (RPWEM)[74]. In this theory, the incident electron is considered in a central electrostatic field when being deflected by an atom. The radius of this electrostatic field is up to where the atomic potential can be neglected (~2 angstrom). Such interaction is written as a Dirac equation, and solving it will enable the calculation of the phase shift of the wave. The phase shift is used for calculating the differential elastic cross-section.

The inelastic differential cross-section and IMFP can be obtained from extending the optical data beyond the optical limit[75]. The ELF can be written into a series of oscillator function, and this oscillator function can be matched with the optical loss function. The extension of ELF in energy transfer and momentum transfer plane can be made through the Ashley approximation, which will give out inelastic differential cross-section and the IMFP.

For electrons to escape into the vacuum, they can also lose energy due to surface excitation[24]. This surface loss can be represented as a surface excitation probability differentiated over energy loss. This probability is determined by the atomic number and the polarization angle of the electron surface crossing[76].

With these input data, the Monte Carlo simulation can be run through different simulation strategies[77]. In the electron straggling approach, the electron is assumed to travel in solid in a unit step length, which is determined by electron mean free path and a random number. This mean free path is calculated through the density of the atoms in the solid unit cell and the sum of total electron cross-section, which includes elastic, inelastic, polaron and phonon cross-section. For molecules the cross-section is the summated cross-section of each atom in molecule. The scattering event after this unit step length is determined by another random number and the starting parameters of the next step is calculated using the elastic or inelastic cross-section respectively. This continues until the electron reaches the surface or minimum energy (such as ionization energy). Only electrons with an energy component in direction perpendicular to the surface larger than work function (electron affinity) can escape into vacuum.

The second approach is the continuous slowing down approximation which uses a step length determined by a random number and only the elastic mean free path[25]. The energy loss events in this larger step length is covered by integrating the stopping power in this material over the step length. In this way the simulation only need to consider the elastic deflections and is much simplified. However, this method is not as accurate as the electron straggling method as a result of ignoring details of the inelastic events. Thus the result may deviate from that value obtained from the electron straggling method due to ignoring factors such as SE cascade in simulation.

For SEM applications, the Monte Carlo simulation output covers the energy and angular distribution of all electron signals including SE and BSE. This contributes to the interpretation of SE spectra and energy loss spectra[78], which can be applied for material characterization and energy filtered imaging. The electron yield for given experimental SEM settings can be predicted and utilized for contrast formation[79], interpretation and optimisation. The simulation can work for bulk solids or thin films and layered structures[80] or even more complex structures[81]. It can provide useful guidance on the formation of contrast for chosen structure[82]. These simulation outputs for SEM have shown to hold great potential, especially for complex insulating (such as bio-polymers) or semi-conductive materials[83], materials for which "classic" formulas don't work well.

2.2.3 Secondary Electron (SE) emission and the SE energy selection mechanism

As the result of the inelastic scattering of incidents electron in the solid materials, the SE can be generated by primary electron (PE) directly or by BSE or as part of the cascade in the solid material. In SEM experiments, only the electrons emitted from the sample surface with energy below 50eV are generally considered as SE signal[51]. This is not a very accurate physical definition (since SE can exceed 50eV limit), but unless specifically noted, this commonly adopted experimental definition for SE would be used in this thesis.
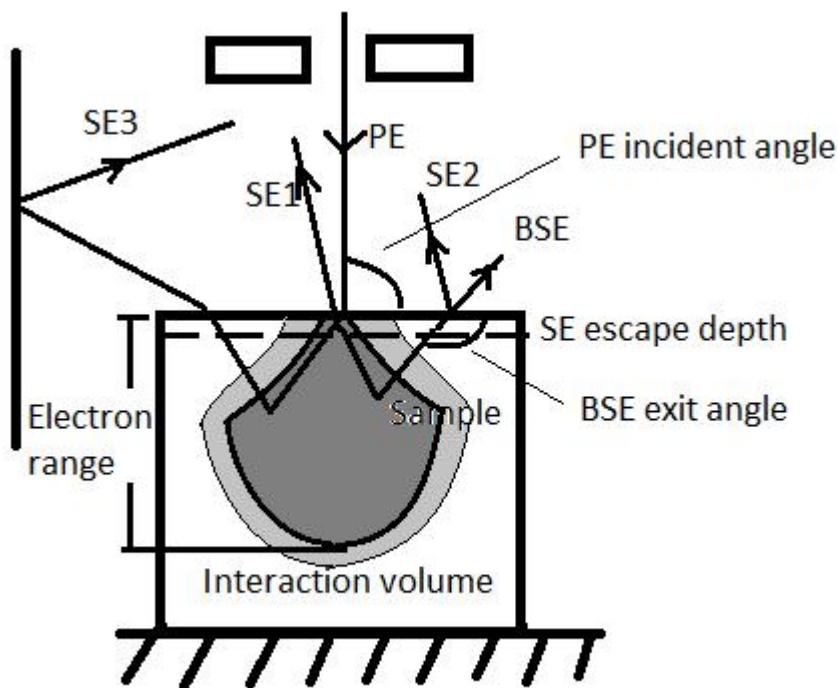

Figure 2.2.2: The schematic[45] of three possible contribution SE signal generated from PE beam hitting a sample in SEM chamber. Note not all electron emission can escape and those which cannot is absorbed in the light grey area, thus the edge of interaction volume is not a definite boundary but more a diffusion.

If we do not consider the SE cascade in its detail, in many practical applications SE can be classed as follows by their origin: 1) PE beam-sample surface layer interaction 2) BSE-sample surface layer interaction 3) BSE-chamber interaction. If we represent these three SE signals as SE1, SE2, SE3, they can be drawn in a schematic of SEM chamber in figure 2.2.2[45].
The major SE signal preferred in SEM is the SE1 signal as it stems from the surface layer since SE1 remain very close to the PE incident point, alias beam spot. Thus SE1 can provide a sub-nanometer resolution, surface dependent signal, emitted from an

angstrom scale lateral area around the beam spot. On the other hand, the SE escape depth is very small, causing the SE1 to be very sensitive to contamination[84]. The escape depth is below several nanometer even for light materials such as polymers[85]. Any contamination due to low-vacuum or beam radiation may prevent SE1 emission from the original sample surface. This can be reflected by the depth where electron emission probability drops to 1/e, SE attenuation length[86]. The value for a few common polymers are shown in table 2.2.1. This same effect also removes any potential compositional information contained in the SE signal if the sample is coated by a conductive coating. Overall the SE1 signal is most widely used for high-resolution imaging and has a complex relationship with material composition. This relationship can be exploited by filtering the SE signal by energy, which will be reviewed later. In conventional SEM applications, the separation between different SE signals is not available and image is simply formed using all SE.

Table 2.2.1 The SE attenuation length in some common polymers[86]

Material	Attenuation length (nm)
Polyethylene	4.4
Polystyrene	9.4
Polyimide	3.3
Polyamide	6.4
Polyurethane	8
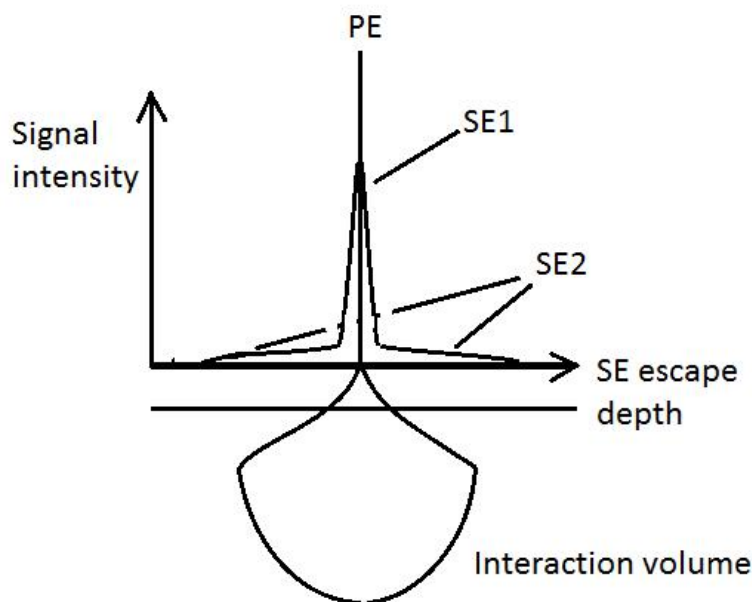
Figure 2.2.3: The schematic of SE2 reducing SE spatial resolution. The *x* axis shows the location on the sample surface and *y* axis is the signal intensity.[89]

The SE2 and SE3 are not easily separated from SE1 in common SE detection systems. Thus some researchers have reported to suppress SE2 and SE3 by absorbing BSE[87] or deflecting it with biased grid[88]. The SE2 always escape at the surface layer where the BSE exit cross-section is located. Its radius is affected by the projection radius of the

pear-shape electron interaction volume[89]. This greatly reduces the spatial resolution of the SE signal which is shown in figure 2.2.3. The resolution of the SE1 in the center is directly determined by electron spot radius which can be as small as 0.5-1nm[90]. The SE2 become much broader as is is originated from the BSE emission in larger interaction volume[91]. However, since SE2 can reflect the BSE signal, it is also useful in some situations. In such cases, SE2 signal is considered to be carrying composition information or Z-information.

As long as the signal origin is known, the SE yield is the most important parameter in imaging. The SE yield is the ratio between the number of PE and emitted SE, which represents the strength of SE signal emitted from any beam location. In turn SE yield differences form the basis for the the grey levels in SEM images.

The SE yield can be obtained by the integration (over energy & angle) of all SE emission escaped into vacuum, and as mentioned in 2.2.1, it is related to the sample material. As mentioned above the relationship is complex so it is hard to define a general trend[92]. The table 2.2.2 shows the maximum SE yield of some common insulating polymers   which are compared with some inorganic compounds in LV-SEM[93][94].

Table 2.2.2: The maximum SE yield of some common polymer insulators and inorganic compounds in LV-SEM with beam perpendicular to sample surface[93][94]

Material	Maximum SE yield	PE energy (eV)
Al_2O_3	2.6-4.7	600
SiO_2	2.1-2.9	400
NaCl	14	1200
KCl	12	1600
Polyethylene terephthalate	3.3	220
Polystyrene	3	240
Polyimide	2	200
Nylon12	2.6	250
Polymethylmethacrylate	2.3	600

For a certain material, the SE1 yield is affected by the PE energy and the incident PE angle. The SE yield reaches a maximum at a certain PE energy. The yield curve depends on the sample material, and can be approached with a semi empirical theory[95]. An estimate of δ can be made with an empirical formula as in equation 2.2.6, however most experimental values are lower than such calculated values.

$$\delta = 0.86 \delta_{max}^{1.35} (\frac{E_0}{keV})^{-0.35} \qquad \qquad \text{equation 2.2.6}$$

Models refined for polymer materials has been presented[81] but a more accurate approach is based on the Monte Carlo simulation. The preferred simulation strategy used in literature is based on the continuous slowing down model in 2.2.2 to simplify the calculation.

The incident angle dependence is the result of the small escape depth of SE. The SE,

due to its low energy, can only exit the sample and be detected as signal when emitted close to surface. Generally it is assumed the exit probability of a electron with a distance x from the surface decrease by $e^{-x/\lambda m}$, where parameter λ_m is called mean escape depth[40]. For a non crystalline material and within the SE mean escape depth, the PE can travel longer in sample at larger incident angle. As the definition of inelastic mean free path suggests, this leads to more inelastic scattering. Thus larger incident angle commonly result in larger SE yield[96].

These two factors effect SE yield also determines the SE2 yield, which is the BSE contribution towards total SE signal[97]. This contribution can be represented by a parameter β, which is a ratio between SE yield caused by unit amount of BSE and by the same amount of PE. β is ~2 for standard SEM (> 10keV) and rises to ~4 at about 5keV PE[98]. The reason for $\beta>1$ is: 1) the energy of BSE is smaller than the energy of PE, which encourage SE generation except for incident energies at ~1keV or lower[99], 2) the incident angle of BSE exiting the sample surface is smaller than incidence angle of PE unless the sample is tilted for large angle, which also raises the SE yield.

Summarizing the SE signal origin mentioned above, conclusion can be made that the information (thus image contrast) that generally applies in SEM practice as shown in table 2.2.3[100][101][102][103].

Table 2.2.3 The common SE contrast applied in SEM

Contrast type	Signal origin	Information
SE topography	SE1	Surface topography
SE material	SE2	Material Z within electron range
Channeling	SE1	Crystallography
Voltage type I	Charging	Surface potential
Voltage type II	SE spectra shift	Surface potential
Voltage type III and IV Magnetic type I, II	Deflecting electric and magnetic field	Ferro-electric domains
Dopant	SE yield due to different ionization	Dopant profile

The polymer bio-materials are commonly beam sensitive insulators, and are also likely to be semi-crystalline or amorphous. The SE topography contrast surely would meet the need for surface shape imaging, however none of the common SE contrast can provide high-resolution chemical mapping. The SE2 lacks resolution and sensitivity for similar C based composites. In order to satisfy the technical requirement for polymer bio-materials, a series of SE techniques has been developed in last two decades.

LV-SEM is using low PE energy in SEM techniques[104]. It is based on one major principle, which is the electron total yield Y relationship with PE energy E_0. The total yield is the combination of all electrons emitted from the sample surface including SE, BSE and AE. The overall shape of Y vs E_0 curve is similar to the SE yield curve as shown in figure 2.2.4, which has a maximum total yield point and two PE energies E_{01}

and E_{02} where Y=1[105]. When the total yield equals one, the number of incident electron and emitted electron reaches balance. Thus the sample at SEM setting E_{01} and E_{02} will not receive any net surface charging and can be imaged without the application of a conductive coating. This eliminates all the effects of coating in imaging, such as covering fine features and disabling compositonal imaging[106].
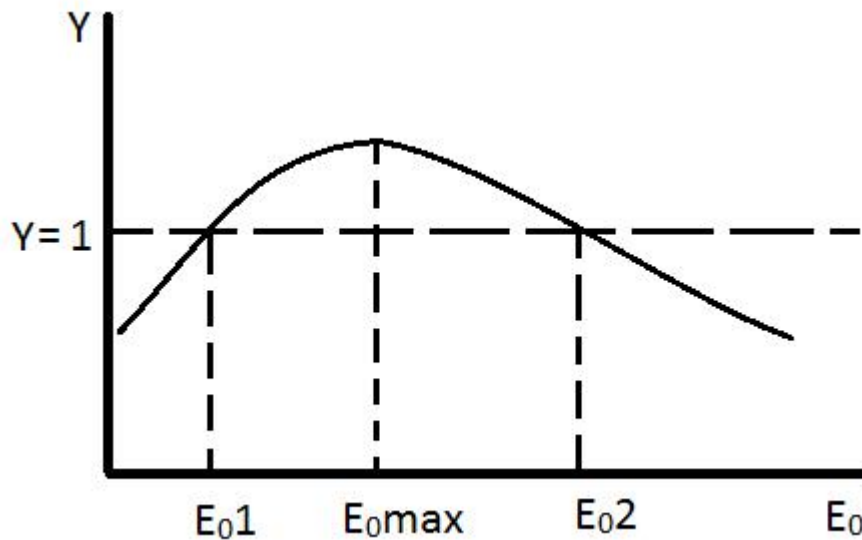

Figure 2.2.4. A schematic of total yield plot against incident electron energy, E_{01} and E_{02} are the value where total yield Y=1, E_{0max} is where σ reaches maximum value.[104]

In practice, LVSEM also show several other advantages for polymer materials. First, the E_{02} of polymers are much closer to maximum SE yield (very close to E_{0max} since δ is much larger than η in common polymer imaging) than energy region over 5keV in conventional SEM, and it is still high enough to provide high imaging resolution. The E_{02} value of a few common polymers are shown in table 2.2.4[107].

Table 2.2.4: The E_{02} value of a few common polymers[107]

Material	Measured E_{02} (eV)
Polyethylene terephthalate	900
Polymethylmethacrylate	1600
Nylon 6	1200
Polystyrene	900
High-density polyethylene	1500
Isotactic polypropylene	1400
Polyacrylonitrile-butadiene-styrene	1100
high-impact polystyrene	1300
Polycarbonate	1300
Polycaprolactone	1400
Polyethylene-vinyl alcohol	1400
Poly(ethylene-co-propylene)	1300

Second, LVSEM increases the spatial resolution the of SE signal. The electron interaction volume decreases by magnitudes when dropping PE energy from 20keV to ~1keV[108]. Thus the exit cross-section of BSE is also reduced and the emission radius of SE2 is much smaller.

Third, LVSEM may reduces the electron radiation damage on samples, this is very important for sensitive materials which includes many bio-polymers. The electron sputtering is almost eliminated in LVSEM[109]. The radiolysis is a process where an electron in material is excited by radiation, this can result in the bond breaking and degradation in organic materials[110]. It has been reported[109] that the radiation damage on some aromatics drop to unmeasurable levels when E_0 is below 1keV. While other organic materials still exhibit radiation damage, they also suffer less beam damage[109]. It has been suggested the K-shell ionization is much reduced below 1keV incident beam and this may be due to the competition between K-shell excitation and valence band excitation[110]. Thus LVSEM below 1keV will reduce charging and radiation damage as well as increase imaging resolution, which is definitely preferred for chemical characterization of polymer bio-composites.

Many of the bio-polymers are very soft materials and may contain liquid component such as water. Although such problem can be addressed in environmental SEM, high-quality images are hard to achieve in low-vacuum[111]. A widely applied technique for such requirement is the cryo-technique. The sample material can be rapidly frozen by media such as liquid nitrogen and thus retain its structure. Such cryo status can be sustained in SEM as well and it has been applied for imaging of bio-scaffolds[112], cells[113] and hydrogels[114]. The low temperature reduces the rate of beam damage[115] and is also known to affect the SE spectra, which is suspected to be related with the conformation change of polymer crystallinity[116]. It was considered very effective technique for the characterization of materials with liquid or in unstable conformation.

Building a relationship between material composition and SE signal has always been the goal for SEM techniques. The SE1 signal's high resolution make it a competitive candidate for high-resolution chemical characterization. Since this is not achieved by standard SE, there has been some attempt to filter the SE signal in SEM to isolate specific material contrast from the original complex signal[117][118]. These filter settings generally try to use a biased grid to generate different contrast. However, such settings often result in very rough bias settings up to hundreds of volts, resulting in a complex SE/BSE mixed signal[175].

The recent SE filtering based on SE energy spectrum is encouraged by the further understanding of electron scattering with Monte Carlo tools. Theoretical estimation of SE spectrum of different materials in chosen settings can provide the most suitable imaging energy region. The SE spectra, as its theoretical origin shows, is reflecting the electron, plasmon, phonon and polaron excitation in solids[119]. The electron excitation on each electron shell of an atom will absorb a specific amount of energy, thus may create a specific energy loss feature in the electron spectra long as SE1 signal is dominant. For the energy range of SE spectra it is commonly compared with ultra violet photoelectron spectroscopy[120]. Thus the SE spectra may provide a direct

insight of the atom electron cloud, which can be exploited for imaging. However, the theoretical spectra may not match experiment for complex polymer materials due to the more complicated electron excitation in such macromolecules. On the other hand, this complexity of SE spectra also provides valuable information about the bonding, crystallography and molecular conformation in polymer materials[121].

Experimentally the study on the SE energy spectrum started from early twentieth century[122], and further developed in the late twentieth century[123]. However the early SE spectroscopy was studied with special designed SE spectrometers using ultra high vacuum (UHV)[124]. This strict requirement is not met in SEM and thus can not directly instruct SEM practice. The lack of UHV in the SEM along with electron beam radiation causes commonly the presence of a contamination layer covering the sample surface. The latter can be several nanometers thick, hence exceeding the SE escape depth. Joy and Meyer[125] compared the SE spectra measured in a low-voltage SEM with the spectra recorded in UHV for single element samples and some compound materials, and obtained a reasonable match. And there have been reports on avoiding contamination effects with energy-filtered SE imaging on InP semiconductor[126].

More recently, the SE energy filter detection system applicable of high resolution composition mapping was developed[127][128]. Apart from the filter detection system adopted in one our group a "fountain detector" was suggested. This collects electron beneath the sample stage and use an electric field perpendicular to electron beam to guide electrons onto the detector. However, there is still very limited application of SE spectra collection and imaging based on it, especially in the study of SE spectra of polymers. In order to exploit the SE spectrum, the detection system is based on a through lens detector (TLD) in an immersion lens in a field immersion SEM[129]. A set of electron deflectors form part of the immersion lens pole piece, and the electron with selected energy range will be deflected towards the detector entrance as shown in schematic figure 2.2.6[130].
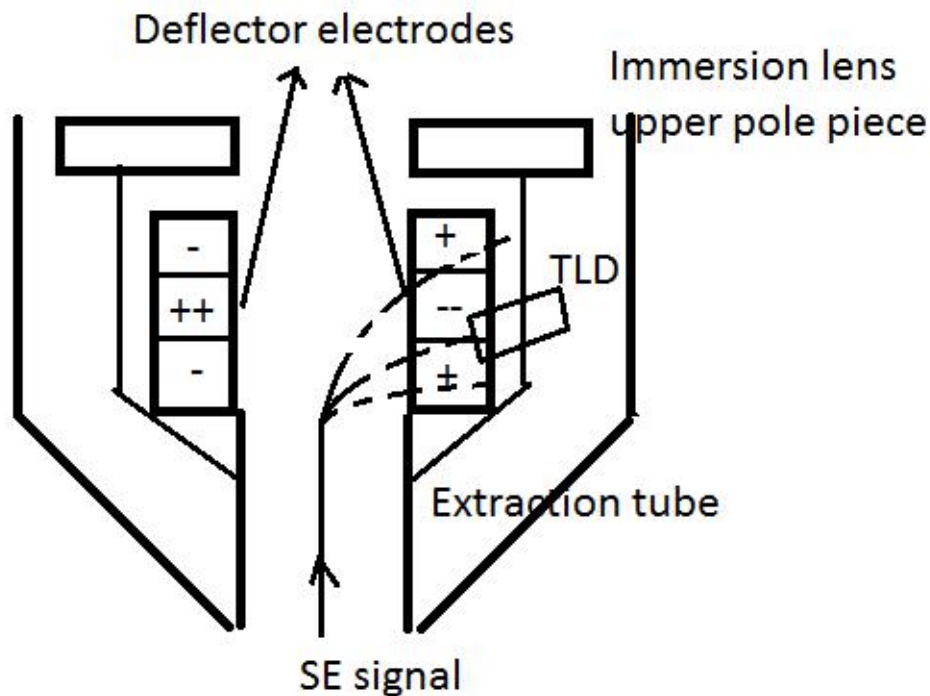
Figure 2.2.6. A schematic of SE filtering by deflector plates in an immersion lens. The SE depending on their energy (alias velocity), will hit different location in the deflection field.[130]

The detection system was investigated by tracing electron trajectories for different combinations of SE emission angle and energy[131]. These simulations showed very effective SE energy restriction for low energy selection below 10eV[72]. There is a higher detection efficiency at smaller working distance[72]. However, electron ray tracing shows larger fraction of SE3 contributes to the higher detection efficiency at smaller working distance, suggesting such signal is interrupted and not preferred for composition contrast formation. This is also suggested by the calibration of the system. The calibration is done by observing the shift of the electron spectrum with sample bias, and matching the shift on deflection voltage axis with the bias voltage applied. Ideally these two values should form a linear relationship[131], however the linear relationship only remains for lower energy region in practice. On the other hand, for insulators the majority of the peak of the SE spectrum is found below 10eV and higher energy region do not contribute much to the SE spectrum. The measured SE spectra matched the simulation (Monte Carlo) with chosen settings respectively, the Monte Carlo simulation[132] is reviewed in 2.2.2.

The choice of electron angular range and energy range also plays an important role in the elimination of contamination effects on SE spectra measurements. The inelastic mean free path (IMFP) increase for electron energies below 70~100eV (which can be calculated for common polymer materials based on ELF) and enable lower energy SE travel longer in solid, thus low-energy SE effectively have a higher escape depth compared to high-energy SE. Thus selecting low-energy SE tend to increase the SE fraction emitted from below the contamination layer[133]. The simulation shows the low energy SE are also shifted to smaller emission angle, which make using larger working distance further preferred for reducing contamination effect in SEM images.

It has been shown that the selection of certain part of low-energy SE spectrum can yield reliable composition contrast for light polymer materials as well as increase the spatial resolution[134]. Such capability gives this energy-filter technique remarkable potential for the nano-scale local chemical characterization required for the study of polymer nano-composites. However the link to paticular material properties such as local crystallinity is so far unexplored.

In order to meet the characterization requirement for our polymer nano-composite, the capability to image both the shape and chemical distribution of nano-scale features is necessary. The LVSEM already enables high-resolution topography imaging. Combining phase identification from BSE and energy-filtered SE imaging, the nano-scale chemical mapping can be obtained simultaneously and insights into the origin of the chemical SE contrast may be obtained. Thus the SEM techniques with the assistance of Monte Carlo simulation would be able to fill the gap for nano to micro-meter scale chemical characterization of polymer nano-composite, which will be explored in chapter 4.

2.2.4 *Backscattered Electron emission and angle selective mechanism*

The backscattered electron (BSE) can be divided into different groups based on the origin of electron scattering[135]. Some of BSE went through almost completely elastic scattering thus suffered little energy loss. These electrons are commonly classed as low-loss BSE (LL-BSE). Other BSE encountered inelastic scattering as part of cascade in the solid, thus lost more energy. The LL-BSE is located at the elastic peak on the electron energy spectrum (as shown in figure 2.2.7) according to its mechanism[136]. However in SEM imaging, it is generally considered to be within a certain energy range to the PE energy, and this energy range (~50eV for LVSEM setting) is much larger than the elastic peak width for practical purposes[137]. All the other electrons from 50eV to low-loss energy is considered BSE that experienced the cascade.
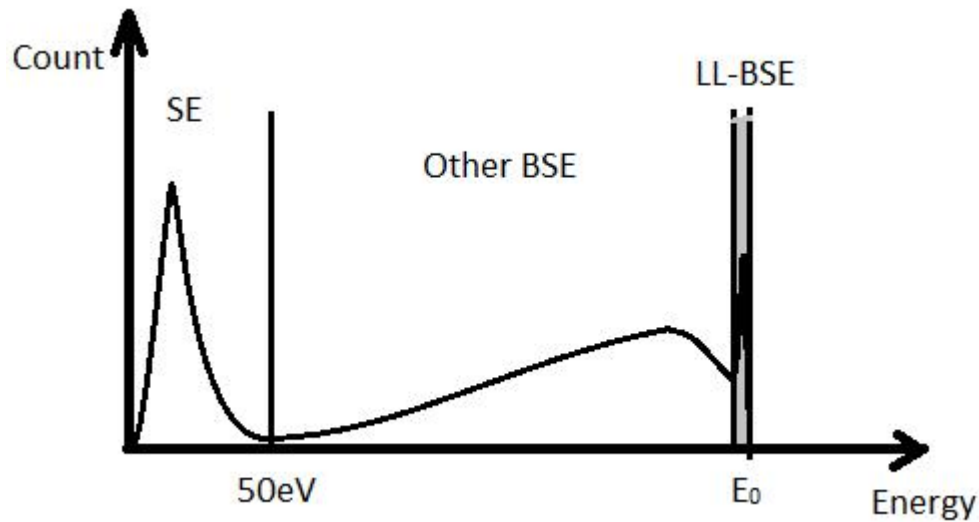
Figure 2.2.7: A schematic of an electron energy spectrum, including the SE region below 50eV, the LL-BSE at elastic peak with PE energy and other BSE with energy losses.

The energy loss of BSE is mostly applied in electron energy loss spectroscopy to acquire material information[2]. But in common SEM practice there is little quantitative control on electron energy detected, and BSE is generally divided into two groups: BSEI and BSEII, which have difference in electron energy and scattering angle[138]. Considering all the BSE signals, they can be emitted from a much larger volume of the sample compared to SE and this BSE escape volume is approximately half of the electron interaction volume[139]. Thus BSE signal in SEM can go through very different path length before being emitted. The BSE can be classed into BSEI and BSEII based on this as shown in figure 2.2.8. The BSEI are the electrons has only gone through very short length and single elastic scattering before being emitted into vacuum. The BSEI signal mostly emit at large scattering angle ϑ_S. The BSEII, on the other hand, are the electrons that have gone through a large amount of elastic scattering and are emitted from deep within the sample and also their emission is distributed in smaller ϑ_S region[140]. The BSEII suffer from energy losses as they travel through the material see 1.3.1. Thus in its nature, BSEI are mostly LL-BSE while BSEII are other BSE[141].
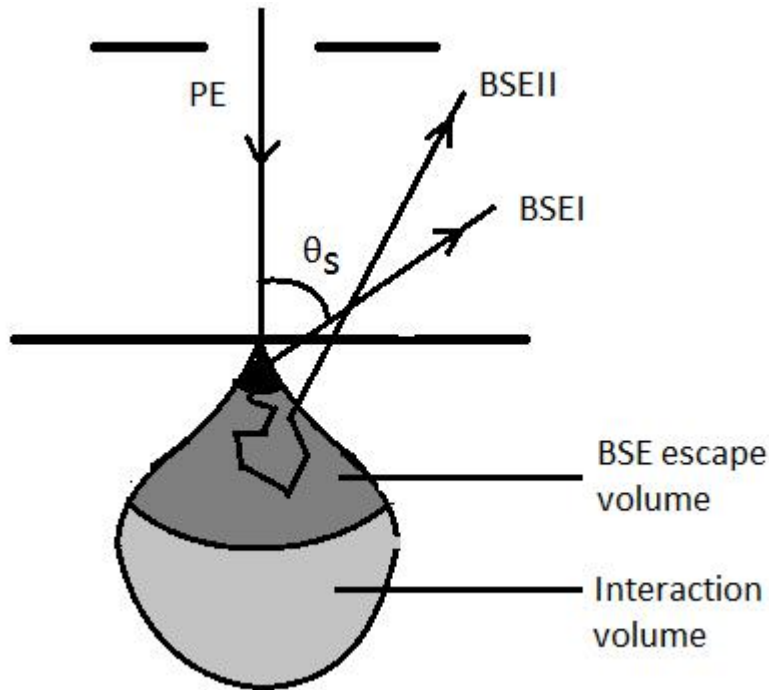
Figure 2.2.8: A schematic of BSEI and BSEII signal emission from a solid sample in SEM, the BSEI can be emitted from the black region close to surface, while BSEII can be emitted from the whole BSE escape depth. This escape depth forming a volume shown in dark grey. The angle between incident PE and electron signal is the scattering angle ϑ_S.

BSE imaging is considered a standard elemental and hence chemical characterization technique in common SEM[142]. However, this is very much simplified from the BSE signals mentioned above. The BSEI, according to elastic scattering theory, should be very much Z-based signal, but it is also very topography-sensitive due to small emission depth[143]. The BSEII is a rather complex signal, but it will reflect the chemical composition (rather than just Z number) of the sample based on energy loss mechanism[144].

Since BSEI and BSEII have largely different emission depth, their respective collection would be influenced differently by surface topography. The BSEI are highly sensitive to surface roughness, while the effect on BSEII depends on the scale of roughness. For example, when the incident electron energy is 1keV, the emission depth of BSEII in amorphous C is about 70nm (which is similar to common polymer materials) and most BSEI emission is from first 5nm layer below the surface. Thus in the case of our example situation, if the composition of the first 70nm below the surface is homogeneous in the axis perpendicular to electron beam, the surface roughness has little effect on BSEII signal. On the other hand, if there is phase separation in this 70nm thick layer, the BSEII signal will form contrast according to the thickness variation of each phase created by the roughness.

The simplified idea of BSE Z-contrast is only effective for heavy elements (especially heavy metals) in high energy region (>5keV)[145]. This is reflected by the trend of BSE

coefficient plotting against incident electron energy. BSE coefficient η is the ratio between BSE emission number and incident electron number, and it is used to quantify the BSE emission. For heavy elements such as Cu or Au, the BSE coefficient increases with incident electron energy, and the trend is very rapid <1-1.5keV. For light elements such as C or Al, the BSE actually drops very quickly in this low-energy region. This lead to a certain incident electron energy where below this energy the heavy element will yield lower BSE coefficient than light element. Thus contrast inversion between different components in LV-BSE is a common situation[146]. Therefore, BSE contrast interpretation becomes complicated for polymer materials as a low PE energy is required. In polymer systems, almost all elements are very light ones and the primary electron energy is limited to <5keV. As the BSE coefficient does not have a simple relationship with material Z number anymore, the complex BSE signal needs to be separated to provide valid information about the sample.

To study polymer systems, the BSE signal can be separated and selected based on its energy or emission angle. Both of these parameters can be linked with the information depth[147] of the BSE signal. These selective BSE imaging techniques have been applied to challenging samples for which conventional BSE techniques are unsuccessful. This includes the measurement of thin layered structures[148], chemical characterization of cells[149], high-resolution topography imaging[150] and 3D-composition mapping[151].

The energy-filtered BSE (EF-BSE) technique is build upon the energy spectrum of electrons. Just like the filtered SE technique, in the EF-BSE one selects a certain BSE energy range to form specific image contrast[152]. Common EF-BSE system use a high-pass strategy, filtering off low energy electrons by applying a retarding bias[153]. Recently EF-SEM is mainly applied for forming LL-BSE images[154][17][16]. The LL-BSE, as mentioned above, have the advantage of being Z or density -responsive (especially for heavy materials) and have a high spatial resolution. There are also reports on LL-BSE responding to the material electron bonding[155] but this application has not been commonly applied in light elements such as polymers yet. The resolution of LL-BSE is commonly below 5nm and can even be comparable to that of the SE signals[156]. In contrast the conventional BSE resolution is in the level of tens of nanometres for polymers even in LVSEM[157]. The LL-BSE is also applied for high resolution topography imaging for its sensitivity to sample shape, which is a result of small emission depth[158].

Despite the advantages, the LL-BSE image has some difficulty with imaging of complex polymer composite systems. First, the polymer system commonly do not exhibit much differences in Z number between components and LL-BSE may not reflect such small Z differences. Second, many polymer composite systems are not flat surfaces but may form complex shape like scaffolds, networks or fibers, often on the nano-scale. This can cause confusion between chemical contrast with topography contrast creating difficulties for identification of chemical differences.

The BSE with energy losses is not as popular as the LL-BSE in EF-BSE imaging. This energy region could potentially be utilized using the characterization principle of energy loss spectroscopy. However this energy region is rather large and its

characterization for polymer system in experimental SEM situation can be challenging. Although some spectrometers has been developed[159], the energy resolution required is not fully fulfilled throughout the spectrum.

The angle-selective BSE is another BSE technique that utilize the angular distribution of BSE to select the preferred signal. It is done by setting up a detector located at a specific emission angle (for large angle detection)[160], or in the form of a concentric ring detector at the end of electron column[161]. If all of the detection rings can form images simultaneously, each ring would correspond to a selected angular range. Such an angle-selective detection scheme cannot achieve high angular resolution. The latter is limited by the width of detector rings, and the signal percentage in angular range of each detector ring would be too low for very small angle range. The mechanism of BSE selection in angular selection is similar to EF-BSE. The BSEI and BSEII have different angular distributions. BSEI are mostly emitted at very large emission angle above 70°, while BSEII generally yield a broad distribution centered around 40-50$^{o[162]}$. Thus adjusting the detector location can conveniently achieve a BSEII or BSEI dominated BSE signal.

As the BSEI mainly consist of LL-BSE, the large angle BSE imaging has very similar advantage and disadvantage of LL-BSE. The BSEII, despite its complex origin, can be applied to cover the chemical characterization of polymer systems. As reviewed in electron stopping mechanism, the electron energy loss depends on many factors such as atom type, atom density, material ionization properties (see 2.2.1). Although the atoms in polymer components are very similar, different structures and bonding in polymer system affects the ionization properties in each phases. Thus different crystallinity, conformation, density and bonding will all have an effect on the coefficient of BSEII. This in turn will form contrast between different components in polymers. This contrast an only be understood by combining experimental results with Monte Carlo simulation for given materials as demonstrate in 4.1.2. Considering that the BSEII are not sensitive to surface inclination due to their much deeper emission depth (tens of nanometers for polymers in LVSEM), the image formed by selective BSEII can provide the composition contrast of polymer composite systems.

2.3 Introduction to polymer material systems investigated

As reviewed in section 1.3 and 1.4, there are SEM techniques that may fulfill the polymer composite chemical characterization requirements. Energy filtered SE technique and angle selective BSE technique combined with Monte Carlo simulation was applied for high-resolution chemical mapping on sensitive and insulating bio-polymer systems in chapter 4 respectively. In this project a few representative bio-polymer nano-composite system was selected to verify and apply our SEM techniques. This include a synthetic bio-polymer composite system Poly(N-isopropylacrylamide)/Poly(ethylene glycol) diacrylate nano-composite and natural biological polymer system silkworm and spider silks.

2.3.1 Synthetic polymer - PNIPAM/PEGDA composite

Poly(N-isopropylacrylamide) (PNIPAM) is one of the most commonly studied thermo-responsive polymer materials, and is a representative material for the "smart" polymer family[163]. The key feature of its "smart" property is at a critical temperature a miscibility gap appears in its aqueous solution. PNIPAM solutions rapidly de-mix upon exceeding this lower critical solution temperature (LCST)[164]. The steeply reduced solubility enables direct control on the hydrophobicity of the material system. The LCST of PNIPAM is around 31°C[165], which is very close to room temperature and human body temperature. This made it a suitable thermo-responsive material to be applied in bio- and medical material system. The phase separation at LCST for PNIPAM is known to be affected by the molecular mass, chain tacticity, end group and chain architecture and will adopt two different types accordingly[24]. Thus its de-mixing property can also be tuned through controlled polymerization for the best overall performance.

PNIPAM is always processed into composite systems for better performance in bio-material systems. This involves the co-polymerization[166], cross-linking[167], grafting[168] with other polymers, fabrication of interpenetrating networks (IPN)[169] and core-shell micro-structures[170]. PNIPAM is used to control certain hydrophilic/hydrophobic behaviour in these systems, some examples are shown in figure 2.3.1.
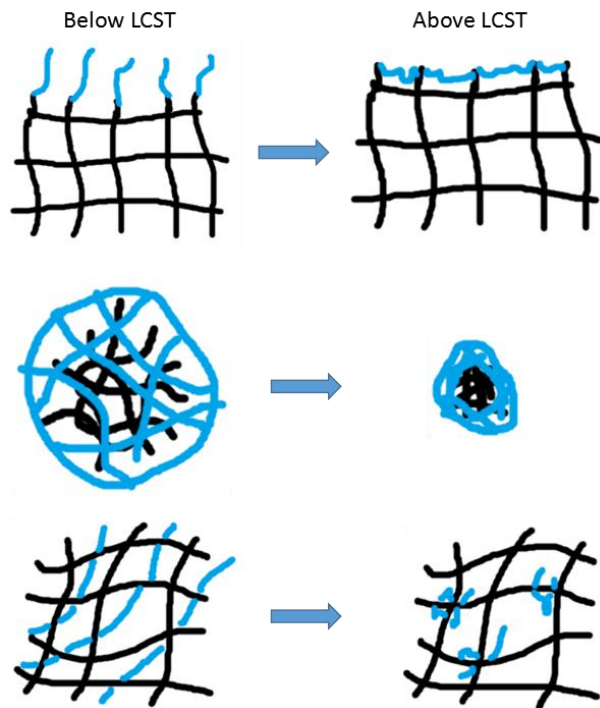
Below LCST   Above LCST

Figure 2.3.1: A brief schematic of PNIPAM grafted brush, micro core-shell structure and semi IPN change from hydrophilic to hydrophobic at LCST in water. The blue line represent PNIPAM chain, the black line represent other polymers.

The PNIPAM can be fabricated into forms of hydrogel[171], microgel[172], membrane[173] and other composite systems. The PNIPAM itself lacks mechanical strength[174], thus commonly other bio-materials such as cellulose[35] and Poly(ethylene glycol)[175] are applied in material systems to enhance it. Such material systems aim at properties such as fast response time, compatibility for direct body injection and degradable in the human body. Furthermore, it can be combined with fluorescence molecules for in-situ monitoring with fluorescence spectroscopy[176] or combined with other "smart" materials such as pH-responsive Poly(methyl methacrylate) to form HP-thermo-responsive hydrogels[177]. These material systems are widely applied for ion-exchange[178], drug delivery[179], cell culture[180], and bio-compatible sensor[181].

Most of the materials mentioned above are within the category of nano-composite systems in which the properties of these nano-composite materials change with the interaction between different components. Therefore, morphology analysis techniques are useful tools to characterize the material structures created during fabrication. Conventional microscope technique can only provide sample shape information and encounter difficulty in high-resolution chemical mapping. If a composite system include three or more different phases as in many complex bio-materials (natural fibers etc), spectroscopy techniques struggle to show the local distribution of nano-particles and conventional microscopy cannot image the phase separation. In contrast, a high-resolution chemical characterization technique can be very beneficial in this case. Thus the SEM techniques (demonstrated in chapter 4) have shown much potential for application in such bio-polymer systems.

2.3.2 Natural polymer - Silks

Silk is a type of material which is built up from natural proteins by a spinning process in animals such as moth (such as Bombyx mori) larva and spiders[182]. The natural silk fibers from Bombyx mori (B. mori) has been used in textile production throughout history[183], but modern application of silk mostly concentrate on the high mechanical properties of silks. The natural silk is known for its remarkable tensile strength and elongation property with moderate modulus. The strongest silk fibers such as major ampullate spider silk and force reeled B. Mori silkcan reach over 1.3 GPa tensile strength and 40% elongation[184]. On the other hand, silk is also a bio-compatible material which is suitable for medical applications. Hence there are a lot of bio-material systems using silk fiber as reinforcement for mechanical strength. More bio-products are fabricated into forms such as gels[185], films[186] and wires[187] using artificial/regenerated silk protein. Such material systems are widely applied in wound healing[188], drug delivery[189], bio- electronic and photonic devices[190] and membrane sensors[191].

The high properties of silks are known to be related with the combination of soft and flexible amorphous phases and strong crystalline phase[192]. The study of origin of this combination lead back to the natural silk fibers, which are still model nano-composite material systems for artificial ones to mimic. The natural silk fiber is a representative hierarchical material. Hierarchical structures are built up by small repeating structural units throughout multiple scale levels[193], typically, from nano-scale to micrometer scale. The local properties of hierarchical materials can be tuned for best overall performance by organizing the local nano repeating unit independently. This makes hierarchical materials capable of combining the advantages of different repeating units and is remarkably versatile. This type of structure is common in biological systems and mimicking this is a major goal in the advanced material fabrication field[194].

The hierarchical structure of silk is composed of several level of repeating unit, including fibroin/spideroin fiber, microscale fiber bundle, microfiber (some silkworm silk only) and nanofibrils (sometime called microfibril for spider silks)[195]. A brief schematic of this structure is shown in figure 2.3.2. At the nano-scale level, the organization of nano crystalline phase and other less ordered phases is considered to be the origin of silks' mechanical properties[196]. However, different concepts are used to describe this nano-crystallinity, they are closely linked but not exactly the same.
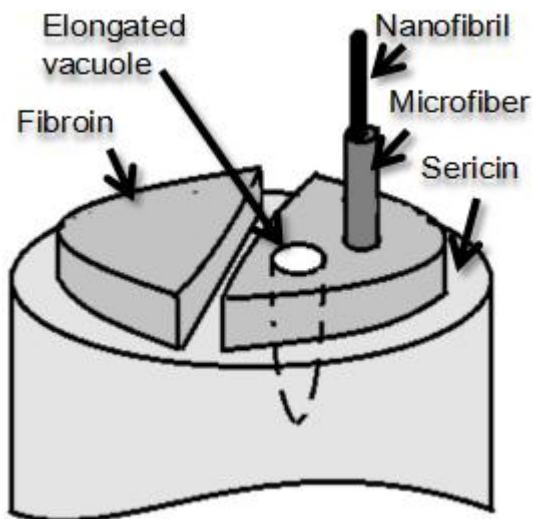
Figure 2.3.2: A schematic of hierarchical structure of silk fiber.

At molecular level, the silk protein is known to adopt different forms: fibroin I, II, III and spidroin I, II. The fibroin I and spidroin I are the major protein forms contributing to the crystallinity and thus tensile strength[197]. The fibroin II and spidroin II is responsible for the more amorphous region but also occurs in crystalline region such as nanofibirls of spider silk[198]. The fibroin III is a liquid-crystalline form that appears in the crystallization progress of silkworm silk[199]. The protein forms are reflected in the vibrational spectroscopies, since the bond vibration difference in the protein forms yield specific peaks. The crystallinity study of such techniques are mostly about these protein forms. How each type of silk protein forms features observed in imaging techniques is still not completely understood, it is proposed that proteins were bonded with extra interlinking agent in forming molecular level repeating units. Due to the complexity of molecule conformation and resolution limit, imaging single protein molecules and identify them directly in SEM imaging is not available with current instrument limitations.

At supermolecule level, the silk protein form nano-phases, including an ordered phase and two dis-ordered phases. The dis-ordered phase include an amorphous phase and an oriented amorphous phase[200]. The ordered phase is mostly build up by a β-sheet structure, which is composed of repeating amino acid units on protein heavy chain using hydrogen bonds[201]. The oriented amorphous phase is not composed of crystals but the protein chains in this phase have some degree of orientation. Although the β-sheet in the ordered phase is commonly measured as fiber crystallinity, the uncounted oriented amorphous phase actually plays an important role in the tensile strength of silk[202]. Single β-sheet crystal dimensions are 9.44 Ǎ for interchain axis, 8.95 Ǎ for intersheet axis and 7Ǎ for fiber axis in a B. mori silk. Since at least 3 pixels for each axis are required to form image, such scale is beyond the resolution limit of the SEM. However, the interlinked crystals still form phases in nano-scale and such features of tens of nanometers can be observed if their chemical contrast can be optimized and identified. These phases are often

indirectly represented in characterization result[203], but the direct local distribution of these phases were still missing which are revealed in chapter 4 for the first time.

In terms of silk repeating structure unit, the nano-fibril (or sometimes called micro-fibril) is considered the crystalline structure in silk fiber[204]. Observation of such structure has been reported by AFM and SEM literature, despite most observation were carried out by disassembling the silk. The size of nano-fibril varies in different sources, ranging from 20nm to 50nm or even larger. The size of nano-fibrils is often considered to be directly linked to crystallinity in microscopy techniques like AFM[205][206]. However, other study show that the nano-fibrils do not consist entirely of β-sheet crystals, but the oriented amorphous phase has not been successfully imaged in microscopy. There has been speculations for the oriented amorphous phase is in the region surrounding nano-fibirls, or forming core-shell structure on β-sheet beads in nano-fibril[207].

The crystallinity is used by researchers to determine the silk mechanical properties[208]. However, as shown above, such crystallinity values can be concluded from different concepts which are not equal to each other, when using different characterization techniques respectively. Not the mention the crystallinity value is often an average result. This cannot reflect the local variation of nano-repeating units, which is the key factor of the hierarchical structure. I notice this is due to a gap between the scale of conventional characterization techniques from macromolecular to more "visible" fibril structure scale. Filling this gap is to provide the local nano-phase distribution with respect to the local organization of nano-fibrils. Applying the SEM chemical mapping technique in chapter 4, this characterization gap can be filled and linking the silk crystallinity formation from supermolecular scale to micrometer scale.

2.4 Summary of challenges for bio-composite characterization

We can summarize the capability of common analytic techniques as reviewed in section 2.1-2.2. The major challenge of bio-polymer composite system characterization is the high-resolution chemical characterization of C based complex materials. Vibrational spectroscopies, X-ray diffraction and electron spectroscopy can provide material information. While the resolution requirement can be met with SEM technique or AFM technique, only the SEM techniques can cover the chemical characterization at the required scales. In the following chapters, the electron spectrum and angular distribution are exploited to fulfill such requirements.

The aim of this project is the development of a suitable SEM analysis technique fulfilling the requirement of bio-polymer nano-composite characterization. These requirements include: 1) nano-scale resolution 2) tens of micrometers of field of view 3) capability of chemical characterization based on the crystallinity and molecule conformation 4) limited sample radiation damage. They are defined by the structure (from micron scale down to nano scale) and composition (sensitive carbon based chemicals) of the material systems as reviewed in section 2.3. In order to achieve this, combination of angle-selective BSE and energy-filtered SE technique are applied with the assistance of Monte Carlo simulation of the electron signal yield. The brief procedure of this project is shown in figure 2.4.1 below.
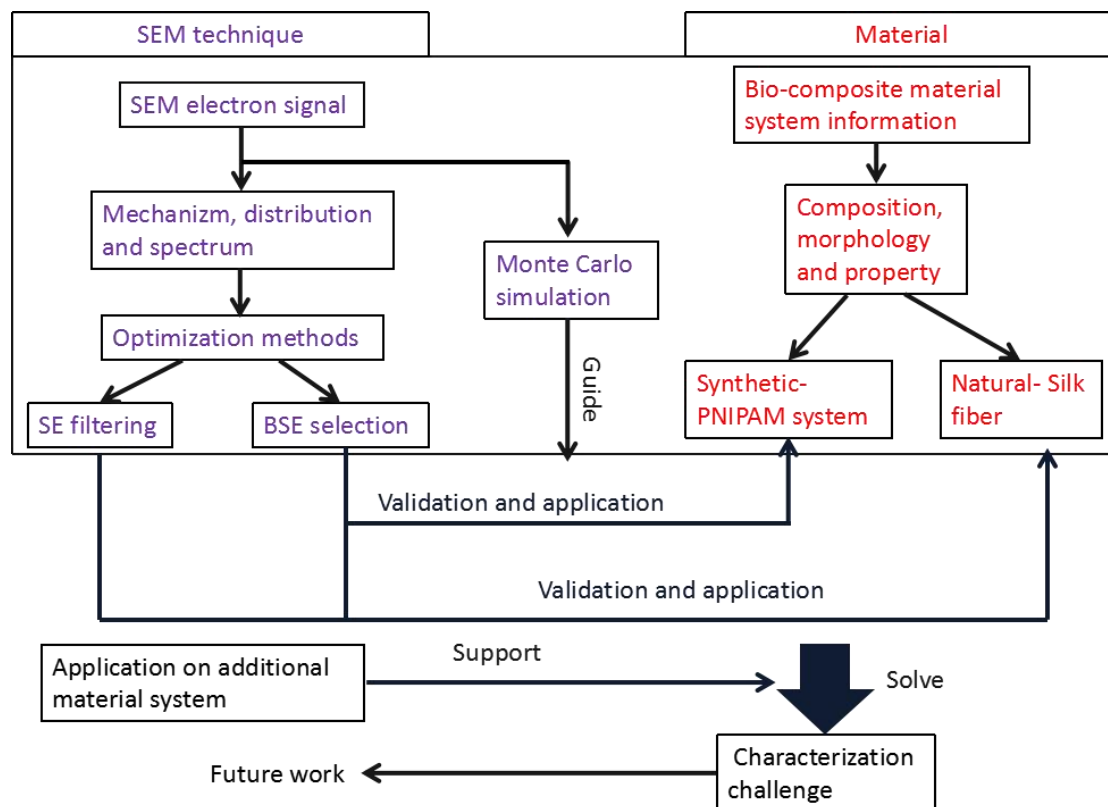

Figure 2.4.1: The brief procedure of this project, showing how the SEM technique can

be optimized to meet characterization requirement of bio-composite systems.

First the BSE signal was studied through the comparison between experimental and Monte Carlo simulation results. The distribution of BSE signal on the detector can be optimized for compositional contrast. This method can conveniently provide material contrast as conventional BSE technique, but also works for low-voltage SEM settings, C based material system. This part is demonstrated in chapter 4.

Second, the energy-filtered SE imaging was introduced for higher resolution requirements and multi-phase complex materials. Due to resolution limitation of the BSEII signal, the angle-selective BSE can only reach spatial resolution of ten nanometer level even in low-voltage SEM. The SE technique is only limited by the resolution limit of microscope itself, thus can reach sub-nanometer level in ideal situation. As filtered SE technique base on the electron spectrum, the image collected in this technique can correspond to specific molecule structure. This part is demonstrated in chapter 4.

Despite the advantage of energy-filtered SE technique, the SE spectrum of complex polymer systems is still not understood and subject to research. Comparison of SE spectrum between selected material systems can reflect the nature of electron signal peaks in spectra, as well as validate the imaging results collected in 4.2. Noticeably some electron spectra fine structures appear at the same energy value of UV absorption or fluorescence peaks, confirming such energy bands' existence. This opens up the opportunity to utilize such energy region for chemical characterization in bulk composite materials by SE hyperspectral imaging (SEHI). More research on the structure of electron spectrum is needed for utilizing the full potential of filtered SE technique in bio-polymer composite systems.

3. Experimental

The detail of microscope experimental setting and data processing has been included in the manuscripts in result and discussion section 4.1 and 4.2. Here, only the sample materials provided by collaborators and the general sample preparation/microscope detection setup used by all of our experiments are briefly introduced .

3.1 The sample materials

The following sample materials are provided by collaborating groups and thus the synthesis detail are not included. Following sample information is only briefly introduced to show their basic chemical composition which was used in our SEM experiment.

The PNIPAM/PEGDA semi-IPN provided by Dr. R. A. Plenderleith was produced from (Gly-Arg-Gly-Asp-Ser) peptides and carboxylic acid functionalized, pyrrolecarbodithioate ended highly-branched PNIPAM. The composite went through radical copolymerization using Naphthyl Vinylpyridine and Diethylene glycol diacrylate with PNIPAM material in presence. The sample material is a bulk phase separated nano-composite system. The molecule weight of PEGDA is 40000, the concentration of PNIPAM in the system is 20% and the crystallinity of the system is unknown.

The natural B. mori and A. mylitta silk fibers provided by Dr. C. Holland was unraveled in deionized water from natural silk cocoons. The A. mylitta silk was demineralized in ethylene diamine tetra acetic acid beforehand.

The natural spider silk samples were produce through forced reeling of adult female Nephila edulis dragline silk on a plastic frame at 20 mm/s^1 under room temperature. Detail information about the preparation is shown in literature[209]. The size and composition of the repeating unit in natural silk is still under debate but the compositon of one protein molecule is listed below in table 3.1.1

Table 3.1.1: the amino acid composition of silk proteins

Amino acid	Percentage (%)
Ala	34.37
Arg	0.98
Asp	2.31
Cys	0.18
Glu	1.73
Gly	42.6
His	0.3

Ile	0.96
Leu	0.81
Lys	0.56
Phe	1.32
Pro	0.59
Ser	15.98
Thr	1.19
Trp	0.5
Tyr	11.29
Val	3.12
Amm	0.24

The thin spin coated silk film provided by Dr. C. Holland was produced using silk gland extracted from fifth instar of B. mori silkworms dissected in room temperature. Water (at 5 °C ± 3 °C) was used to rinse the silk glands which were then submerged in a fresh quantity of water also at 5 °C (± 6 °C) prior to removal of the outer membrane. Each gland was cut into four segments where segment one is known to be rich in sericin, the concentration of which decreases along the length of the gland to segment four which is known to be sericin free. The segments were placed in eppendorph tubes and homogenized via gentle shaking for 16 hours. The solutions were diluted with water and homogenized before spun coated on pre-plasma cleaned silicon wafer. The silk is not crystallized in the gland, so the film produce from gland cross-section is totally amorphous.

The artificial silkworm silk film with laser feature provided by A. Brif was also produced from B. mori silkworm gland, and segment is chosen to include no sericin. The solution of gland was processed with riboflavin and coated as a photocurable film on glass substrate. The original silk film is amorphous. The feature on the film was created by UV laser exposure.

3.2 Sample preparation for SEM - cryo-snap and plasma treatment

The bio-composite material applied in my project is mostly vulnerable to deformation in sample preparation, thus such samples were cryo-snapped to create a representative cross-section surface of its inside structure. The samples (fiber or film) was fixed between two pieces of silicon wafer before immersion in liquid nitrogen. The sample remains in liquid nitrogen for ~10min to reach uniform temperature inside before fracturing. As the sample is exposed to air during transportation and loading to the SEM frost may form on the sample, however the

water interaction with silk is known to be recoverable.

The samples are plasma treated with a Diener Zepto version B plasma etching unit. The plasma etching is done in a vacuum chamber with cold gas plasma generated inside. The gas input can be selected from different gas such as air for PNIPAM materials and argon for silk materials. The plasma treatment improves the conductivity on samples. The possible artifact was considered and excluded by comparing the sample surface after different time of plasma treatment. The silk film samples are not treated by plasma due to thin thickness and potential sample damage.

The plasma treatment was set to 100W power for bulk samples and 50W for fiber samples, and the respective treatment time (as described in result sections) are concluded from experimental testing. For example, in the preparation of silk sample, the etching time was controlled so that the plasma artifact pattern (discussed in section 4.2) do not exist on the treated sample surface. Since plasma etching tends to remove more amorphous phase than crystalline phase, this treatment will create surface topography. However, as long as such effects follow the sample composition distribution, it would not produce artifact in the imaging. An example of such effect was shown in the AFM result of treated PNIPAM/PEGDA sample in section 4.1.1, where 10-20nm high topography was created according to local crystallinity.

3.3 SEM detection system setup and signal simulation

The SEM imaging in this project is carried out using an FEI Nova 450 microscope. The BSE detection setup and the energy filtering SE setup are briefly described below.

In order to minimize the error of measurement in SEM imaging, all data used in the calculation and analysis was averaged from a series of image respectively. The image brightness/contrast measured in BSE imaging was repeated 5 times each data point. The SE spectra measurement was repeated 5 times each data plot, every measurement was done on an independent 1μm×1μm sample area. The effect of error of each plot on finding SE peaks is discussed in SI 3 of section 4.2. The feature size measurement in imaging of silk fiber was averaged among three different fiber samples of each species.

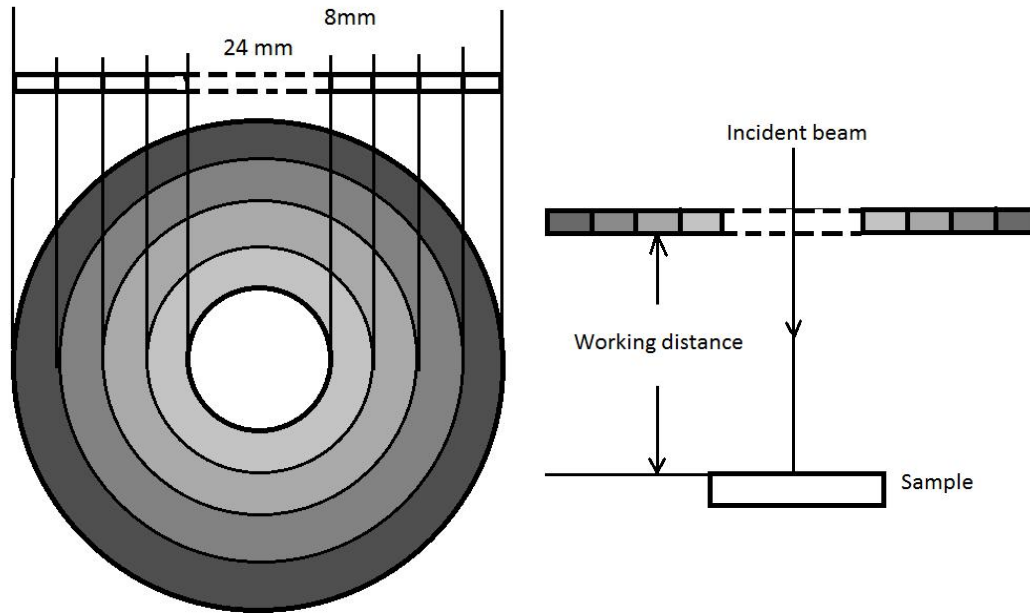### 3.3.1 CBS detector parameter and measurement procedure in BSE imaging

Figure 3.3.1: A schematic showing the shape and parameters of our CBS detector applied in BSE imaging. The working distance is measured by focusing in the BSE imaging mode, thus detector thickness do not need to be considered.

As shown in figure 3.3.1, the parameters of CBS detector, including the radius of central hole and width of each detector ring is a give value. The only controllable parameter of detector spacing is the working distance. In a series of imaging of a given sample using the same beam energy and deceleration field setting, each working distance corresponds to a certain relationship between distribution of electron scattering from sample and electron landing on detector. The angle range covered by the whole detector increases when working distance becomes smaller, but the range of individual rings do not follow a same trend. In the BSE imaging of this project, the working distance between 7mm and 2mm was chosen (7mm is the largest working distance when SEM immersion mode can be activated). The angle range covered by all four detector rings are $9.7°$-$15.9°$, $15.9°$-$21.8°$, $21.8°$-$27.2°$, $27.2°$-$32.1°$ when working distance is 7mm. The angle ranges are increased to $30.9°$-$45°$, $45°$-$54.6°$, $54.6°$-$60.9°$, $60.9°$-$65.5°$.

In the imaging of samples, the field of view chosen for measurement depends on the scale of features required to be analyzed. The horizontal width of whole field of view is about 50 times of the feature radius so that a suffient number of features are included in the measurement. For example, for a PNIPAM sample in which PNPAM particles are on the scale of 100-200nm, the horizontal field width in measurement is 8μm. Each image set uses the same field of view size in the measurement, the sample area is changed after each measurement on homogeneous samples such as PNIPAM to avoid surface damage/artifact after long beam radiation time. Data was measured using whole image field of view for each image set and the measured data are averaged using five sets of images collected with the same microscope setting.

3.3.2 Energy filter mechanizm, spectra measurement and hyperspectral imaging procedure

The energy filter system uses a deflection field, which is an integral part of the through the lens detector ,to guide the electron signal on to detector. As shown in figure 3.3.2 below, as the deflection field becomes stronger, more electron hit the detector. Thus each deflection voltage defines a critical kinetic energy range, if the electron energy is higher than this critical value it will not be detected. The electron signal strength given by TLD detector is the integration of all electron below this value, and if we differentiate the signal strength to deflection voltage the result is the electron energy spectra versus deflection voltage.

Since every deflection voltage corresponds to a maximum energy of detectable electron, a relationship can be built between the deflection voltage and electron energy. In this detection system a stage bias is applied on the sample so that we can add a chosen value of additional kinetic energy to the electron signal. As we add a series of energy (1eV, 2eV ...) to electron energy, we can measure the deflection voltage where same spectra feature appears. As result, we can plot the deflection voltage to the change in electron energy and fit their relationship. Detail of such calibration is shown in SI 2 of section 4.2.

The relationship of electron energy to deflection voltage is a linear relationship on the detection system applied in this project. The electron energy equals to 2.84 multiplied by the deflection voltage. The calibration of this system is not done by me, the measurement done by R Masters is shown in SI 2 of section 4.2.

As we described above, each deflection voltage lead to an integrated electron signal landing on the TLD detector. So the energy-filtered image we collected is also formed by all electron below chosen energy. In order to analyze the SE spectra of silk sample, a series of filtered image using 0-10eV (for silk material, would differ based on material types) is taken. The change in electron energy in the measurement is set to 0.07eV. Each image in a data set is collected on exactly same sample area, the size of area is decided by the scale of local phase separation, which 1μm×1μm for silk fiber. The brightness value of each phase in the chosen area is measured on each filtered image as a data point. Each data point is repeated on 5 independent areas on same sample. (P2.4.4) The plot of these data point versus the electron energy is the integrated electron spectra, the SE spectra can be acquired by differentiation.

Since the silk fiber sample is sensitive to beam damage, the scanning time of each data point is limited. This can lead to noisy data. The smoothing of data is done through an origin 9.0 software, using a Savitzky-Golay smooth, the points of window is set to 5. (P2.4.2) Due to the complex shape of SE spectra, a convenient mathematical fitting for each peak is still not available. Experimentally, I chose the energy value where the differentiation of SE spectra equal to zero as the start and end of each peak, and the energy range between these value as the width of each peak. The shape of experimental SE peak varies greatly on silk, so the width of peaks

also varies. Generally the peaks in 0-10eV energy region is about 0.4-0.7eV wide, so a ±0.3eV is considered acceptable for each spectra. (P2.4.6) The detail of peak location and energy window used for silk fiber is listed in detail in SI 3 of section 4.2.
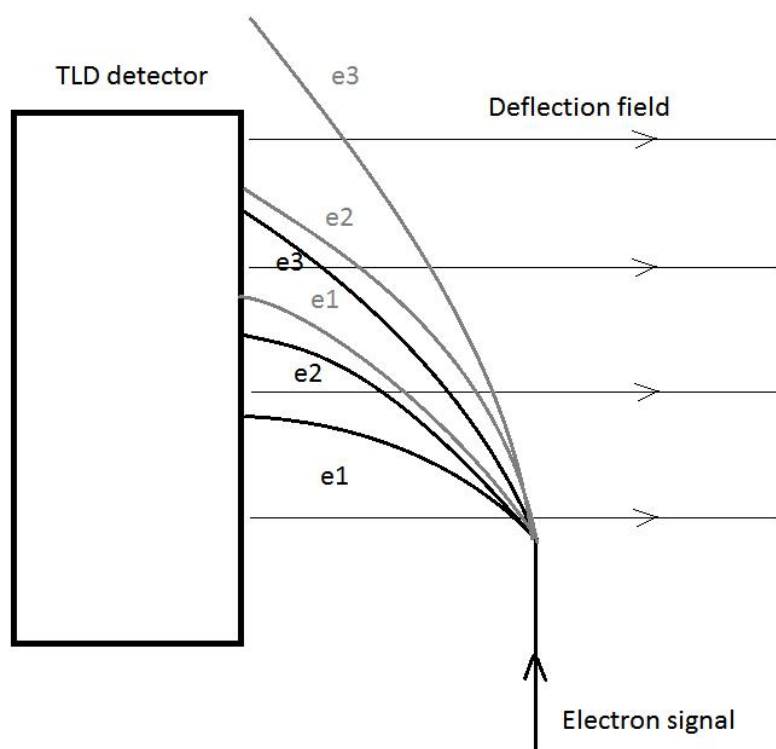

Figure 3.3.2: A schematic of energy filter mechanizm, e1, e2, e3 are three electron with different energy, black trail are the trail of electrons when deflection voltage is U_1, grey trail is the trail when deflection voltage is U_2. $U_1 > U_2$

3.3.3 Procedure of Monte Carlo simulation

The Monte Carlo simulation was applied to guide BSE and SE imaging in this project, and the procedure to calculate the simulation input of elastic scattering and inelastic scattering are described below. The SE spectrum and BSE distribution is given by the simulation program using 1 million inputs for each material and incident beam energy.

The elastic scattering input for simulation includes the total elastic scattering cross-section and plot of cumulative probability of elastic scattering versus scattering angle. Such input needs to be calculated for a series of incident beam energy 100eV, 200eV … 2000eV in this project. The calculation includes several steps, using the composition information, I calculated the atomic potential, phase shift and the differentiate elastic cross-section (to angle) of each atom. The cross-section of whole molecule is the summation of all atoms and then total cross-section and probability can be calculated accordingly.

The inelastic scattering input includes the inelastic mean free path and plot of

inelastic cumulative probability versus energy. The input was calculated for energy 100eV, 200eV ... 1000eV in this project. The calculation starts from optical absorption/reflection data of sample material. The complex refractive index can be calculated and thus optical loss function is acquired. As introduced in section 2.2.1 and 2.2.2, if we fit the optical loss function into Drude equation form and extend it to finite q region, the electron energy loss function is available. The calculation of inelastic mean free path and probability was done using the computing software respectively.

4. Result and discussion

The section 4.1 and 4.2 are covered by three published papers, a statement of contribution and copyright is accompanied with the manuscript and supporting information of each paper. In order to preserve the original structure of the paper manuscripts, the numbering of tables and figures in each paper are done independent to the thesis. To ensure each numbering is unique, the numbering of paper manuscripts start with a "PX", for example, the "figure 1" of first paper (section 4.1.1) is numbered as "P1 figure 1".

4.1 Angle-selective BSE and phase separation characterization of a PNIPAM/PEGDA nanocomposite

In order to study the BSE signal in angle selective detection, the BSE imaging in large angle and small angle was collected using a concentric backscattered detector (CBS). The large angle BSE images were compared with AFM height mapping to validate its topographical dependency, which is discussed in 4.1.1. The smaller angle BSE signal is suggested to be composition dependent as established by Monte Carlo simulations. These different contrast types were validated and optimized for given PNIPAM composite material in 4.1.2. The statement of contribution and copyright of each section is attached at the end of thesis. (P3.1)

4.1.1 Separating topographical and chemical analysis of nano-structure of polymer composite in low voltage SEM

The paper attached below is published on 2015 J. Phys.: Conf. Ser. 644, 012018. This paper includes one manuscript, with three figures, P1 figure 1-3. Statement of contribution and copyright is attached at the end of thesis.

The original research aim of manuscript in 4.1.1 is to study the relationship between image contrast formed by using different CBS segments and surface topography directly. So the height of topographical features was plotted to image contrast of D segment directly. However, in later research it is realized such direct relationship is an over simplification of BSE angular distribution. Thus a more systematic approach with theoretical simulation and experimental validation was practiced to separate compositional and topographical information in 4.1.2. The section 4.1.1 is included in this thesis to show how composition and topography information can be separated experimentally using CBS detector, then its mechanism and optimization is studied in detail in section 4.1.2.

Q Wan[1], R A Plenderleith[1], M Dapor[3], S Rimmer[2], F Claeyssens[1], C Rodenburg[1]

[1]Department of Material Science and Engineering, University of Sheffield, Western Bank, Sheffield, S10 2TN, UK

[1]Department of Chemistry, University of Sheffield, Western Bank, Sheffield, S10 2TN, UK

[3]European Centre for Theoretical Studies in Nuclear Physics and Related Areas (ECT*-FBK) and Trento Institute for Fundamental Physics and Applications (TIFPA-INFN), via Sommarive 18, I-38123 Trento, Italy

Email: qwan2@sheffield.ac.uk

Abstract. The possibility of separating the topographical and chemical information in a polymer nano-composite using low-voltage SEM imaging is demonstrated, when images are acquired with a Concentric Backscattered (CBS) detector. This separation of chemical and topographical information is based on the different angular distribution of electron scattering which were calculated using a Monte Carlo simulation. The simulation based on angular restricted detection was applied to a semi-branched PNIPAM/PEGDA interpenetration network for which a linear relationship of topography SEM contrast and feature height data was observed.

1. Introduction

Due to the strong dependence of functional properties of polymer nano-composites on nano-morphological features, the characterization of nano-scale morphology is vital in the field of polymer nano-composite materials. Among all the techniques developed to provide morphological information, the SEM techniques processes several advantages: the simple sample preparation, contact free measurement, reasonable resolution in surface imaging and convenient scanning of a relatively large area comparing to other microscopies such as Transmission Electron Microscopy (TEM)[1] and Scanning Probe Microscopy (SPM)[2].

Low-voltage (LV) SEM was developed in order to overcome the radiation damage on beam-sensitive samples, still avoiding the need of conductive coatings[3]. Earlier application of LVSEM to materials such as regenerated silk fiboin nanofibre[4] and bone grafting[5] has proved to be an efficient technique. However in the condition of

46

low-voltage SEM the energy of the backscattered electrons (BSE) may drop to similar levels of the secondary electrons (SE), and the normal separate detection of the SE and BSE may not be applicable. Thus effort to achieve separated topography and chemical information from SEM image contrast were made by the introduction of the theories of electron scattering in the imaging process. As shown in the studies of natural fibre[6] and metal[7] samples this electron kinetic based detection provided a potential extraction of topography and chemical contrast. The recent study on the photovoltaic materials has pushed this detection technique further to predictable material contrast mapping and identification[8].

The distribution of the scattered electrons may be analyzed for SE or BSE in several aspects such as the kinetic energy, the impact depth and the scattering angle. Using a concentric backscattered detector which can potentially detected ~50 eV signal[9], we have chosen the scattering angle of the backscattered electrons as the main factor in our separation of topographical and chemical information.

2. Experimental

The 0%, 5%, 10%, 20% and 30% extracted PNIPAM branched PNIPAM/PEGDA interpenetration network sample (the synthesis process is described in reference[10]) was treated with a Diener Zepto version B plasma cleaner. The gas input was air, and etching condition was set to 840 s with a power of 100 W. The plasma chamber was ventilated once during the etching to avoid overheating the sample surface. The AFM height data were acquired with a Dimension 3100 AFM in tapping mode.

The PNIPAM/PEG samples were imaged by a FEI NOVA 450 SEM in low-voltage conditions (<5 kV accelerating voltage) and the spot size was set to 2 in all images. SEM images were taken using a concentric backscattered detector with 4000 V beam deceleration field in working distance ~4 mm. The applied detector segment and the accelerating voltage are listed for individual images.

3.Result and Discussion

According to the definition of contrast, the simulated image BSE contrast, C_s, can be described by the equation 1, as follows:

$$C_s = \frac{I_s - I_s{'}}{I_s{'}}$$

(1)

where I_s is the simulated BSE signal of the sample PNIPAM, and $I_s{'}$ is the simulated BSE signal of the background (PEGDA matrix).
The calculation of the simulated BSE signal, I_s, is based on the equation

$$I_s \propto \eta \sum_{\theta_1}^{\theta_2} P_{elastic}(\theta)$$

(2)

where $P_{elastic}$ is probability of electron elastic scattering at angle ϑ, ϑ_1 and ϑ_2 are respectively the minimum and the maximum of the range of scattering angles for a

given detector segment, and η is the backscattering coefficient of the respective material.

η is calculated by a Monte Carlo code and $P_{elastic}$ is computed by using the Mott theory (details of the Monte Carlo method and of the Mott theory are described in reference[11]). The CBS detector was installed at the end of the objective lens pole piece. The angular range of each CBS detector segment was calculated by the measurement of inner segment size and by literature data[9]. The diameter of the inner segment A is 4 mm and each segment is 0.8 mm wide. The working distance as set on the microscope was kept close to 4mm.

For our imaging condition of 700 V primary beam we found to be η=0.135 for PNIPAM and η=0.118 for PEGDA. The angular probability on each detector segment is shown in P1 Figure 1(a).

The comparison of simulation (C_s) with the experiment (C_e) in P1 Figure 1(b) shows that the backscattered electron signal dominates in the inner segments, especially in segments B and C, which allows the chemical mapping with BSE using these segments.

The simulation also revealed that the BSE signal on the outer segment D on the CBS detector is very weak for materials using small working distances. C_s in segment D at 4 mm working distance would be ~ -1%. This means that PNIPAM is darker than PEGDA matrix. However the C_e in segment D is ~ 21%. Due to the very weak BSE contribution to the signal in segment D in the simulation, we expect that C_e in the segment D, stem mostly from SE and thus provides topography information for our chosen experimental settings. However we note that the electron distribution is sensitive to the working condition of the microscope such as working distance and beam deceleration.
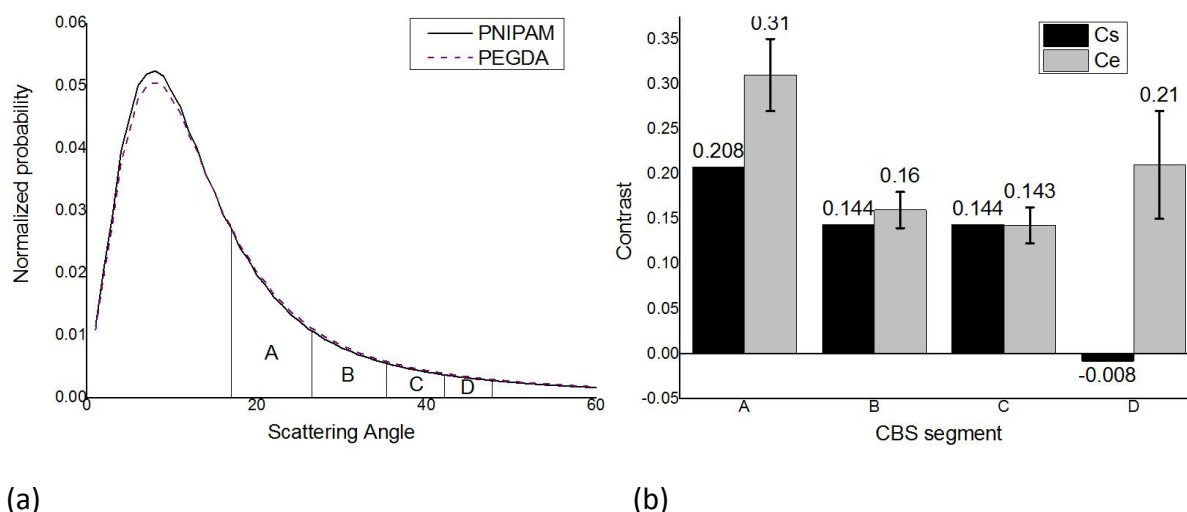

(a)   (b)

P1 Figure 1: The angular probability of backscattering angle (a) and the C_s and C_e in segments A-D (b) for a 20% etched PNIPAM/PEGDA sample imaged with 700 V primary beam energy and 4mm working distance.

We have imaged the plasma etched and un-etched PNIPAM/PEGDA samples with segment D at primary energy 700 V and working distance 4 mm, and compared the

contrast of topographic features including the PNIPAM particle and PEGDA matrix phase separation (P1 Figure 2(a)) to AFM height data (P1 Figure 3). We note that C_e of objects on the segment D images has a rather linear relationship with the respective height data measured by AFM. The PNIPAM particle data is almost proportional while the PEGDA phase separation deviates only slightly below 30 nm height (P1 Figure 2(b)). We find that a linear relationship is valid in height range of 30-100 nm for our objects with <300 nm diameter.
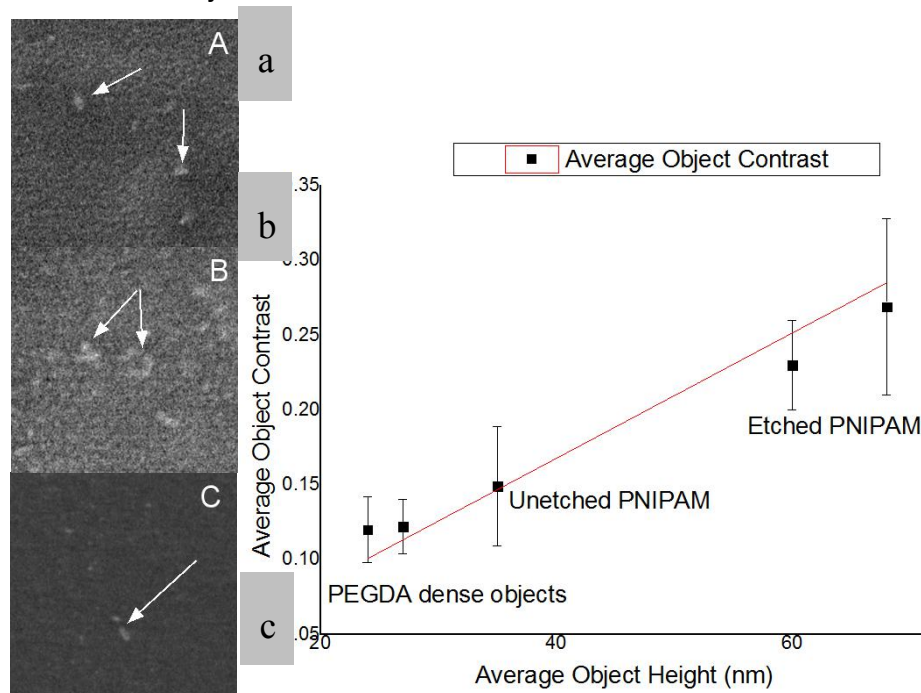
P1 Figure 2: The CBS segment D image (normalized enhanced C_e) of 100 W/840 s plasma etched (a and b) and un-etched (c) PNIPAM particles and the average contrast vs average height of different objects. The field of view for SEM image is 2x2 μm. The PNIPAM particles are pointed out with arrows.
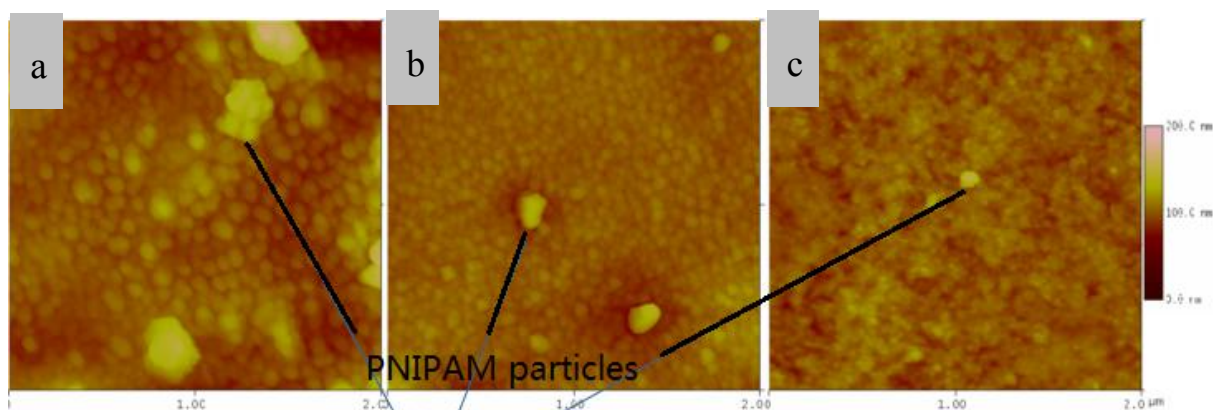
P1 Figure 3: The AFM image of of 100 W/840 s plasma etched (a,b) and un-etched PNIPAM particles(c). The field of view in each image is 2x2 μm, the height range is 0-200 nm.

The deviation in the PEGDA phase separation feature may be due to the larger

error in the measurement of smaller features by both AFM and SEM. More data on other materials should be collected to test the wider applicability for the linear height-contrast relationship. We note the peak in elastic scattering angular probability curve will shift to the smaller angles as the material becomes denser. Materials denser than our sample tend to have lower BSE signal in outer segment D. This indicates that our height mapping may still be reasonable for materials denser than our polymers.

4. Conclusion

The distribution of backscattered electrons was simulated and the separation of chemical and topographical information in LVSEM was achieved through the controlling of angular range of detection in our experiment. We found an approximately linear relationship between contrast C_e in CBS D segment and the AFM height data for two polymers. Such a relationship therefore could be used for contact free direct height mapping of nano-topographical features in LV-SEM once a calibration curve is recorded.   Simulations suggest the wider applicability to denser materials.

References

[1]   Danino D, 2012 *Curr Opin Colloid Interface Sci*, **17** 316

[2]   Vansteenkiste S O, Davies M C, Roberts C J, Tendler S J B, Williams P M, 1998 *Prog Surf Sci*,

          57 95

[3]   Vezie D L, Thomas E L, Adams W W, 1995 *Polymer*, **36** 1761

[4]   Mhuka V, Dube S, Nindi M M, Torto N, 2013 *Macromol Res*, **21** 995

[5]   Benezra Rosen V, Hobbs L W, Spector M, 2002 *Biomaterials*, **23** 921

[6]   Rasch R, Stricher A, Truss R W, 2013 *J. Appl Polym Sci*, **131**

[7]   Nagoshi M, Aoyama T, Sato K, 2013 *Ultramicroscopy*, **124** 20

[8]   Masters R C et al, 2015 *Nat Commun*, **6** 6928

[9]   Sakic A et al, 2011 *Micro Technology and Micro Devices SAFE, 1-4*

[10]   Plenderleith R, 2014 *thesis* University of Sheffield

[11]   Dapor M, 2014 *Transport of Energetic Electrons in Solids*, Springer. Tr. Mod. Phys., Vol. 257 (Springer, Berlin)

4.1.2 Angle selective backscattered electron contrast in the low-voltage scanning electron microscope: simulation & experiment for polymers

The paper attached below is published in 2016 Ultramicroscopy, 171, 126. This paper includes one manuscript with 13 figures, P2 figure 2.1.1-4.2.7 and one supporting information with 4 figures, P2 figure SI 1.1- SI 3.1. Statement of contribution and copyright is attached at the end of thesis.

Note the CBS detector can only detect a certain series of angular ranges, and all the signal intensity data points given in the manuscripts are collected from such angular ranges. For example, in P2 figure 4.1.1 c, every data point is collected from the angular range of segment A or B. The angle value given on the plot is the inner or outer boundary of the angular range when the respective data point is collected. The 17 degree for A segment means at that data point, the inner boundary of A segment angular range is 17 degree. These angles were given to show the whole angular range where the relationship between simulation and experimental remain linear, which is from 17-38 degree in this plot. Such angular ranges were marked on each accompanied BSE angular distribution curve.

There is a misused term in this manuscript, which is "pure composition contrast" such as in the abstract. The optimization of contrast was done by exploiting distribution of BSEI and BSEII, but in order to acquire enough signal to form image the very low BSEI angle region is not preferred. So the "pure composition contrast" or "pure BSEII signal" only exist theoretically, and is not applicable in imaging. The images collected for composition contrast in the manuscript is more accurately BSEII dominated contrast, where the intensity of BSEII is at least 2 times stronger than the BSEI.

Q Wan[1], R C Master[1], D Lidsey[2], K J Abrams[1], M Dapor[3], R A Plenderleith[1], S Rimmer[4], F Claeyssens[1], C Rodenburg[1]

[1]Department of Material Science and Engineering, University of Sheffield, Western Bank, Sheffield, S10 2TN, UK

[2]Department of Physics and Astronomy, University of Sheffield, Western Bank, Sheffield, S10 2TN, UK

[3]European Centre for Theoretical Studies in Nuclear Physics and Related Areas (ECT*-FBK) and Trento Institute for Fundamental Physics and Applications (TIFPA-INFN), via Sommarive 18, I-38123 Trento, Italy

[4]Department of Chemistry, University of Sheffield, Western Bank, Sheffield, S10 2TN, UK

Email: qwan2@sheffield.ac.uk

Abstract

Recently developed detectors can deliver high resolution and high contrast images of nanostructured carbon based materials in low voltage scanning electron microscopes (LVSEM) with beam deceleration. Monte Carlo Simulations are also used to predict under which exact imaging conditions purely compositional contrast can be obtained and optimised. This allows the prediction of the electron signal intensity in angle selective conditions for back-scattered electron (BSE) imaging in LVSEM and compares it to experimental signals. Angle selective detection with a concentric back scattered (CBS) detector is considered in the model in the absence and presence of a deceleration field, respectively. The validity of the model prediction for both cases was tested experimentally for amorphous C and Cu and applied to complex nanostructured carbon based materials, namely a Poly(N-isopropylacrylamide)/Poly(ethylene glycol) Diacrylate (PNIPAM/PEGDA) semi-interpenetration network (IPN) and a Poly(3-hexylthiophene-2,5-diyl) (P3HT) film, to map nano-scale composition and crystallinity distribution by avoiding experimental imaging conditions that lead to a mixed topographical and compositional contrast.
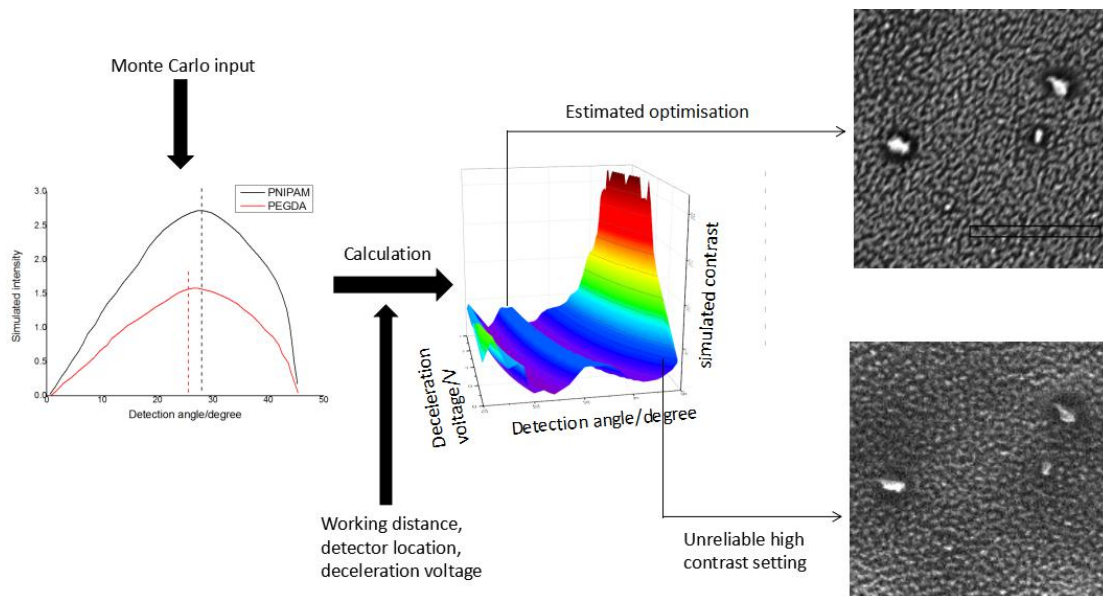
Research highlights

1. An optimised model for nano-scale analysis of beam sensitive materials by LVSEM.
2. Simulation and separation of composition and topography in a CBS detector.
3. Selective angle backscattered electron collection for mapping of polymers.

Keywords

Low-voltage scanning electron microscopy, quantitative back-scattered imaging, polymer, concentric back scattered detector, angle selective SEM

1.Introduction

Low-voltage scanning electron microscopes (LVSEMs) have substantially benefited from the development of the field-emission gun and high sensitivity detectors in last few decades[1]; resulting in a significant increase of resolution from 100nm to <0.5nm[2]. Nowadays, the LVSEM is commonly used as a high resolution imaging for surface topography and insulators[3].

In the case of imaging insulator materials, it is well known the SE signal is highly sensitive to charging on the sample surface, voltage contrast will also form as a result of the charging effect [4]. Although BSE imaging is generally less affected by surface charging, the electric field build up on sample surface can still cause electron beam deflection and strong electron implantation effect which leads to sample damage[5] [6], especially if the primary beam energy exceeds a few keV as in conventional BSE imaging. In order to prevent the charging situation, ordinarily, a conductive coating is applied in conventional SEM. Unfortunately this coating hides the surface detail and can create artificial signals due to the electron range differences in the sample material and the coating [7]. In contrast, the LVSEM technique allows careful control of the primary voltage which allows for the imaging of non-conductive insulating

materials, even in the absence of a coating[8].

Additionally, for a composition based investigation, low-voltage backscattered (LVBSE) imaging can provide relatively high imaging resolutions up to <5nm[9]. Since the electron range is significantly decreased in LVBSE imaging[6], a non- coated specimen is strongly preferred for a quantitative analysis. In the absence of a conductive coating, the primary electron energy is limited to a small energy range in which the electron input and emission is close to balance. The BSE signal can be optimised for uncoated insulating samples and, generally, reaches a maximum value around primary energy setting of 1-2keV [10][4].

To optimise the LVBSE imaging, Monte Carlo (MC) simulations are required to predict the image contrast, as conventional calculation methods yield large deviations when the primary electron energy drops below 2keV[11]. Such MC simulations normally comprise of both inelastic scattering and the elastic scattering. The inelastic part employs the dielectric function approach as physical model in the simulation programmes and the relevant prediction for low-voltage setting has already been reported to match the experiments[12] in SE imaging. In the case of elastic scattering simulation, the Mott cross-section solved from Dirac equation was widely applied for electron energy over 100eV[13]. It's application for simulating electron matter interactions have been reported by researchers[14][15][16]. Here we report on its use for the prediction of optimised angle selective BSE imaging conditions for low density materials.

Although BSE are commonly expected to exhibit compositional information, the BSE signal can also contain topographical information[17]. This is because the signal emitted from the sample contains BSEI, which is generated from near-surface area and applied in topographical imaging[18], and BSEII which reflects purely composition information as they originate from deeper in the specimen and have undergone multiple scattering events[19]. In order to acquire compositional or topographical information separately through BSE imaging an angular selection is needed since the BSEI are generally emitted at large angles[20]. The detailed mechanism of BSE detection and contrast formation based on scattering angle has already been discussed in literature[21]. Here we introduce MC simulation to predict the necessary experimental conditions under which a separation in the landing angle of BSEI and BSEII can be achieved.

The concentric back scattered detector or circular back scattered detector (CBS) is a multi-segment solid state high-efficiency BSE detector[22] which is composed of multiple rings which can form images simultaneously. Thus it can collect the emitted electron signal from a set angular range[23][24]. Here we show how to optimise the microscope settings in terms of angular acceptance range by combining the low detection threshold of CBS detector with a deceleration (retarding) field[25], so it becomes possible to acquire high contrast BSE images of materials with very small average atomic number differences (free from topography). Although this work is focused on carbon based polymer materials, we expect to apply this method for heavier elements analysis such as for carbides in steel[26]. As the experimental settings for LVBSE imaging can vary greatly when a deceleration field is employed,

model calculations ensure suitable imaging conditions are used to access compositional information only.

2. Theoretical background and calculations

Monte Carlo simulations can be used to calculate the electron emission from a given point at the specimen surface.   This then needs to be translated into a local signal strength, S_D, at a given point on the detector plane, based on the spatial and energy distribution of the emitted electrons as well as user-controllable parameters in the LVSEM such as the working distance and the deceleration voltage, U_d.

The angle between the incident primary beam and the straight line from emission point to detection point, ϑ_D, is shown in Fig. 2.1.1. It is defined by the working distance for $U_d=0$.

2.1 Determination of detected electron signal from the simulated electron emission

Since our calculation is focused on the signal formation in our CBS detector, only the electron signal that can potentially reach our detector is considered in the following calculation. For simplicity, we only consider the case in which the entire interaction volume is contained within the material, thus we exclude the possibility of electrons being transmitted. For any other cases the adsorbed and transmitted electrons have to be considered in more detail as the transmitted electrons could contribute to the detected signal and cause substantial contrast as was shown in literature[27]. Traditionally the electron signal detected by a SEM detector is ascribed to two parts: the secondary electron (SE) signal and the BSE signal. Thus, the overall detected electron signal strength, S_D, can be represented by equation 2.1.1:

$$S_D = (S_{D(BSE)} + S_{D(SE)}) \qquad\qquad 2.1.1$$

S_D is the electron signal strength measured at detection point

$S_{D(BSE)}$ is the electron signal strength of BSE at detection point

$S_{D(SE)}$ is the electron signal strength of SE at detection point

Assuming U_d = 0, the electrons emitted with scattering angle, ϑ_S, move towards the detection point in a straight line from the emission point. The angle between the primary beam and the straight line from emission point to detection point written as ϑ_D (Fig. 2.1.1 a) is equal to ϑ_S.

S_D at this detection point can be estimated from following equation[28]:

$$S_D \propto \iint [P_{BSE} * (E_{BSE} - E_T)]dE_{BSE}d\theta_S + \iint [P_{SE} * (E_{SE} - E_T)]dE_{SE}d\theta_S \qquad 2.1.2$$

E_T is the detector energy threshold (the minimum energy that leads to a detection event which is a characteristic of the detector used)

E_{BSE} is the electron energy of a backscattered electron when it reaches the detection point

P_{BSE} is the absolute probability of a BSE with electron energy E_{BSE} landing on this

detection point

E_{SE} is the electron energy of secondary electron when it reaches the detection point

P_{SE} is the absolute probability of a SE with electron energy E_{SE} landing on this detection point
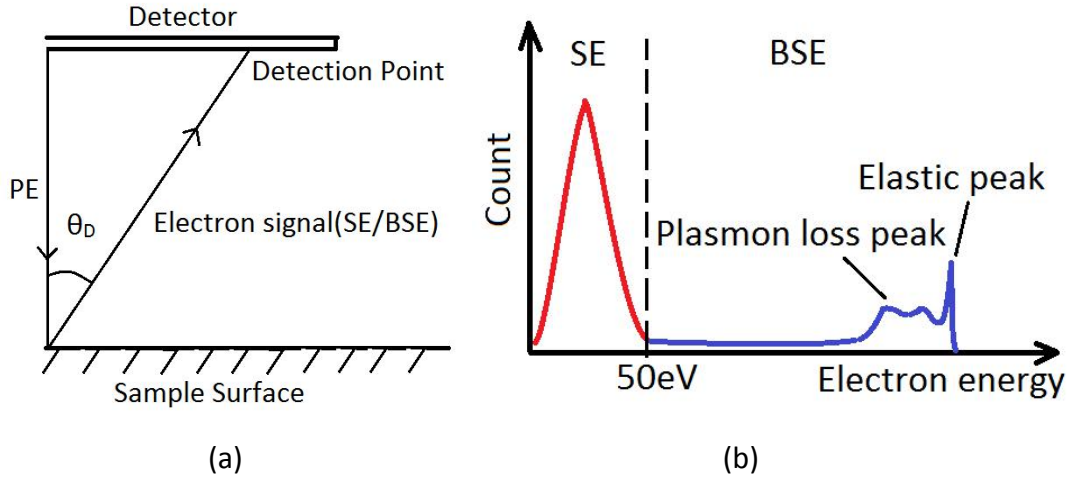
P2 Figure 2.1.1: (a) Schematic representation of the detection point location showing angle θ_D between the primary electron (PE) and the scattered electron and (b) Schematic of electron energy spectra illustrating the SE/BSE energy range

In equation 2.1.2, E_T is a constant for a selected detection point and a given detector. Note that our calculations are restricted to the low-loss electrons (plasmon-loss and elastic peak region, schematically shown in P2 Figure 2.1.1 b)[29]. Thus, E_{BSE} is very close to the landing energy, U_L, of the primary electron. U_L is a parameter that is selected by the SEM user. P_{BSE} is a function of BSE scattering angle, ϑ_{SBSE}, and can be obtained from Monte Carlo simulations[17] using Mott cross-sections. It is based on U_L, and sample composition.

P_{SE} is a function of the SE energy, E_{SE}, and the SE scattering angle, ϑ_{SSE}. The latter can be obtained from Monte Carlo simulation[17] requiring electron energy loss function parameters as input. The details of the Monte Carlo simulation method we applied here are described in detail in literature [30].

In an ideal situation, a selected detection point, ϑ_{SBSE} and ϑ_{SSE} are equal to the detection angle ϑ_D as shown in P2 Figure 2.1.1 a. As P_{BSE} and P_{SE} are both simulated values based on ϑ_D, thus,

$$\left[\begin{array}{l} f(\theta) = P_{BSE} * (E_{SE} - E_T) \\[2ex] g(\theta) = P_{SE} * (E_{SE} - E_T) \end{array} \right.$$

We can simplify the equation 2.1.2 into the form of equation 2.1.3:

$$S_D \propto f(\theta_D) + \int_0^{E_{SE\max}} g(\theta_D) dE_{SE} \qquad\qquad 2.1.3$$

E_{SEmax} is the maximum energy of SE. Generally, 50eV is used[4].

S_D only accounts for the signal strength taking into account an emission point and the related detection point. In reality, the electrons are emitted into a volume of which we can only access the solid angles the detector covers[16]. Therefore, we define the experimentally accessible effective signal strength, S_E and use this parameter instead of S_D in the following calculation, as described in following equation:

$$S_E = S_D * \cos^2\theta_D \propto [f(\theta_D) + \int_0^{E_{SE\,max}} g(\theta_D)dE_{SE}] * \cos^2\theta_D \qquad 2.1.4$$

2.2 Calculating the detected electron signal based on electron emission in a beam deceleration field

When a deceleration field is applied on the SEM sample, $\vartheta_D = \vartheta_S$ is no longer valid. Hence, estimating S_E, involves a transformation of the electron angular distribution from axis based on ϑ_S to one based on ϑ_D using equation 2.2.1. This is derived more fully in the supporting information for flat sample surfaces and flat detector surfaces which are large enough such that the deceleration field is a uniform parallel electric field E_d, between the surface and the detector plane in which the emitted electron (with charge q) is uniformly accelerated. Then E_d is determined by the working distance, and the applied deceleration voltage, U_d.

$$\theta_D = \tan^{-1}[(\sqrt{2E_e\cos^2\theta_s + 2U_dq} - \cos\theta_S\sqrt{2E_e})\frac{\sqrt{2E_e}\sin\theta_S}{U_dq}] \qquad 2.2.1$$

E_e is the electron scattering energy, which is equal to E_{SE} or E_{BSE}, dependent on its origin.

We obtain an expression with ϑ_D instead of ϑ_S for the effective BSE signal, $S_{E(BSE)}$ as derived in the supporting information and shown in equation 2.2.2.

$$S_{E(BSE)} \propto \int_{\theta_{D\,min}}^{\theta_{D\,max}} [(E_{BSE}\cos\theta_D + U_dq - E_T)\cos^2\theta_D * P_{BSE}(\theta_D)]d\theta_D \qquad 2.2.2$$

The effective SE signal, $S_{E(SE)}$ depends on the value of U_d. When $E_T > U_dq$ +50 eV, the SEs will reach the detector but if their energy is below the threshold, the detector will not yield any SE signal. In the case that the $E_T < U_dq + 50eV$, SEs that reach the detector threshold will contribute to S_E but then becomes a mixed SE/BSE signal. The contribution of the SE to the mixed signal is $S_{E(SE)}$ and given by equation 2.2.3 as described in supporting information SI 2.

$$S_{E(SE)} \propto \int\int [P_{SE} * \cos^2\theta_D * (E_{SE}\cos\theta_D + U_dq - E_T)]dE_{SE}d\theta_D \qquad 2.2.3$$

3. Experimental methods

3.1 Monte Carlo simulation of the scattered electron distribution

The electron emission of the sample was simulated from the Monte Carlo program [18] using the following inputs(full list in P2 Table 3.1.1): the material composition (average atomic number), electron affinity, electron energy loss function (EELF) as well as the impact angle and U_L of the primary electron. Since the Monte Carlo simulation is based on the Mott cross-section for BSE and the dielectric function approach for SE, only full energy loss function (EELF) input for single element materials were used. The EELF inputs are energy, width and strength of each oscillator.

The simulation is based on the electron banding and atomic composition of the material; the crystallinity or orientation is not a direct input parameter. However, such structural differences would affect the density input, thus would lead to a difference in the simulation result. For example, the amorphous/crystalline phases are represented by the respective density inputs in our simulation for P3HT samples in section 4.2.2.

P2 Table 3.1.1 Monte Carlo simulation inputs for various samples

Sample	Amorphous C	Cu	PNIPAM	PEGDA	P3HT
Unit composition	C	Cu	$C_6H_{11}NO_2$	$C_2H_4O_2$	$C_{10}H_{14}S$
Molecule mass (g/mol)	12.011	63.546	113.158	44.050	166.288
Density (g/cm$^{3)}$)	1.700	8.960	1.100	1.120[1]	1.090 (amorphous) 1.132 (crystalline)[3]
Electron affinity /Work function (Ev)	4.260	10			2
EELF oscillator electron energy parameter	6.260, 25.710	17.800, 27.700, 31.500			2.740, 23.400
EELF oscillator width parameter	5.710, 13.330	3.250, 7.100, 61.700			0.325, 16.100
EELF oscillator	0.236, 0.709	0.0281, 0.0925,			0.00899, 0.740

| | | amplitude parameter | 0.928 | | | |

1. The density of PEGDA used in simulation input above is the average density of the composite matrix
2. The average atomic numbers of PNIPAM and PEGDA are respectively 3.26 and 3.42
3. The density of amorphous and crystalline phase P3HT is acquired from literature[31]

The primary electron energy input, E_0, is the landing energy of the primary electron. Thus the simulation result is not affected by a deceleration field for a chosen E_0, and any situation in which the primary electron cannot reach the sample before (e.g. it is deflected by the deceleration field) is not considered here. The electron angular distribution was acquired as the probability for each scattering angle in the range of 0-90°, with a step size of 1°. The electron energy distribution was acquired as the probability of electron energy from 0eV to E_0+5eV (in order to cover the width of the elastic peak), in energy steps of 0.1 eV. The SE distribution was simulated from 0-100eV scattering electron energy in order to cover the tail of SE peak, while the low-loss BSE were simulated from E_0-100eV to E_0+5eV in order to cover the plasmon-loss and elastic peak. In the case of the electron energy-angular distribution of SE, the data was acquired from simulating the angular distribution of 0-1eV, 1-2eV, ..., 99-100eV scattered electrons. Every 1 eV step and the distribution was built from the collected probability points in an electron energy-scattering angle-probability coordinate system. The data sets acquired from simulation was plotted and processed with Savitzky-Golay smoothing.

3.2 Sample materials

The Cu and amorphous C sample used, obtained from Agar, were 200 Mesh TEM copper grids with carbon film. The carbon film had a thickness of 13nm (which is smaller than the maximum penetration depth of a 2keV electron beam.) In order to prevent the electron signal transmission, we created another 4μm thick C layer by an Emitech C coater, the layer thickness requirement is discussed in SI 3. The electron implantation and the "bulk" thickness requirement is simulated by Monte Carlo simulation. Detail of relationship between film thickness and electron interaction is discussed elsewhere[32].
The PNIPAM/PEGDA semi-interpenetration network was fabricated with highly branched PNIPAM and a PEGDA matrix. Synthesis of the PNIPAM system is described elsewhere[33]. The PNIPAM concentration of the sample investigated was 20% wt. To enhance conductivity and remove contamination, the PNIPAM/PEGDA samples were plasma etched in air by a Diener Zepto version B (840s and 100W power.)

The P3HT was purchased from Ossila, brand Merck SP001 94.2% regioregularity and M_w=54,200 Da and spin coated on silicon substrate from solution. The detail of the P3HT film is described elsewhere[34].

3.3 SEM image acquisition

The SEM images were taken in a FEI Nova450 SEM. The contrast and brightness setting of the microscope was set to fixed values for each CBS detector segment in all data sets. The background subtraction of the images was done by taking reference images with beam blank for every setting in the imaging process. The detection angle of each CBS segment is calculated from the detector segment size and microscope working distance as shown in P2 Figure 3.3.1, while the detector segment size is measured from an image of the CBS detector. In order to change the detection angle, the microscope was operated to record images from a series of working distances with fixed U_L and U_d.

All data sets were acquired with fixed U_L and either 1) fixed U_d while changing the detection angle ϑ_D or 2) changing U_d with fixed ϑ_D.
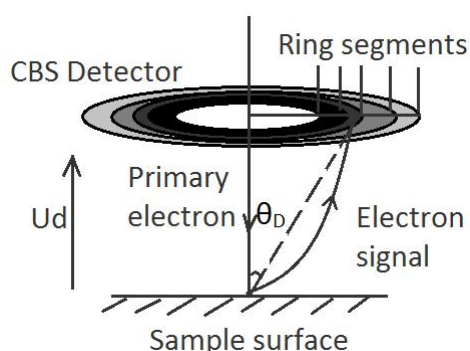
P2 Figure 3.3.1: A schematic of the parameters of CBS detector, the ϑ_D can be directly calculated from working distance and segment location.

The measured grey value extracted from the image (8 bit) using ImageJ 1.48v software represents the signal intensity S. Grey values for all individual pixels were averaged from the entire field of view before the reference value is subtracted. This reference value is determined by averaging all grey values present in an image with same field of view and identical microscope settings but with a blanked beam.

4. Result and Discussion

4.1 The comparison of simulation and experimental data of SEM signal on a single element material

In order to test the feasibility of the simulation, we investigated two single element materials: Cu as an example of a heavy element and amorphous carbon as an example of light element. The data of these two samples is well established in literature [35][36][37] and was used to provide a good comparison between our simulation and experimental data.

4.1.1 Comparison of simulation and experimental non-decelerated BSE signal

P2 Figure 4.1.1 a, c are plots of experimental BSE signal versus the simulated signal calculated from MC simulation from the 17º to 38º ϑ_D range. We note that the experimental intensity vs simulated intensity data remains linear from 18º to 32º for Cu (see P2 Figure 4.1.1a) and 17º to 34º for amorphous C (see P2 Figure 4.1.1c).

At larger ϑ_D, the experimental signal intensity drops noticeably below the predictions from MC simulations. We consider the angle up to which the prediction fits as the upper limit of the angular range for which our model is valid. We have not observed any signal intensity deviation from our predictions at the minimum accessible angle (17º) of our detector. As shown in P2 Figure 4.1.1 b, d, the shaded area is the actual valid prediction zone in the simulated intensity angular distribution curve for our CBS detector in the absence of a deceleration field. In the absence of a deceleration field any SE contribution to the signal can be ignored as it is below the detector energy threshold E_T, which we estimate to be around 400 eV from our imaging experiments.
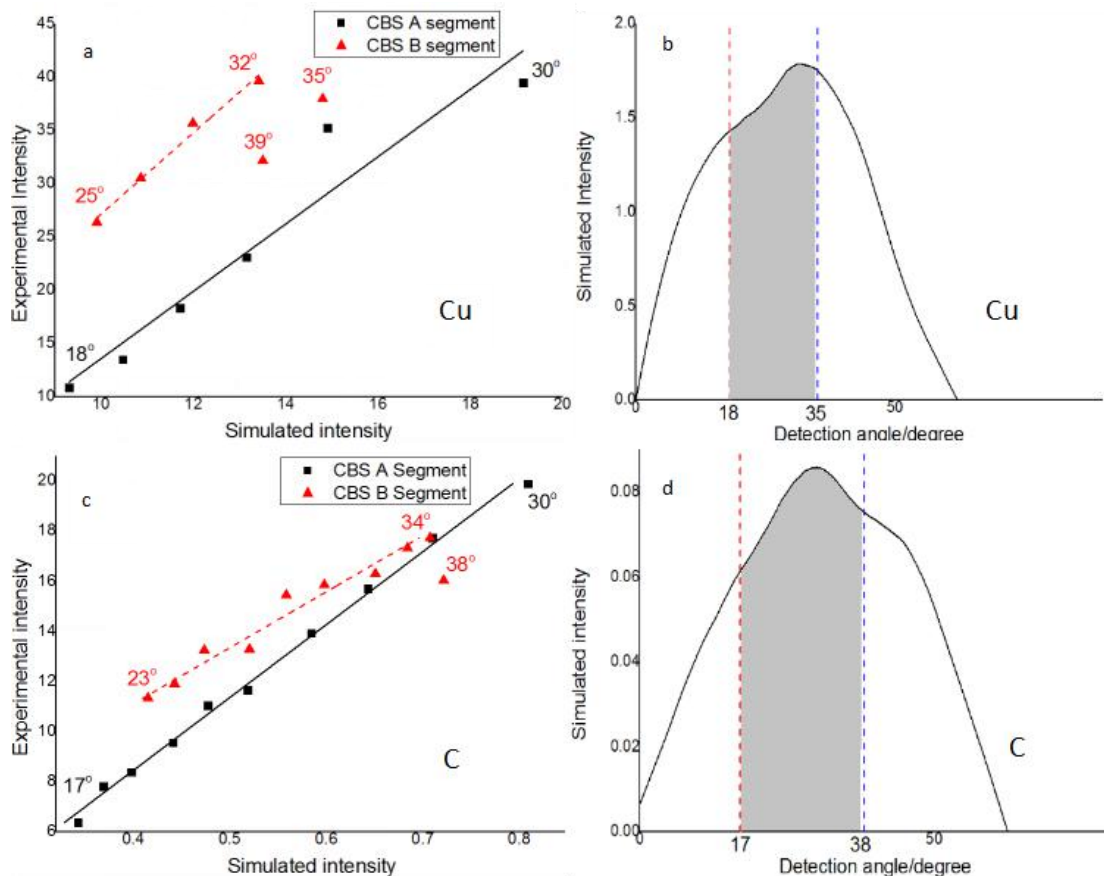

P2 Figure 4.1.1: (a,c): Plots of experimental (U_L = 2000eV, U_d = 0) intensity versus the simulated intensity of Cu (a) and amorphous C (c); (b ,d): Simulated SE$_{(BSE)}$ signal as function of ϑ_D for Cu (c) and amorphous C (d), the shaded areas indicate the range of experimentally accessible angles for which the simulation method remains valid.

4.1.2 The prediction of the influence of the SE signal in a decelerated SEM imaging process

The SE signal can exceed the detector threshold of a BSE detector if the applied deceleration field results in SE energies larger than E_T+50eV, thus the simulation of the SE signal is required for the identification of signal detected in these situations. The simulation of SE signal relies on the energy-angular distribution of SE emission. This is shown in P2 Figure 4.1.2 (a) the SE distribution is focused in a small energy range below 30eV for the Cu sample with U_L 2000eV. The SE distribution covers the whole angular range of 0-90° but reaches a maximum at around 40°. $S_{E(SE)}$ only contributes to S_E if two conditions are fulfilled, that is, the threshold of the detector needs to be exceeded and the maximum ϑ_D is brought within the angular range of the detector through the effects of E_d. Since E_d is perpendicular to the detection plane and much larger than the SE energy, the actual $S_{E(SE)}$ is very small. For example, for Cu with $U_L = 2000eV$ and $U_d = 1000V$ deceleration field, an SE with 50eV energy would have the maximum ϑ_D when it is emitted parallel to the detection plane. That ϑ_D would then only be 17° which is the lower limit for the CBS detector in our microscope.

As shown in P2 Figure 4.1.2 (b), the SE will only form a large signal in very small detection angular range below 10° for the Cu sample. Although other materials have different SE distribution, the SE detection range is still always limited below 15° for all our samples and microscope settings. The SE signal intensity peak also shifts to smaller ϑ_D if the U_d is increased, and so the SE signal can safely be ignored.
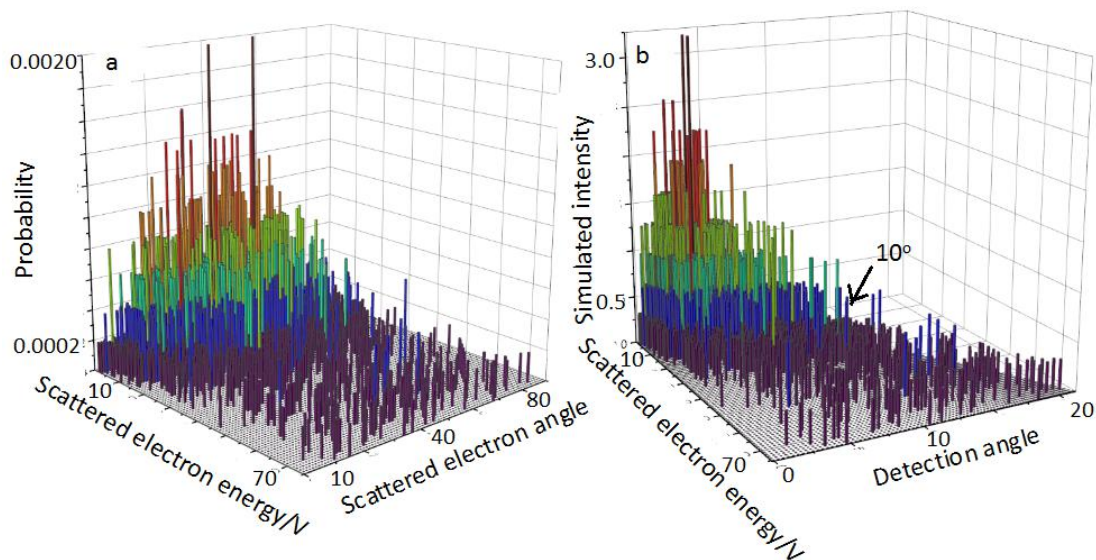
P2 Figure 4.1.2: (a) The electron energy-scatter angular distribution of Cu with $U_L =$ 2000eV, U_d=0V; (b) the simulated $S_{E(SE)}$ distribution of the same sample when $U_d =$ 1000V. The scatter in the higher energy (50-80eV) part of the data is a result of the very low electron probability (<0.0002 for each scattered purple data point and <0.5% of the total SE emission) as shown in (a).

4.1.3 Comparison of simulation and experimental decelerated BSE signal

As shown above, the SE signal can be safely ignored for the CBS detector in our SEM conditions, even if a deceleration field is applied. Hence the main difference of the results presented in section 4.1.1 (where $U_d=0$) is a substantial increase in $S_{E(BSE)}$ that falls within an angular range of our CBS detector (compare P2 Figure 4.1.1 a,c ($U_d = 0$ V) and P2 Figure 4.1.3 a,c ($U_d = 1000$ V)). However, according to the experimental versus simulated data plot shown in 4.1.3 a, c, the valid ϑ_D range for simulation to match experiment is still limited to around 35° for both the Cu and the amorphous C samples. Furthermore, slight changes in the angular distributions are visible when comparing P2 Figure 4.1.1 b,d ($U_d = 0$ V) and P2 Figure 4.1.3 b,d ($U_d = 1000$ V). Note especially the more pronounced peaks and shoulders appearing in P2 Figure 4.1.3 b,d. The detection angle zone that is validated by our experiment (shaded in grey in P2 Figure 4.1.3 b,d) still extends just past the maximum for Cu in P2 Figure 4.1.3b and the first peak in P2 Figure 4.1.3.d obtained for amorphous C. For larger angles, the experimental intensity still drops rapidly below the predicted value for angles larger than 35° for Cu and 38° for C sample (Figs. 5.1.3 b,d).
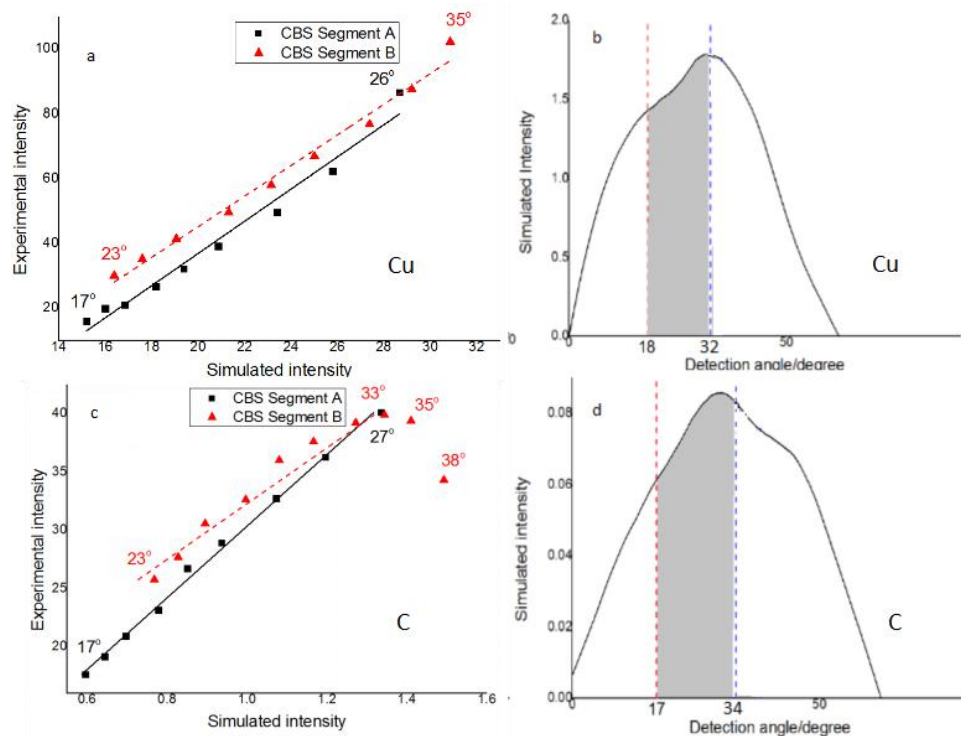

P2 Figure 4.1.3: Plots of experimental (U_L = 2000eV, U_d = 1000 V) intensity versus simulated intensity of Cu (a) and amorphous C (c); (b ,d): Simulated $SE_{(BSE)}$ signal as function of ϑ_D for Cu (c) and amorphous C (d), where the shaded areas indicate the range of experimentally accessible angles.

4.1.4 The estimation and effect of angular distribution of the BSEI and BSEII signal

As mentioned in the introduction, the BSE emitted from the very top surface of a

specimen forms a signal which is topography dependent. This BSEI signal is emitted at a large scattering angle. If we plan to acquire a BSE image with solely compositional contrast, we need to collect the BSEII signal which is emitted from beneath the sample surface. The BSE emission simulated from different layers within the specimen from 0 nm-0.5nm to full penetration depth of Cu and C. As shown in P2 Figure 4.1.4 a, c, the scattering angle of the highest electron probability/intensity shifts from 83° to 75° for C and 76° to 51° for Cu. The same trend is also observed in P2 Figure 4.1.4 b, d for the simulated relative BSE intensity when a U_d = 2000 V is applied.

Although there is no clear boundary for the BSEI and BSEII, the electrons emitted from the first 3nm of the sample surface have an emission depth which is very similar to SE and can be expected to contribute to the topographical contrast of BSE images. As can be seen from P2 Figure 4.1.4. the BSEI signal constitutes a large fraction of $S_{E(BSE)}$ for both C and Cu. Hence in these cases, topography can significantly affect BSE imaging. This effect can be noticed as shoulders or even double peaks in the BSE angular distribution curve such as in P2 Figure 4.1.3 b, d. The fact that BSEI is the dominant signal for BSE detection at large angles (see P2 Figure 4.1.3 b, d) also explains the substantial deviation of simulated intensity from experimental data for larger ϑ_D as we do not control the surface topography. Hence nano-scale topography limits the validity of our prediction range of angles just below the first peak in the angular emission plots. For this range, the BSE image contains purely compositional information. The more this angular range is exceeded toward larger angles, the stronger the contribution of topography to the detected BSE signal. This effect can indeed be exploited for the measurement of nano-scale topographical features as reported in[12]. Importantly, this shows that by correctly choosing the maximum $\vartheta_{D,}$ topographical and compositional contrast can be selected. As the SEM user does not select this angle directly but needs to achieve it through the correct combination of working distance, U_L, U_d and detector segment, this model can be used to predict the best combinations for maximum compositional contrast.
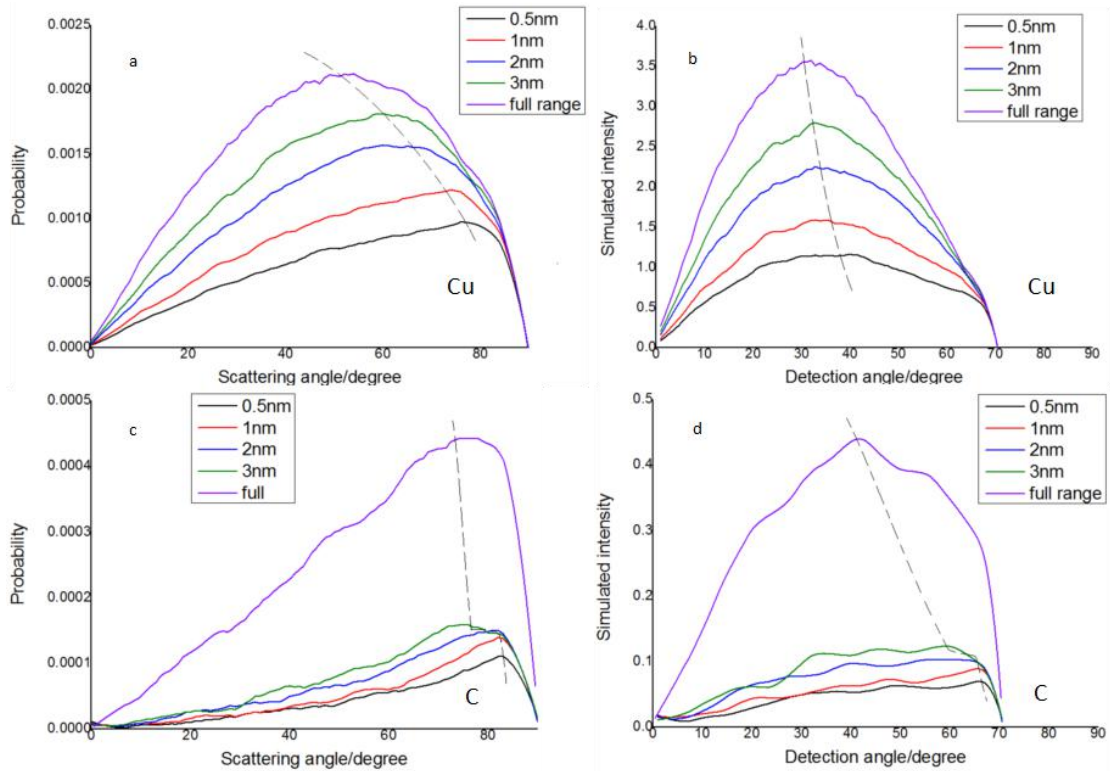
P2 Figure 4.1.4: (a,c) The simulated BSE angular emission with varying thicknesses of emission layer for Cu (a) and C (c) at U_L= 2000 V; (b, d) Simulated intensity based on emission shown in (a,c) when U_d = 1000 V. The peak of each angular distribution curve has been connected by a dashed line. The full range curve represent the full implantation range BSE, which is a reflection of BSEII in this case.

4.2 Application of model for the optimisation of compositional BSE signal on complex nanostructured materials- PNIPAM/PEGDA semi-IPN and regioregular P3HT film

Section 4.1 shows that in the cases of single elemental samples of Cu and amorphous C, the prediction of the BSE signal intensity is reliable in the angular range from largest SE detection angle to the first maximum in the simulated angular distribution. As shown by the results of the Cu sample this simulation can be applied to heavier elements, but our main purpose is the optimisation of polymer imaging as these are the most challenging of materials due to often minute differences in average atomic numbers.

Here we extend the same prediction, thus the microscope setting (detection angle limitation) for a guaranteed optimisation of composition contrast can be achieved to exclude contributions from topography.

4.2.1 Verification of simulated BSE signal and experimental signal of a PNIPAM/PEGDA semi-IPN

The same verification method used in 4.1 to check the feasibility of our prediction has been applied on the PNIPAM/PEGDA semi-IPN samples and the plot of the simulated intensity versus experimental grey value is shown in P2 Figure 4.2.1. The

highest usable primary beam voltage for this polymer composite is limited to around 1kV due to charging effects. The experimental signal for this condition without deceleration field is very small and the imaging at U_d=0V is not practical. Hence the only data checked for the PNIPAM/PEGDA sample are those with deceleration applied using the methods of section 4.1.3.

The PNIPAM simulation in P2 Figure 4.2.1 compares and fits the experimental data to the maximum angle of around 29°. The angle that this linear relationship ends is around the same value for both the A and B segment in our CBS detector. The PEGDA simulation only fitted with experimental data to the maximum angle of around 26°, which resulted in the simulation deviating from linear relationship in almost the entire angular range of the B segment (23-40°).
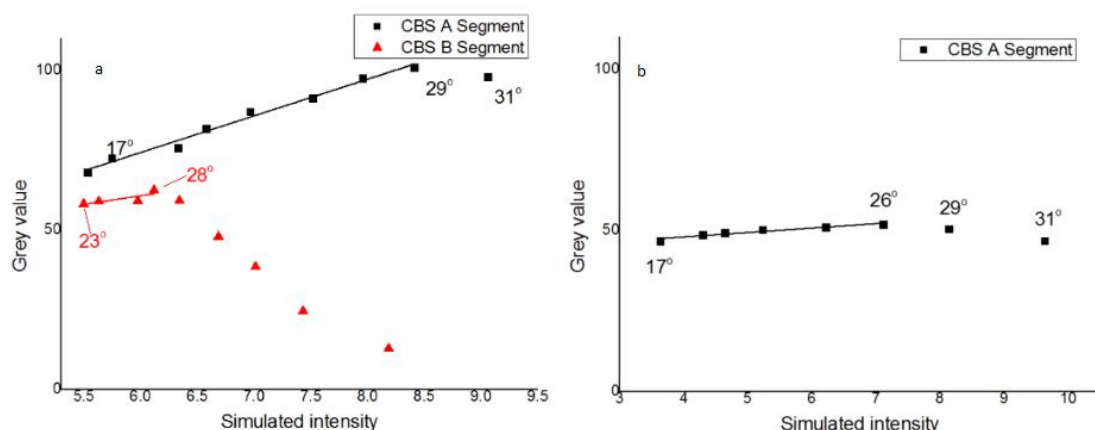
P2 Figure 4.2.1: The plot of simulated BSE signal intensity with the experimental image grey values using U_L =1000V and U_d = 4000 for (a) PNIPAM and (b) average value of PEGDA matrix.

P2 Figure 4.2.2 a is an image taken within our predictable angular range that results in compositional contrast. This polymer composite contains PNIPAM particles with size from 50-200nm as well as smaller 30-50nm features in PEGDA matrix. PNIPAM particles (indicated by the arrows) yielded larger signal than any part of the PEGDA, as expected from results in P2 Figure 4.2.1. The same locations are indicated in P2 Figure 4.2.2 b, which was taken at angles exceeding our predictable range, and thus contain little compositional contrast. The contrast is mainly formed by the topography difference between different phases created in etching and indeed the small PNIPAM particles are barely visible. The larger PNIPAM particle at the centre of the image can mainly be recognised by its bright edges. The line profiles of the two images in 4.2.2 b, d also confirm this. The appearance of edge effect (the high brightness edge formed at steps on sample surface due to the small emission depth of the relevant electron signal [38]) is a clear sign of the appearance of topographical contrast. Since the large angle signal is dominated by BSEI, the topographical BSE images for large angle agree with our expectation based on simulation in 4.1.4. Thus we can use the BSE below the simulated peak in the angular distribution for composition contrast imaging and select the BSE at large angles for topographical

imaging.
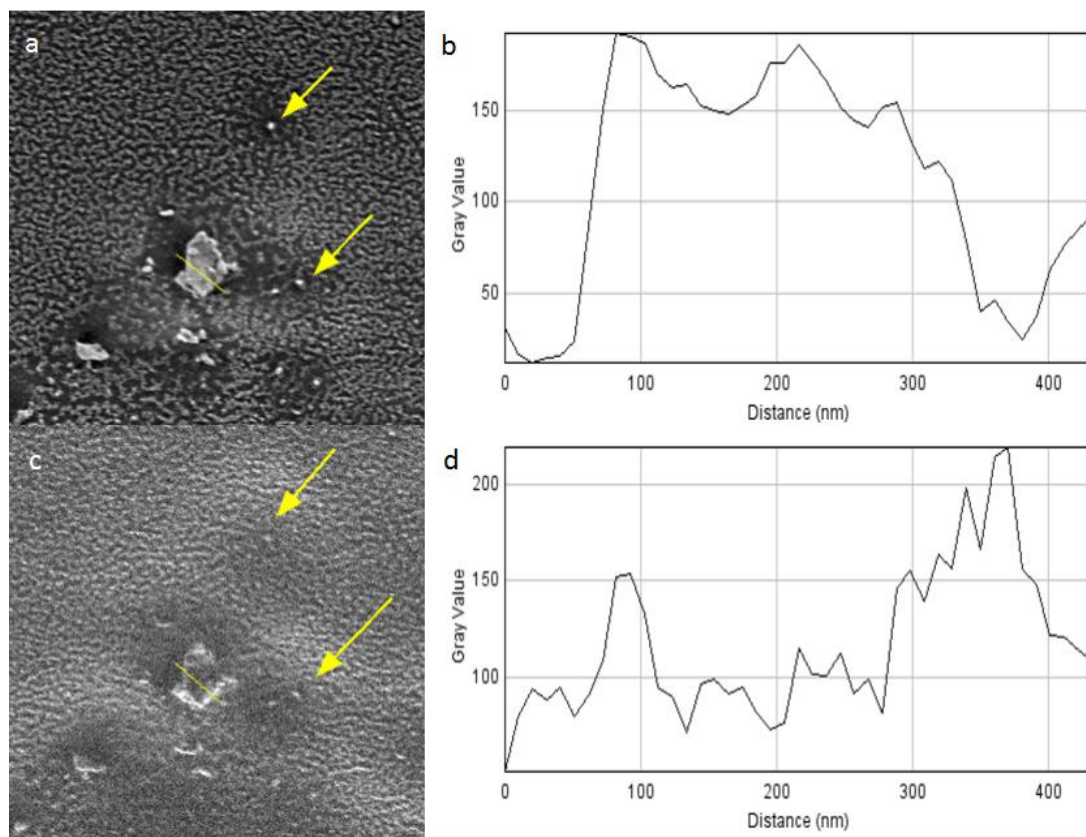
P2 Figure 4.2.2: The CBS image of the surface of PNIPAM/PEGDA sample from (a) segment A (14-22°) and (c) segment D (30-36°) both with U_L = 1000 V and U_d = 4000 V. The field of view is 3*3μm². The location of small PNIPAM particles are highlighted by arrows; (c,d) are the corresponding line profiles of the larger PNIPAM particle in (a) and (c)

4.2.2 Limitation of the signal prediction

Comparing the data acquired from the PNIPAM/PEGDA sample (P2 Figure 4.2.1) and the single elemental samples of Cu and C (P2 Figure 4.1.3), the viable angular range of our prediction method changed dramatically for each different material and different imaging conditions. However, this viable angular range is closely related to the simulated angular distribution peak in our simulations. The maximum angular range are shown in P2 Table 4.2.1, this maximum viable angle value always matches the peak position of the simulated intensity distribution curve (shown in P2 Figure 4.1.4) as the maximum in the BSEII peak and highlighted by the dashed line.

As stated earlier in 4.1.2, since the energy of the major part of the SE is always around 0-50eV, we always expect the SE to be limited to very small angular range (<10°) for any U_d above 1000V. Hence we can conclude that the viable angular range for our BSE signal prediction is from 10° to around the angle of the simulated angular distribution peak.

Ideally for a known material, the detection angle limitation can be chosen at the angle of the simulated angular distribution peak that is obtained from the simulation. We demonstrate this on the example semicrystalline polymer presented in section 4.2.4.

P2 Table 4.2.1: Comparison between the peak position in simulated angular distribution and the maximum reliable prediction angle obtained from experiment.

Specimen	Simulation Intensity peak position / degree	Experimental Maximum reliable angle for our prediction/ degree
Cu	32	32
C	31	34
Cu (U_d=1000V)	34	35
C (U_d=1000V)	33	33
PNIPAM (U_d=1000V)	28	29
PEGDA (U_d=1000V)	24	26

4.2.3 Microscope settings for optimised signal simulation of PNIPAM/PEGDA semi-IPN

According to 4.2.2, we can estimate the expected angular range for our BSE signal for known microscope settings and materials. Since the angular range in our CBS detector is fixed, the working distance is changed in order to select the ϑ_D range as shown in P2 Figure 4.2.3. To utilise this figure for the optimisation of compositional contrast we must use the range in which topography will not affect the contrast. This range is based on the results of P2 Figure 4.2.1 and indicated by striped lines in P2 Figure 4.2.3. It can be seen that the detector segment A can deliver compositional contrast over a much wider range of working distances than segment B. However, the simulations in P2 Figure 4.2.3 a and c show that the compositional signal intensity obtainable with detector segment B is substantially higher than that from segment A, due to a slower reduction trend of the overall intensity in segment B as ϑ_D decreases. This leads to higher noise-signal ratio in high contrast setting in segment A and makes segment B a more suitable segment for high contrast imaging at large working distances, as shown in experimental data in P2 Figure 4.2.4a. This situation demonstrates the complexity of optimising the contrast on an experimental basis. A further parameter that the user has to decide is U_d, which can also have a substantial influence (see P2 Figure 4.2.4b).

Moving from overall simulated signal intensities to simulated contrast, where

contrast is defined as $\quad C = \dfrac{S_2 - S_1}{S_2}\quad$ (S_1, S_2 is the grey value of different areas, S_2>S_1)

[17]. The simulated contrast can be plotted as a function of both U_d and ϑ_D (see P2 Figure 4.2.5 a). This plot immediately indicates on how to maximise the contrast. However, we need to bear in mind that only a limited angular range delivers pure

compositional contrast. Therefore, in P2 Figure 4.2.5 b the line of maximum reliable contrast is projected into the U_d versus ϑ_D plane and plotted. Any microscope settings that lead to detection within the striped area in P2 Figure 4.2.5. will give pure compositional contrast. Maximum compositional contrast is obtained with settings approaching the line of maximum contrast from the smaller ϑ_D. Thus we can select any experimentally realisable ϑ_D - U_d pair near this curve for optimised compositional imaging. This ϑ_D can be directly transferred to the location of concentric ring detector segment based on the location of working distance setting as mentioned in calculation 2.2. Since the concentric ring detector has an angular range, in order to acquire reliable compositional contrast, maintaining the maximum ϑ_D of the chosen segment in P2 Figure 4.2.5 a is suggested. The position of this curve for a given set of materials is determined by the highest angle for valid compositional contrast prediction of this material system. This can be experimentally verified as shown in P2 Figure 4.2.1.

For some settings within the predictable zone in P2 Figure 4.2.5 b, the contrast could reach higher values than our suggested setting as the total signal intensity drops at low U_d and low θ_D. However, as shown in P2 Figure 4.2.6 c, this higher contrast is accompanied with a low signal intensity and hence low signal to noise ratio. Our suggested setting at the maximum valid angle provides a high intensity difference and a high total signal intensity as shown in P2 Figure 4.2.6 a.

Our simulated optimised contrast settings in P2 Figure 4.2.5 (b) were compared with the experimental optimised contrast setting for PNIPAM/PEGDA specimen. The experimental optimised contrast setting was acquired from contrast-U_d plot at working distance 4.5 mm-6 0 mm similar to the plot in P2 Figure 4.2.4 (b). As shown in P2 table 4.2.2, the experimental and estimated optimised setting agrees well. The absolute deviation from our estimated setting is about 200V to 300V for most conditions. Therefore, higher U_d results have shown smaller relative differences to our simulations. We recommend that this simulation method be used for the optimisation of the compositional contrast collected from specimens with small compositional changes. It can be directly translated into suitable experimental settings using plots such as shown in P2 Figure 4.2.5 a, b. In this way, polymer nanoparticles in multi-phase polymer systems can successfully be predicted, imaged and identified.
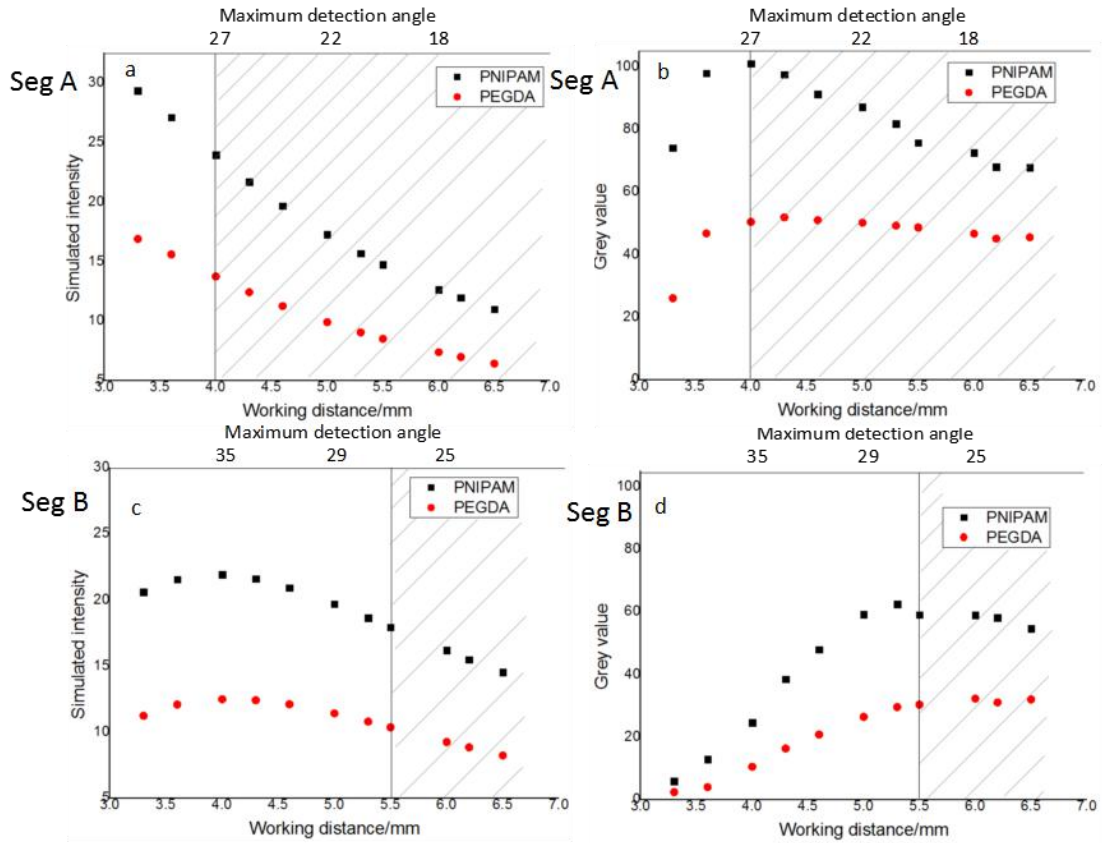
P2 Figure 4.2.3: (a) Simulated intensity for PNIPAM and PEGDA with U_L = 1000V and U_d = 4000V using segment A of CBS; (b) Experimental image grey values for same conditions as in (a); (c) as (a) but using segment B of CBS; (d) as (b) but using segment B of CBS. The predictable zone for our model is marked by the striped area.
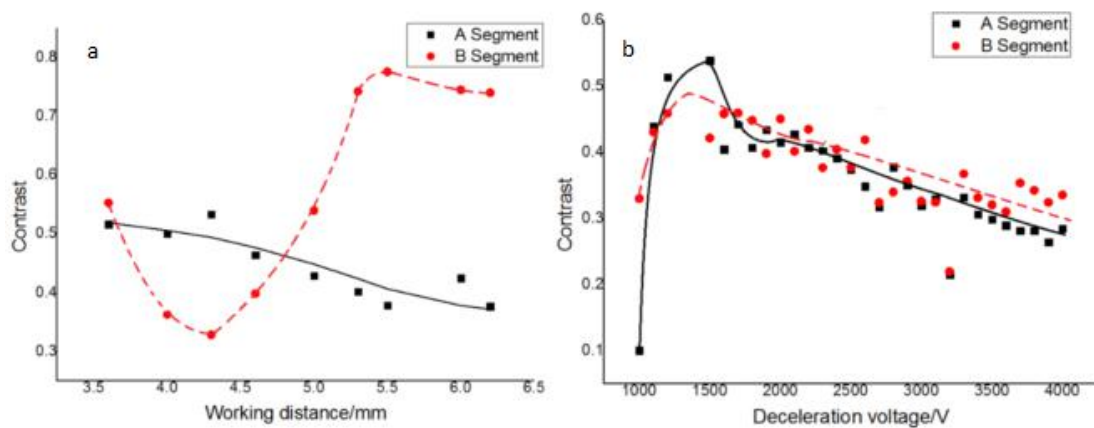
P2 Figure 4.2.4: BSE images collected with CBS segment A and B at U_L= 1000 V (a) Experimental contrast between PNIPAM and PEGDA versus working distance; (b)
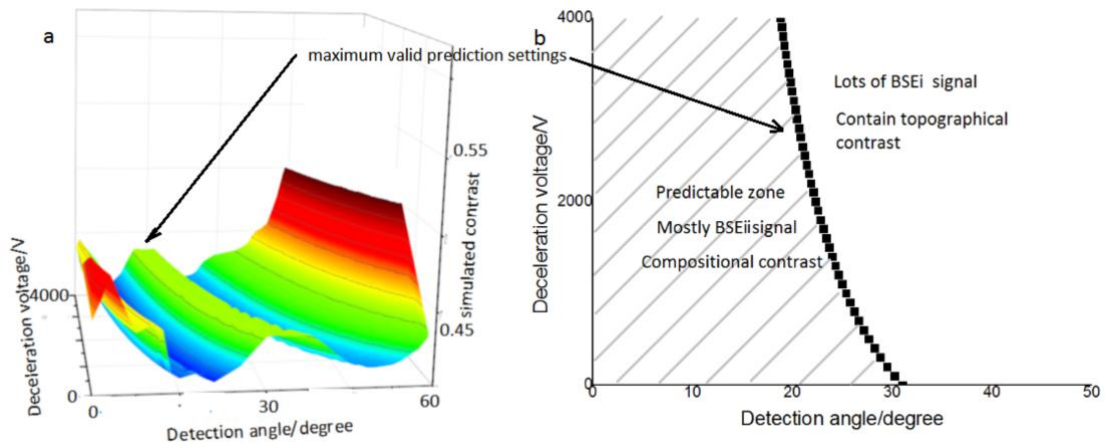
P2 Figure 4.2.5: The BSE simulated contrast vs U_d and ϑ_D of PNIPAM/average PEGDA matrix (a) in 1000V U_L condition. The contrast peak position was projected as a curve in 2D θ_D-U_d plane (b). The predictable zone is marked with striped area in d. Note the U_d is limitation by the accessible range of the microscope.
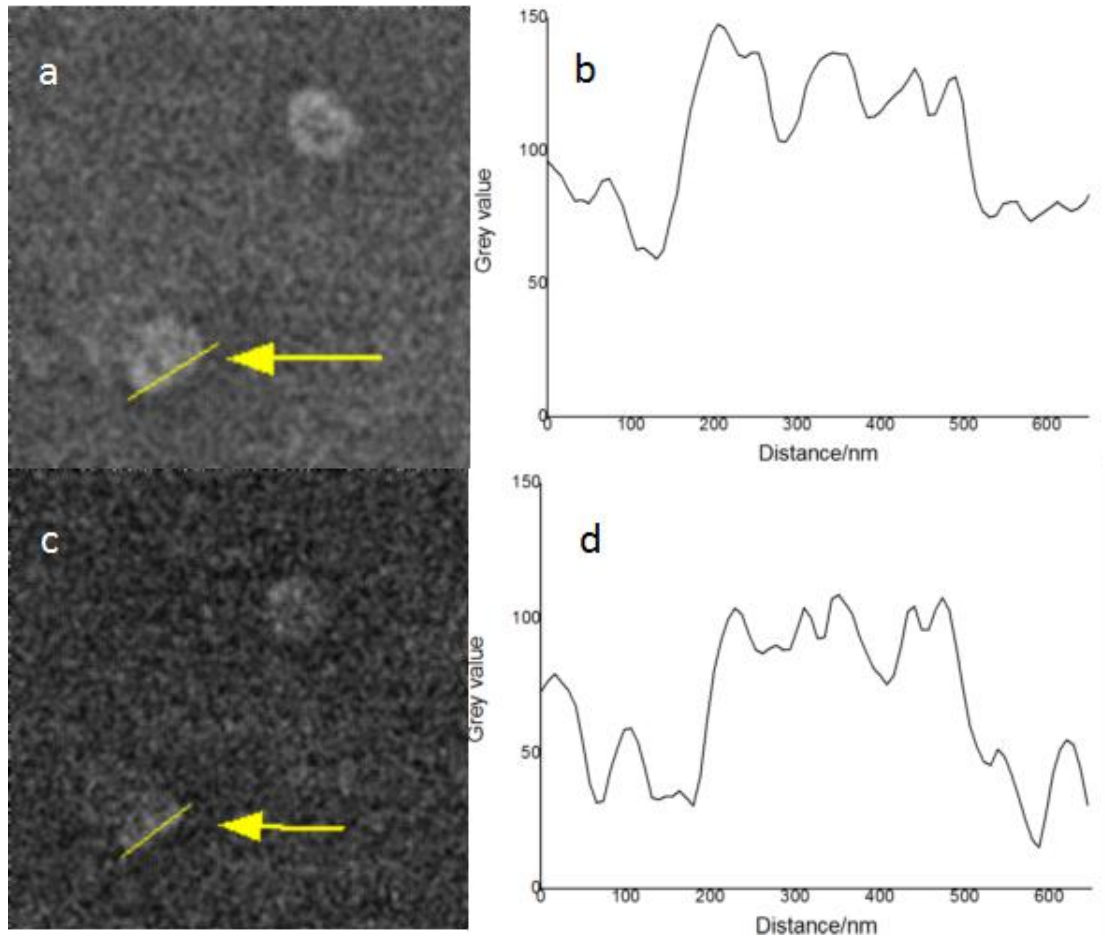
P2 Figure 4.2.6: The images a and c are CBS B segment images taken at U_L=1000V working distance 4.5mm for PNIPAM/PEGDA sample. The Ud is 3000V for image a and 1700V for image b. The figure b and d show the corresponding line profiles of the PNIPAM particle on image a and c, the line is indicated by arrow on image a and c. The field of view is 2*2μm$^{2.}$

P2 table 4.2.2: The comparison between estimated and optimised experimental settings for PNIPAM/PEGDA sample from working distance 4.5mm to 6mm

| Working distance (mm)	Simulation Optimised deceleration voltage (V)		Experimental Optimised deceleration voltage (V)	
	Segment A	Segment B	Segment A	Segment B
6	_2	3214	_1	3500
5.5	4729	2235	_1	2500
5	3890	1461	4000	1800
4.5	3119	841	2900	1100

1. These values exceed the upper limits of the deceleration voltage obtainable in our microscope

2. This voltage is over 10kV and exceeds our assumption of the electron speed in primary beam axis $v_{ey}<15\%c$ (c is speed of light) as mentioned in supporting information 1.

4.2.4 Application of model to imaging crystallinity in regioregular P3HT film

Another example application of this method is P3HT which is a conjugated, semiconducting polymer commonly used as a film in organic electronic devices. It has a semicrystalline structure and the level of crystallinity in a P3HT film is strongly linked to its performance in electronic devices[39]. Generally, higher crystallinity in a P3HT film gives an improved charge mobility and stability. Therefore, many techniques are employed to determine the amount of crystalline phase in P3HT, but often with very different results even when measured on the same sample [40]. The often large differences are explained due to the differences in length scales that such techniques use on one hand and a more complicated scenario than a two phase model [40]. Thus here we apply our simulation to establish if crystallinity mapping via BSE imaging of a P3HT is feasible in the SEM as the latter would offer the possibility to explore crystallinity distributions on various length scales.

The microscope setting is selected by the same method described above in 4.2.3 and chosen as CBS segment A, U_L=1000V, U_d=4000V at working distance 4mm, the settings for the crystalline and amorphous phase are simulated based on the density differences. As shown in P2 figure 4.2.7 a, we have collected the highest possible BSE signal for our detector segments below the angular distribution peak of BSEII. Thus a crystallinity map can be formed according to the contrast between the crystalline and the amorphous phases of P3HT. As the crystalline P3HT has reportedly a higher density the (see P2 Table 3.1.1) our simulations predict that the crystalline phase appears brighter in the image in P2 figure 4.2.7b. By analysing cystallinity mapping image collected on P3HT, associated histogram of the image can be fit into two gaussian peaks as shown in P2 figure 4.2.7 c. Thus we obtain the following: minor component (crystalline, ~23%) and major component (amorphous ~77%) from the respective peak areas . This composition is within the range of reported phase compositions and very close to that obtained from density measurements presented

in [40]. However, our method allows us to investigate the lateral distribution best seen by thresholding the image as in P2 figure 4.2.7 d. to some extent.   There is some overlap between the two components for grey levels below 150 , we have set our threshold at 155 so to avoid such overlap. Hence, the black areas in P2 figure 4.2.7 only represent the proportion of crystalline material that can be identified as such with confidence. In this context it is interesting to note that [40] suggest that a two phase model for crystallinity in P3HT might be to simplistic and and intermediate degree of ordering might be present, which seem to be consistent with our observation so far.   However, a much more detailed study on P3HT with different proportions of crystallinity due to different molecular weights and processing conditions, investigated at a wide range of length scales (magnifications) would be needed to test the model put forward in [40]. This is beyond the scope of this work. The focus here is to show that our method (using simulation to ensure nano-scale chemical imaging for phases with small chemical changes) provide a new tool to investigate the subject of local crystallinity, which is of extreme importance to the field of organic electronics.
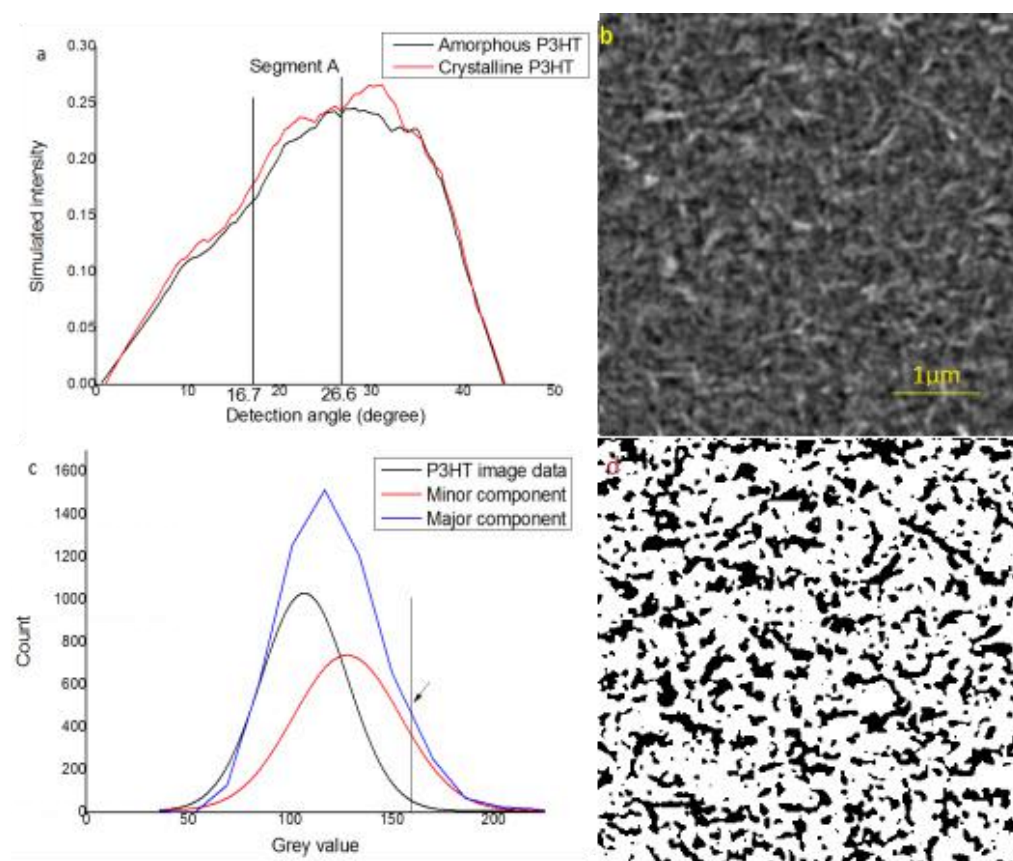
P2 figure 4.2.7: The optimised microscope setting chosen for P3HT is the CBS segment A, as shown in a, this is between the minimum detector angle and the maximum valid angle (the angular distribution peak in this curve). The crystallinity distribution imaged with our setting is shown in b, the field of view of SEM image is $5*5\mu m^2$. The histogram of the image was fit to two gaussian peak for major and minor component in c, and by choosing threshold at the pointed grey value the crystallinity mapping can be acquired as shown in d. (The image b is provided by R.

Masters)
Conclusion

Monte Carlo simulations of amorphous C, Cu, PNIPAM/PEGDA semi-IPN and P3HT film angular distributions of emitted electrons in a low voltage SEM have been shown. We report how to transform the simulated angular distributions to account for particular microscope settings (such as detection geometry and deceleration field,) enabling a direct comparison to experimental data and establish the angular range for which the model can be used. We found that the BSE emission for angles below the peak in the angular emission spectrum can be accurately predicted and used for contrast optimisation of compositional imaging. The BSE emission at angles larger than the peak in the angular spectrum do not match the simulations and are shown to contain mainly topographical information. Although the signal related to this part of the angular emission spectrum is not predictable by our model, the model can predict the experimental parameter range in which topographical features will influence the contrast in BSE images.

In summary our model allows us to optimise and separate compositional and topographical contrast in angle selective BSE imaging in the presence of a deceleration field. This approach can be used to solve the challenge of imaging small differences in nano-scale chemical compositions in carbon based composites or local crystallinity in semi-crystalline polymers.

Reference

[1] Vezie D L, Thomas E L, Adams W W, 1995 *Polymer*, **36** 1761

[2] Pawley J B, 1992 *Microelectronics and Microscopy*, **83** 203

[3] Boyes E D, 2000 *Microsc. Microanal*, **6** 307

[4] Seiler H, 1983 *J. Appl. Phys.*, **54** R1

[5] Wuhrer R, Moran K, 2016 *IOP Conf. Ser. Mater. Sci. Eng.*, **109** 012019

[6] Gaillard C, Stadelmann P A, Plummer C J G, Fuchs G, 2004 *Scanning*, **26** 122

[7] Jaksch H, Martin J P, 1995 *Anal Chem*, **353** 378

[8] Butler J H, Joy D C, Bradley G F, Krause S J, 1995 *Polymer*, **36** 1781

[9] Boyes E D, 1998 *Adv. Mater.*, **10** 1277

[10] Lewis P, Micklethwaite S, Harrington J, Dixon M, Brydson R, Hondow N, 2015 *J. Phys: Conf. Ser.*, **644** 012019

[11] Bongeler R, Golla U, Kassens M, Reimer L, Schindler B, Senkel R, Spranck M, 1993 *Scanning*, **15** 1

[12] Kieft E, Bosch E, 2008 *J. Phys. D: Appl. Phys.*, **41** 10

[13] Czyzewski Z, O'Neill M D, Romig A, Joy D C, 1990 *J. Appl. Phys.*, **68** 3066

[14] Murata K, Kawata H, Nagami K, Hirai Y, Mano Y, 1987 *J. Vac. Sci. Technol. B*, **5** 124

[15] Pasciak A S, Ford J R, 2006 *Scanning,* **28** 333

[16] Merli P, Migliori A, Morandi V, Rosa R, 2001 *Ultramicroscopy*, **88** 139

[17] Wan Q, Plenderleith R A, Dapor M, Rimmer S, Claeyssens F, Rodenburg C, 2015 *J. Phys: Conf. Ser.*, **644** 012018

[18] Mitsuo Suga et al, 2014 *Progress in Solid State Chemistry*, **42** 1

[19] Richard R G, Owen G Rh, Gwynn I Ap, 1999 *Scanning Microscopy*, **13** 55

[20] Joy D C, 1991 *J. Microsc.*, **161** 343

[21] Cazaux J, Kuwano N, Sato K, 2013 *Ultramicroscopy*, **135** 43

[22] Sakic A et al, 2011 *Micro Technology and Micro Devices SAFE, 1-4*

[23] Mullerova I, Konvalina I, Frank L, 2007 *Mater. Trans.*, **48** 940

[24] Aoyama T, Nagoshi M, Nagano H, Sato K, Tachibana S, 2011 *ISIJ Int.*, **51** 1487

[25] Erdman N, Robertson V, Shibata M, 2014 *Microsc. Microanal.*, **20(S3)** 20

[26] Rodenburg C, Rainforth W M, 2007 *Acta Mater.*, **55** 2443

[27] Rodenburg C, Viswanathan P, Jepson M A E, Liu X, Battaglia G, 2014 *Ultramicroscopy*, **139** 13

[28] Reimer L, 1993 *Image formation in low-voltage scanning electron microscopy,* Tutorial texts in optical engineering. Vol. TT 12 (SPIE Optical Engineering Press, Bellingham)

[29] Wells O C, Broers A, Bremer C, 1973 *Appl Phys Lett*, **23** 353

[30] Dapor M, 2014 *Transport of Energetic Electrons in Solids*, Springer. Tr. Mod. Phys., Vol. 257 (Springer, Berlin)

[31] Shen X B, Hu W G, Russell T P, 2016 *Macromolecules*, **49** 4501

[32] Dapor M, Bazzanella N, Toniutti L, Miotello A, Crivellari M, Gialanella S, 2013 *Surf. Interface Anal.*, **45** 677

[33] Plenderleith A R, Pateman C J, Rodenburg C, Haycock J W, Claeyssens F, Sammon C, Rimmer Stephen, 2015 *Soft Matter*, **11** 7567

[34] Master R C et al, 2015 Nat. Commun., **6** 6928

[35] Lesiak B, Jablonski A, Prussak Z, Mrozek P. 1989 *Surf. Sci.*, **223** 213

[36] Williams M R, Arakawa E T, 1972 *J. Appl. Phys.*, **43** 3460

[37] Dapor M, Galliari L, Garberoglio G, 2015 *Nucl. Instrum. Methods Phys. Res. B*, **352** 181

[38] Postek M T, Vladar A E, 2013 *Scanning*, **35** 355

[39] Poelking C, Daoculas K, Troisi A, Andrienko D, 2014 *P3HT Revisited - From Molecular Scale to Solar Cell Device Chapter 5 Morphology and Charge Transport in P3HT: A Theorist's Perspective*, Adv. Polym. Sci., vol. 265 (Springer, Heidelberg)

[40] Shen X, Hu W, Russell T P, 2016 *Macromolecules*, **49** 4501

Supporting information

1. The expression of the BSE signal detection based on spatial distribution

The effective BSE signal strength at a defined detection point is determined by two elements: the BSE angular distribution and the detection angle ϑ_D representing the location of detection point. The BSE angular distribution can be acquired from Monte Carlo simulation with the input of material information and primary beam energy, while the ϑ_D can be measured according to the microscope settings.

In real SEM observation a single detection point is not selectable, for a real detector the received signal is the sum of all electrons landed on the detector surface. Considering a defined detector segment of CBS detector, the detection surface is a ring perpendicular to the primary beam, the range of detection angle for this segment is from ϑ_{Dmin} to ϑ_{Dmax} (P2 figure SI 1.2). The sum of this effective detected BSE signal can be written as equation SI 1.1:

$$S_{E(BSE)} \propto \eta(E_{BSE} - E_T) \int_{\theta_{D\min}}^{\theta_{D\max}} [\cos^2 \theta_D * P_{BSE}(\theta_D)] d\theta_D \qquad \text{SI 1.1}$$

Thus since the BSE angular distribution $P_{BSE}(\theta)$ only depends on the primary electron beam and the E_T is a constant for defined detector, we can write the BSE signal intensity as a function the detection angle and the BSE signal intensity can be acquired based on the measured ϑ_D.

When a deceleration field is applied on the SEM sample, $\vartheta_D = \vartheta_S$ is no longer valid. So we need to estimate the effective signal strength based on ϑ_D, requiring a transformation of electron angular distribution from axis based on ϑ_S to one based on ϑ_D.

If the sample surface and the detector surface are flat and large enough, we assume the deceleration field is a uniform parallel electric field from sample surface to detector plane with strength E_d. According to the definition of electric field strength, we can write E_d into equation SI 1.2:

$$E_d = \frac{U_d}{h} \qquad \text{SI 1.2}$$

where h is the shortest distance from emission point to detector plane, which is equal to the measured working distance for a zero-thickness detector plane.

As mentioned in equation 2.1.4, S_E is a function of the electron scattering angle ϑ_S. However, ϑ_S is only equal to ϑ_D when there is no external electric field applied. Hence in order to represent S_E with controllable parameter which is the location of detection point, we need to replace ϑ_S with ϑ_D when a beam deceleration is used. If we define the emission point as (0,0) and sample surface as the *x* axis, the relationship between ϑ_S with ϑ_D can be seen in P2 figure SI 1.1 .
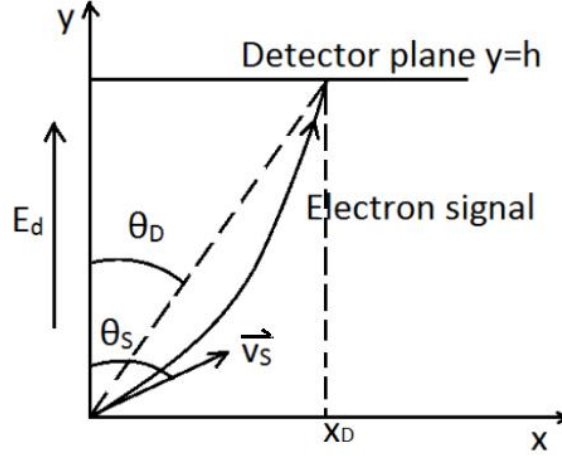
P2 figure SI 1.1: An electron scattered with speed v_S and scattering angle ϑ_S from emission point (0,0) traveling to detection point on detector plane y=h. A deceleration field E_d is applied from sample surface to detector plane.

We define the detection point as (X_D, h). X_D can be calculated from the electron scattering speed v_S and scattering angle θ_S:

$$v_s = (|v_s| \sin\theta_S,\ |v_s| \cos\theta_S)$$

The flight time of scattered electron is defined as T, the electron speed in the direction of the y-axis as v_{ey}. As the movement of scattered electron in the direction of the y-axis is a uniform accelerated movement we obtain:

$$h = \int_0^T v_{ey} dT$$

where,

$$V_{ey} = v_S \cos\theta_S + \frac{U_d}{h} \frac{q}{m} T \qquad \text{SI 1.3}$$

Note that v_{ey} will not exceed 15% of the speed of light in normal LVSEM situation. Hence, relativistic effects can be neglected leading to equation SI 1.4:

$$h = \int_0^T (v_S \cos\theta_S + \frac{U_d q T}{hm}) dT = v_S \cos\theta_S T + \frac{U_d q T^2}{2hm} \qquad \text{SI 1.4}$$

Considering the second solution for equation SI 1.4 will require a negative speed vector in x axis, only one solution has physical meaning, hence:

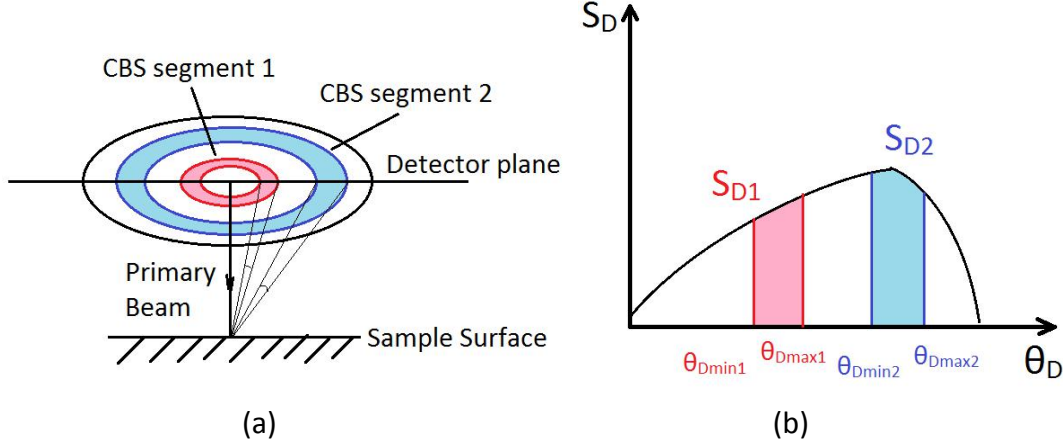$$T = (\sqrt{v_S^2 \cos^2\theta_S + \frac{2U_d q}{m}} - v_S \cos\theta_S) \frac{hm}{U_d q}$$

SI 1.5

q is the electric charge of one electron

m is the mass of one electron

According to P2 figure SI 1.1, we can write ϑ_D in the following form

78

$$\theta_D = \tan^{-1} \frac{v_s \sin\theta_s T}{h} \qquad\qquad \text{SI 1.6}$$

Since T is already written as a function of ϑ_S in the solution of equation SI 1.4, θ_D can also be written into the form of function of ϑ_S as equation 2.2.1.

(a)   (b)

P2 figure SI 1.2: The schematic of the range of detection angle ϑ_D determined by CBS detector segments (a) and the related S_{Dsum} acquired by integration from ϑ_{Dmin} to ϑ_{Dmax} (b).

2. The expression of the SE signal detection based on spatial/energy distribution

When no external electric field is applied in the SEM, the representation of SE detection is similar to the BSE despite all the SE is emitted with different electron energies. Thus the SE part of the energy-angular distribution in equation 2.1.2 cannot be easily simplified. In order to relate the energy-angular distribution acquired from MC simulation to the microscope detection intensity, we project it separately onto the energy-probability and angular-probability planes.

When selecting small electron energy ranges around a series of defined electron energy E_{SE1}, E_{SE2}, E_{SE3}, ... E_{SEn}, if those electron energy ranges are very small, we can assume the electron angular distribution in the energy range around E_{SEn} is equal to the angular distribution at $E_{SE}=E_{SEn}$. Thus we can acquire the total probability of SE landing on a defined angular range by the integration from ϑ_{Dmin} to ϑ_{Dmax} on the angular distribution curve for $E_{SE}=E_{SEn}$ (P2 figure SI 2.1). According to equation 2.1.2 and 2.1.4, the effective SE signal intensity $S_{E(SE)}$ can be written as equation:

$$S_{E(SE)} \propto \iint [\delta P_{SE} * \cos^2 \theta_D * (E_{SE} - E_T)] dE_{SE} d\theta_D \qquad\qquad \text{SI 2.1}$$

The calculation of the $S_{E(SE)}$ is based on the detection probability at $E_{SE}=E_{SEn}$, and plotted as a series of S_{DSE} from E_{SE1} to E_{SEn}. Then the integration of this plot is proportional to the total SE detection signal intensity.

| (a) | (b) |
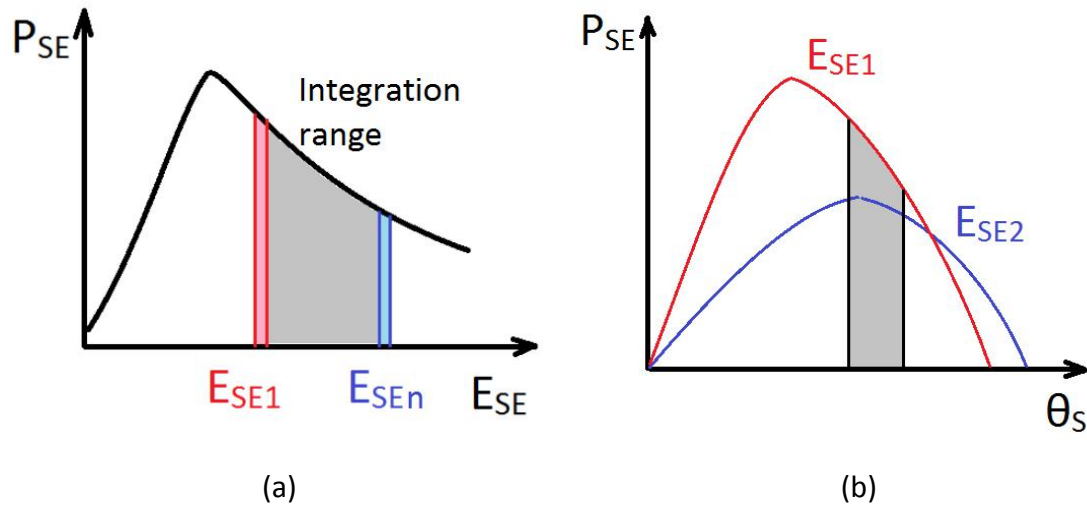
P2 figure SI 2.1: Schematic of the selection of electron energy range E_{SEn} on the SE energy distribution curve (a), and acquisition of SE detection probability on angular distribution curve when $E_{SE}=E_{SEn}$ (b), the grey area represents the detection angular range of the defined detector segment.

3. The Implantation depth profile and the thickness definition of bulk sample in BSE imaging

As mentioned in 3.2, the sample imaged is considered to be a bulk sample and electron transmission is not included in our calculation or imaging. In order to define the thickness limit for a bulk sample, using MC once again we simulated the BSE implantation profile in our chosen single element samples. The BSE implantation in our composite sample cannot be simulated due to the heterogeneous nature of the composite sample. But since the thickness is on the mm scale it can be considered "bulk" for low-voltage BSE imaging.

As shown in P2 figure SI 3.1 a, when E_0=2keV, the electron implantation curve in amorphous C yielded a peak at around 50nm, and the maximum implantation is around 164nm. This depth has largely exceeded the original C film, but it does not exceed the thickness of our C layer sample (with thickness over 4 μm) as shown in P2 figure SI 3.1 b. On the other hand, the maximum electron implantation depth in Cu is 66 nm, which is much smaller than the thickness of our Cu grid sample.

The validity of our BSE model will only apply when no major electron transmission has occurred such as our samples shown here.
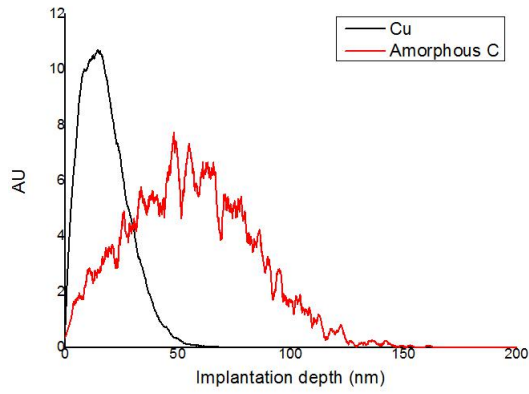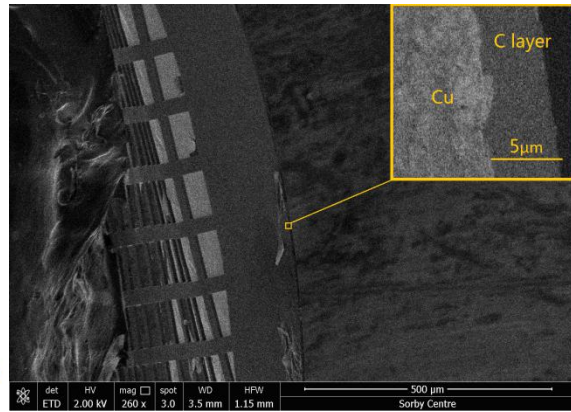
(a)   (b)

P2 figure SI 3.1: The BSE implantation profile of Cu and amorphous C sample when E_0=2keV (a) and the SEM image of our C layer created by coating on a TEM grid (b), the small box on the top right is an enlarged image sample edge

4.2 Mapping nanostructural variations in silk by secondary electron hyperspectral imaging

As shown in 4.1 the BSE technique can be optimized for compositional contrast between two given phases, however many bio-material systems (especially natural ones) are more complex. SE hyperspectral imaging technique exploits the SE energy spectra and specific energy windows can be found corresponding to each phase in a complex material system. Thus SE hyperspectral technique can identify the phases which BSE technique cannot and also push imaging to higher resolution. However, the SE spectra need to be collected on known phases to identify the SE peaks. Thus in the following manuscript the crystalline nano-fibril phase was located by BSE technique, and the hyperspectral SE technique was applied based on the SE spectra collected from nano-fibril and silk fiber matrix.

The paper attached below is published in 2017 Advanced materials, 1703510. This paper includes one manuscript with three figures, P3 figure 1-3 and one supporting information with 14 figures, P3 figure S1-S14. Statement of contribution and copyright is attached at the end of thesis.

Quan Wan, Kerry J. Abrams, Robert C. Masters, Abdullah C. S. Talari, Ihtesham U. Rehman, Frederik Claeyssens, Chris Holland and Cornelia Rodenburg*

Department of Materials Science and Engineering, University of Sheffield, Sir Robert Hadfield Building, Mappin Street, Sheffield, S1 3JD, UK

Keywords: Silk, SEM, Protein, Polymer, Imaging

Nanostructures underpin the excellent properties of silk. Although the bulk nanocomposition of silks has been well studied, direct evidence of the spatial variation of nanocrystalline (ordered) and amorphous (disordered) structures has remained elusive. Here we demonstrate that secondary electron hyperspectral imaging, can be exploited for direct imaging of hierarchical structures in carbon based materials which cannot be revealed by any other standard characterization methods. Applying this technique to silks from domesticated (*Bombyx mori*) and wild (*Antheraea mylitta*) silkworms, we report a variety of previously unseen features which highlight the local interplay between ordered and disordered structures. We conclude that our technique is able to differentiate composition on the nanoscale and enables in-depth studies into the relationship between morphology and performance of these complex biopolymer systems.

A polymer's macroscopic material properties depend on the local organisation of its nanostructures [1][2]. For silk, a key factor in this relationship appears to be the ability to modulate crystallinity, also referred to as the ordered fraction.[3] Whilst this ordered fraction has been measured in bulk through spectroscopy (Raman[4a-f], NMR[4g,h], CD[4i,j], SAXS[4k,l], SANS[4m,n], FTIR[4o-r]) and inferred via mechanical testing (tensile, DMTA)[4s-v], modelling suggests that the mechanical properties of silks are a rather complex interplay between ordered and disordered fractions at a local scale.[5] Whilst some studies have indicated spatial differences of these fractions, either through radiolabeling[6] or local modulus measurements[7], few, if any, techniques have been able to map this nanocompositional variation directly. This situation represents a current length-scale characterization and knowledge gap.

This work exploits secondary electron hyperspectral imaging (SEHI), a new scanning electron microscope (SEM) based characterization tool to reveal and visualize nanostructural variations across micron-scale spatial dimensions. We report that despite similarity in overall ordered fraction, there are distinct differences in the nanoscale order/disorder maps of natural silk fibers from both *Bombyx mori* and *Antheraea mylitta*.

The structural hierarchy of silkworm silks surrounds a sericin glue that binds two microscopic fibroin brins (~15 µm) [3] which are comprised of ~200 nm microfibers and nanofibrils [8] and, finally, nanoscale phases which can be ordered or disordered [4], as shown in the schematic diagram in **P3 figure 1a**.

Using low voltage standard SEM of a cryo-snapped and plasma exposed silk fibers of *B. mori* silk and *A. mylitta* silk it is possible to visualise bright nanostructures (**P3 figure 1a**) due to topographical contrast but such contrast is problematic for accurate nanoscale dimension measurements due a feature size and shape dependant edge effect [9] and, furthermore the topography can be caused by different mechanisms and it is therefore prone to artefacts introduced by sample preparation. Nevertheless, we observe that the average area fraction of these nanostructures is similar in both silks, in *A. mylitta* silk the round nanostructures seem smaller, denser and interconnected.
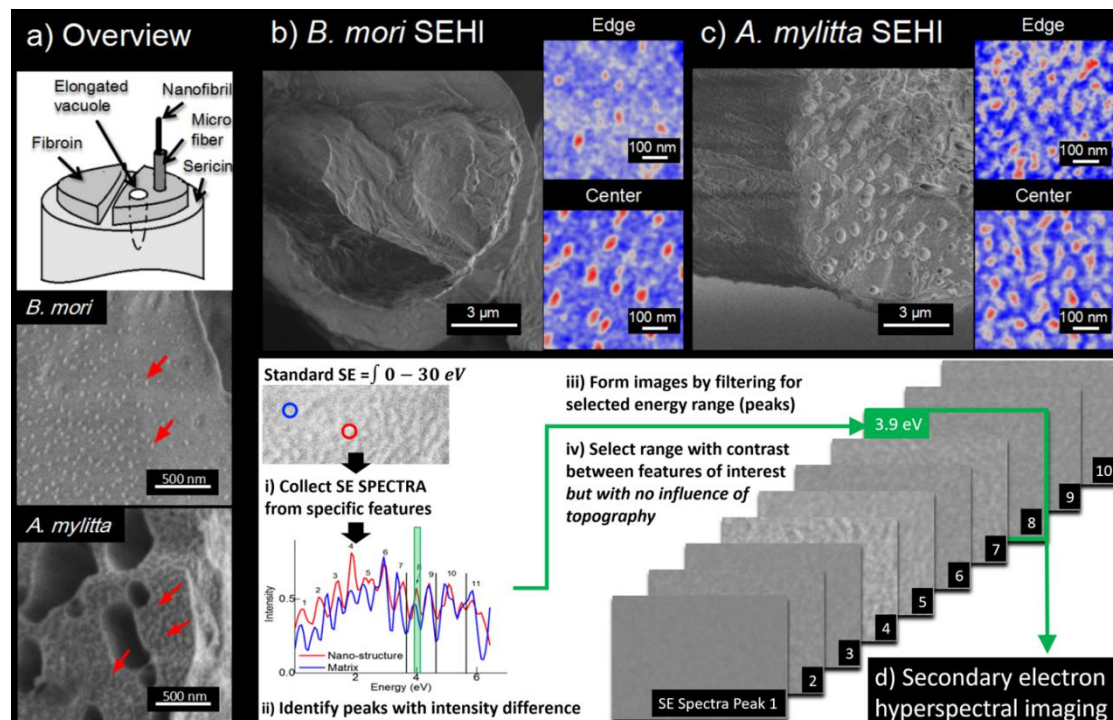
P3 figure 1. a) A schematic overview of a silkworm silk fiber and cross-sectional micrographs of *B. mori* and *A. mylitta* silk using low voltage SEM which identifies bright nanostructures on cryo-snapped, plasma-etched cross-sections as shown by red arrows. Here the nano-structures are visible due to topography contrast as they are slightly raised due to the preferential removal of the low order matrix during sample preparation. Using SEHI, topographical contrast can be supressed (SI section 3 & 6) and the bright features in a) are identified as the ordered fraction (SI section 3 & 5) and shown in fiber cross-sections for b) *B. mori* and c) *A. mylitta*. For better visualization of these structures, an enlarged view (500 nm×500 nm) at the ordered fraction energy peak along with color coded SE hyperspectral image collected using the energy window (3.9 ± 0.3) eV is shown taken from the edge and from the center for each species. Red is assigned to the ordered phase, Blue is the disordered phase and gray the oriented amorphous phase.   To concept of SEHI is summarized in the schematic in e), which displays the SE spectra from B. *mori* silk. The spectra for *A. mylitta* silk are shown in SI (**P3 Figure S3**) along with a full explanation of the terminology in SI, section 1. (The image array was remade by C. Holland and C. Rodenburg)

In order to determine the nature of these bright nanostructures and their dimensions we applied SEHI. SEHI exploits the distinctiveness of secondary electron (SE) signals in carbon based material[10] for hyperspectral imaging (HI) and has the advantage of being able to avoid the confounding influence of topology which beleaguers standard SEM (see SI section 6). The concept of HI is well established in vibrational spectroscopies[11a], where images are formed from several different energy regions, and based on distinctive peaks in the spectrum. This is demonstrated in the schematic in **P3 figure 1d**.   Here we collect SE spectra from the high density nanoscale regions, as established by comparison of Backscattered Electron (BSE) density maps [12] (SI, section 1), which we find correlate with the bright features in the standard SEM images in **P3 figure 1a**. This allows us to investigate which peaks in the SE spectra are related to high density (SI section 3), thus high order (SI section 1). We then   apply the HI concept to quantitatively map the different phases in silks by imaging with an energy window (3.9 ± 0.3) eV which was   specifically selected to map   high order regions   and is free from topographical artefacts (see SI for energy calibration (section 2), peak selection and validation (section 3)). To demonstrate the close relation of HI to vibrational spectroscopy, we performed SEHI on a semi-crystalline polymer system in conjunction with Raman microscopy to further confirm the validity and suitability of our technique for silks (SI, section 4).

Raman/IR[11a,b, c] and XRD[11d] studies show that at least two dominating phases[11e] exist in silk fibroin: a crystalline phase, mostly assembled as nanofibrillar β-sheet crystals which we term ordered, and an amorphous phase which we classify as disordered. A third, oriented amorphous phase has also been suggested based on Raman and XRD studies on spider silks[13a,b], and inferred for *B. mori* silk from the oriented chain composition in the matrix and in regenerated samples[13c,d].

To confirm the most appropriate energy window was used to discriminate the ordered phase, we first analyzed each of 11 observed peaks in the SE spectra (SI, **P3 Figure S3**)   in terms of peak position, and peak intensity differences between matrix and nanostructures to predict a suitable peak for imaging high (SI, **P3 Figure S4**), and then tested this prediction by SEHI images for each of the peaks present in the collected SE spectra (SI, **P3 Figure S5**). From the analysis of spectra only, we predicted the window at   (3.9 ± 0.3) eV is most suitable to image high order regions, which was confirmed by the SEHI image array shown in (SI, **P3 Figure S5**).

A phase map of the ordered fraction for these materials is presented in **P3 figure 2**. Here high intensity (white) corresponds to the ordered phase, mid-intensity (mid-gray levels) to the oriented amorphous phase and low intensity (black) to the disordered phase based on fitting Gaussian peaks to the strongly asymmetric histograms (**P3 figure 2**e,f) that can be best fitted by three peaks (please see full details for peak fitting and justification of phase allocation in SI, section 5). Note that this phase-contrast relationship is only valid for the 3.9eV SEHI image. In fact, we find that for SEHI using a window centred at 4.2 eV of the same area results in a reversal of contrast at most locations as shown in **P3 figure 3**. Hence, we attribute the 4.2 eV peak in the SE spectrum to the disordered phase (see SI, section 3 for full

justification).
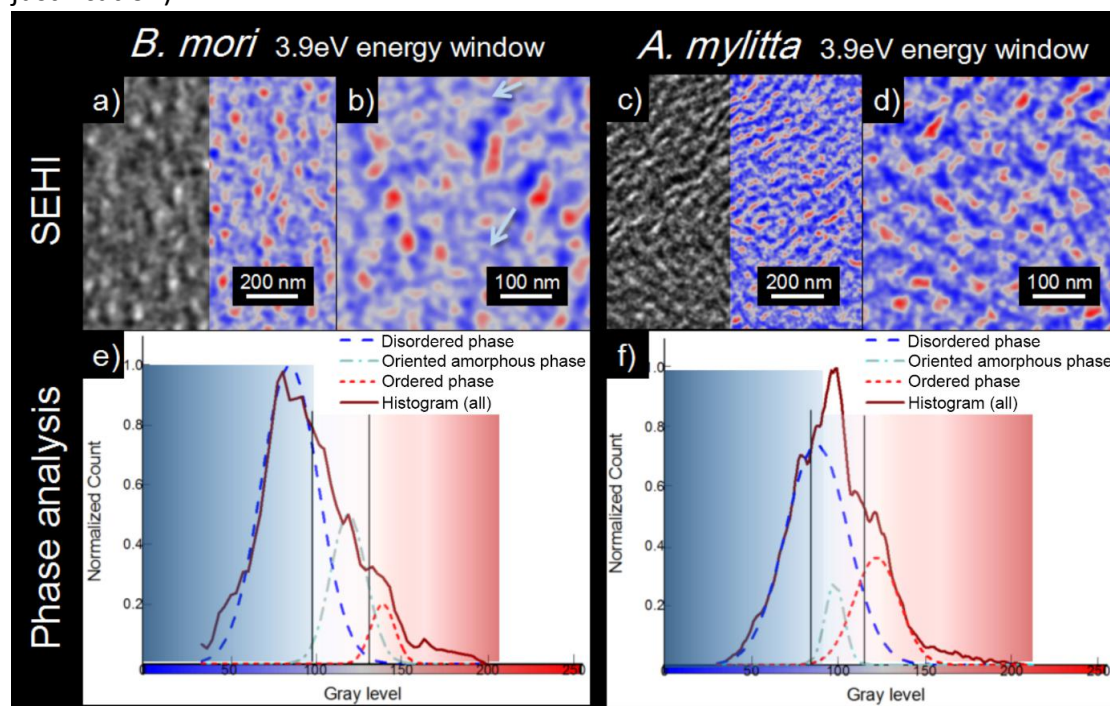
P3 figure 2. Half color coded SEHI image energy window (3.9 ± 0.3) eV for a) *B. mori* silk and c) *A. mylitta* silk cryo-snapped cross-section, with higher magnification and full color coding SEHI in b) and d). The (3.9 ± 0.3) eV energy window results in high intensity levels for the ordered phase (SI, sections 3 & 5). Therefore, in image a) to d), red represents the ordered phase, blue is the disordered phase and the gray represents the oriented amorphous phase. To assign these colors the histogram of the original gray scale SEHI image was analyzed in e) for *B. mori* silk and f) for *A. mylitta* silk with the peak of each phase calculated through Gaussian fitting to match the overall histogram (for full details of peak fitting see SI section 5).
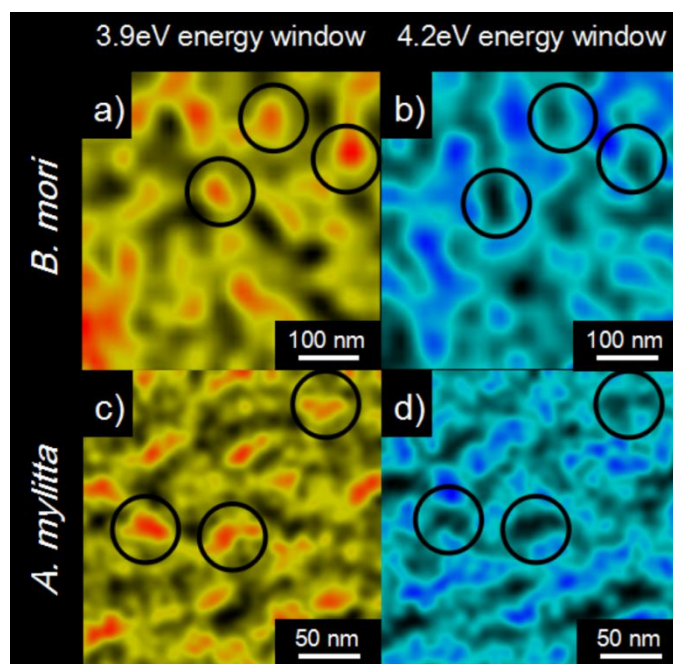
P3 figure 3. Color coded SEHI images collected from the (3.9 ± 0.3) eV ordered phase energy window a, c) are compared to the (4.2 ± 0.3) eV disordered phase energy window b, d) for *B. mori* and *A. mylitta* silk cross-section samples. Note the field of view for each species is the same for both images. The black circles represent areas where the intensity in the (3.9 ± 0.3) eV and (4.2 ± 0.3) eV windows are mutually exclusive, supporting our assignment of these windows to discriminate between ordered and disordered fractions.

To determine the bulk ordered fraction for *B. mori* silk and *A. mylitta* fibers we further analyzed the (3.9 ± 0.3) eV SEHI images as a whole (details in SI, section 5). By assuming that the silk proteins in the bright ordered phase adopt mostly β-sheet conformations and form nanoscale crystals, as suggested by literature [14], based on total area fraction for *B. mori* we estimate an overall fiber ordered content of ~10.4% which agrees well with ~10% crystallinity as measured by X-ray data[15]. For *A. mylitta* fibers, an ordered content of ~13.4% is estimated which is close to reports of ~14.7% β-sheet content   as determined by IR spectroscopy[11f].

Moving beyond bulk measurements, SEHI phase mapping reveals that the size and distribution of the ordered structures are not uniform across the silk fiber cross-section (**P3 figure 1**). The local ordered phase maps of *B. mori* (**P3 figure 1** b) shows that the diameter of these ordered structures is   larger near the edge   of the fiber in comparison to the size of the order structures found in the fiber center. The related full size distribution analysis across the whole cross-section is shown in SI (**P3 P3 Figure S11**c) and the SEHI data reveal a an increase from ~25 to 45 nm within the first 800 nm) for *B. mori* . Likewise, the area fraction reaches a maximum of 12% at the centre of the fiber see SI (**P3 P3 Figure S11**h). In contrast *A. mylitta*'s ordered fraction maps (**P3 figure 1**c) did not show any significant size change across the fiber, maintaining a diameter of 40 nm as shown in SI (**P3 P3 Figure S11** f), and an overall decrease of ordered structures towards the center of the fiber (see SI, Figure   S11h).

However, these distribution differences may be related to the presence of the large amount of small vacuoles close to the fiber edge for *A. mylitta* (SI, section 7).

The observed change in ordered fraction across the fiber in *B. mori* is consistent with a model proposed by TEM analysis of degummed *B. mori* silk, whereupon crystalline areas are reported to form cup-shaped banded regions along the longitudinal axis[15]. This is also reflected in the inclined nanopattern observed on the longitudinal section of *B. mori* silk (see **P3 P3 Figure S13**). Due to the absence of ordered structure size variation in our *A. mylitta* samples, we also infer the absence of cup-shaped banding, which is again confirmed by the relatively flat appearance of the areas between vacuoles in the longitudinal sections of *A. mylitta*. In summary, SEHI has revealed that despite having similar overall ordered phase fractions, these two species differ in both size and distribution of the ordered structures at the nanoscale.

Hence from our SEHI observations, we propose two main areas for hypothesis testing in the future. Firstly, the distribution of order/disorder may be related to the flow field encountered by the silk feedstock in the gland as it undergoes solidification, and, secondly, this distribution may be related to a fiber's mechanical properties and failure mechanism.

Taking each area in turn, during spinning and in *ex vivo* rheological testing, the flow field encountered by the silk proteins is largely responsible for the formation and stabilization of ordered structures, specifically β-sheets and larger nanofibrils[16]. From the data presented here *A. mylitta* adopts a more homogeneous size distribution of ordered features across the fiber, while *B. mori* ordered features are fewer and smaller at the fiber edge, we predict that the flow fields responsible for their generation are more evenly distributed in *A. mylitta* than in *B. mori*. This may be related to differences in gland morphology and the action of the silk press[17a,b], the effects of sericin[17c,d], or the feedstock's rheological properties facilitating a greater extensional flow in the middle of the silk duct of *B. mori*[17e-j].

Finally, silk fiber mechanical properties are known to be species dependent and often correlated to their bulk crystallinity content [18]. Our results for ordered bulk content align well with those of previous spectroscopy studies [11f, 14], therefore SEHI could support future structure-function work by probing how the ordered/disordered phases contribute towards a fiber's mechanical properties. For example, previous fractographic studies of typical polymer nanocomposites report that nanofibrous structures are generally tougher than the bulk component[19a-d] as has been proposed in modelling studies of silk [19e,f]. Hence this technique could be used to identify both the presence of and order/disorder content of silk nanofibrils[8]. However at a slightly larger lengthscale, it is known that microvoids (i.e. the elongated vacuoles) may prevent stress concentrations and subsequent crack propagation in silk[20] and as such there may be a complex dynamic between impinging structural hierarchies which remains to be elucidated.

In conclusion SEHI has provided a means to spectroscopically map silk's molecular order and disorder across several length scales, down to the nano. We propose this new tool could provide us with a means to visualize a silks feedstock's flow history or be used as a predictor of a fiber's mechanical properties. Thus we expect that this

innovative approach will prove fundamental to the understanding of silk formation an indeed, other hierarchical materials.

Experimental

Silk cocoons were obtained from animals bred in captivity and supplied by World Wide Butterflies Ltd and stored under lab conditions until use. Cocoons were unravelled onto spools. *A. mylitta* samples were first demineralised by immersion for 48 hours in 10M ethylene diamine tetra acetic acid (EDTA), gently stirred at 40 °C and unravelled at 20 mm.s^{-1} in deionised water alongside *B. mori* cocoons (which do not require demineralisation).

Subsequently, silk fibers were cut into 5 cm sections using a scalpel blade, and both ends were attached to a clean 1 cm x 3 cm silicon wafer by conductive carbon tape. The fixed fibers were soaked in deionised water and sandwiched between another silicon wafer before cryo-fracturing in liquid nitrogen. The "snapped" cross-section samples were left to dry in air at room temperature for over 2 hours and then briefly plasma etched in a Diener Zepto version B plasma cleaner at 50% power of 100W for 40s. This treatment also enhances crystalline features and conductivity at the surface which allows for better imaging[21]. The silk samples were not coated by a conductive coating before analysis, artefact created by plasma and electron beam damage is discussed and excluded in SI, section 8.

According to the literature[22], the SE spectra of many inorganic materials reflect the status/composition of material within the range of 0- 12eV SE energy. For silkworm silks, the spectra are collected with a similar method described in previously published work[23] utilizing deflection voltages 0 V to 30 V in the through lens detector (TLD) in a Nova 450 nano SEM, the detail of the filter mechanism in this detector is described in literature[23]. The SE hyperspectral images are collected by an iFast auto collection recipe for both SEMs (Nova 450 for silk and Helios for PP), the image processing, and related SE spectra collection/peak selection is described in the previous paragraph and SI section 2 and 3, respectively. The 0-11 eV range was collected for the two silk species with an electron energy step size of 0.071eV. The intensity data was averaged from several (2 x 2)μm^2 area on three different fibroin samples.

After identification of peaks in the SE spectra, the start and end of each peak was defined. The midpoint is defined as where the differentiated spectra reached zero. High resolution SE images were taken at those equivalent deflection voltages and processed by subtracting the peak-end image from the peak-start image. The SEM image was contrast enhanced and normalized with software ImageJ v1.48, the original image for SEHI is shown in detail in **P3 Figure S8**.

Supporting Information

Supporting Information is available from the Wiley Online Library or from the author. Supporting information accompanying this manuscript content is listed below:
1. Evidence of nano-scale density (order/disorder) variations by imaging with

Back-Scatter Electrons (BSE)

2. Secondary electron (SE) spectrum collection and energy calibration

3. Establishing the link between peaks in SE spectrum and order, excluding effects of topology

4. Further Validation of SEHI for mapping of nanoscale order in semi-crystalline polymers by comparison to Raman microscopy on the example of microporous polypropylene sample

5. Establishing number of phases present in silks by SEHI and quantification of relative phase fractions

6. Measurement of dimensions of phases based on SEHI topography free images

7. Elongated tubular vacuole and microscale related features in silk fiber longitudinal section

8. Excluding Beam damage and plasma etching artefact

References

[1] a) W. Zeng, L. Shu, Q. Li, S. Chen, F. Wang, X. M. Tao, *Adv. Mater.* **2014**, *26*, 5310; b) I. Zlotnikov, E. Zolotoyabko, P. Fratzl, Prog. *Mater. Sci.* **2017**, *87*, 292

[2] a) M. J. Buehler, M. J. Cranford, *Nanotechnol. Sci. Appl.* **2010**, *3*, 127 b) P. Fratzi, In: Reis R.L., Weiner S. (eds) Learning from Nature How to Design New Implantable Biomaterialsis: From Biomineralization Fundamentals to Biomimetic Materials and Processing Routes. NATO Science Series II: Mathematics, Physics and Chemistry, vol 171. Springer, Dordrecht, **2014**, pp 15-34

[3] a) Z. Shao, F. Vollrath, *Nature* **2002**, *418*, 741 b) G. Zhou, Z. Shao, D. P. Knight, J. Yan, X. Chen, *Adv. Mater.* **2008**, *21*, 366 c) N. V. Bhat, G. S. J. Nadiger, *Appl. Polym. Sci.* **1980**, *25*, 921-932 d) Y. Shen, M. A. Johnson, D. C. Martin, *Macromol.* **1998**, *31*, 8857 e) R. Gebhardt, C. Vendrely, M. Burghammer, C. Riekel, *Langmuir* **2009**, *25*, 6307 f) Holland, C. Porter, D. Vollrath, F. *MRS Bulletin* **2013**, *38*, 73 g) Koeppel, A. Holland, C.

ACS Biomat. Sci. Eng. **2017**, *3*, 226

[4] a) P. Monti, P. Taddei, G. Freddi, T. Asakura, M. Tsukada, *J. Raman Spectrosc.* **2001**, *32*, 103 b) H. G. M. Edwards, D.W. Farwell, *J. Raman Spectrosc.* **1995**. *26***,** 901 c) P. Monti, G.   Freddi, A. Bertoluzza, N. Kasai, M. Tsukada, *J. Raman Spectrosc.* **1998**, *29*, 297 d) Z. Shao, R. J. Young, F. Vollrath, *Int. J. Biol. Macromol.* **1999**, *24*, 295 e) J. Sirichaisit, V. L. Brookes, R. J. Young, F. Vollrath, *Biomacromolecules* **2003**, *4*, 387 f) T. Lefevre, M. Rousseau, M. Pezolet, *Biophys. J.* **2007**, *92*, 2885 g) J. B. Addison, N. N. Ashton, W. S. Weber, R. J. Stewart, G. P. Holland, J. L. Yarger, *Biomacromolecules* **2013**, *14*, 1140 h) T. Asakura, Y. Suzuki, Y. Nakazawa, G. P. Holland, J. L. Yarger, *Soft Matter* **2013**, *9*, 11440 i) J. M. Kenney, D. P. Knight, C. Dicko, F. Vollrath, *Proceedings of the 19th European Colloquium of Arachnology*. **2000**. Aarhus, Denmark: Aarhus University Press j) C. Dicko, D. Knight, J. M. Kenney, F. Vollrath,   *Biomacromolecules* **2004**, *5*, 758 k) A. Martel, M. Burghammer, R. J. Davies, E. D. Cola, C. Vendrely, C. Riekel, *J. Am. Chem. Soc.* **2008**, *130*, 17070 l) C. Riekel, F. Vollrath, *Int. J. Biol. Macromol.* **2001**, *29*, 203 m) D. Sapede, T. Seydel, V. T. Forsyth, M. M. Koza, R. Schweins, F. Vollrath, C. Riekel, *Macromol.* **2005**, *38*, 8447 n) I. Greving, C. Dicko, A. Terry, P. Callow, F. Vollrath, *Soft Matter* **2010**, *6*, 4389 o) M. Boulet-Audet, F. Vollrath, C. Holland, *J. Exp. Biol.* **2015**, *218*, 3138 p) U. Slotta, M. Tammer, F. Kremer, P. Koelsch, T. Scheibel, *Supramol. Chem.* **2006**, *18*, 465 q) S. Ling,   Z. Qi, D. P. Knight, Z. Shao, X. Chen, *Polym. Chem.* **2013**, *4*,. 5401 r) G. Fang, S. Sapru, S. Behera, J. Yao, Z. Shao, S. C. Kundu, X. Chen, *J. Mater. Chem. B* **2016**, *4*, 4337 s) J. Guan, D. Porter, F. Vollrath, *Polymer* **2012**, *53*, 2717 t) J. Guan, D. Porter, F. Vollrath, *Biomacromolecule*, **2013**, *14*, 930 u) B. Mortimer, J. Guan, C. Holland, D. Porter, F. Vollrath, *Acta Biomaterialia* **2015**, *11*, 247 v) J. Guan, Y. Wang, B. Mortimer, C. Holland, Z. Shao, D. Porter, F. Vollrath, *Soft Matter* **2016**, *12*, 5926

[5] a) D. Porter, F. Vollrath, *Nanotoday* **2007**, *2*, 6 b) D. Porter D, F. Vollrath, *Soft Matter*,**2008**, *4*, 328 c) D. Porter, F. Vollrath, *Adv. Mater*. **2009**, *21*, 487 d) D. Porter, F. Vollrath, *Polymer* **2009**, *50*, 5623 e) D. Porter, F. Vollrath, *Biochim Biophys Acta-Proteins & Proteomics* **2012**, *1824*, 785 f) F. Libonati, M. J. Buehler, *Adv. Eng. Mater.* **2017**, http://dx.doi.org/10.1002/adem.201600787

[6] A. Sponner, E. Unger, F. Grosse, K. Weisshart, *Nat. Mater.* **2005**, *4*, 772

[7] a) S. R. Koebley, F. Vollrath, H. C. Schniepp, *Mater. Horiz*. **2017**, http://dx.doi.org/10.1039/c6mh00473c b) C. P. Brown, J. Macloed, H. Amenitsch, F. Cacho-Nerin, H. S. Gill, A. J. Price, *Nanoscale* **2011**, *3*, 3805

[8] a) Lin, T-Y, Masunga, H, Sato, R. Malay, A.D. Toyooka, K. Takaaki, H. Numata, K. *Biomacromolecules* **2017**, *18*, 1350 b) Miller, L.D. Putthanarat, S. Eby, R.K. Adams, W.W. *Int. J. Biol. Macromol.* **1999**, *24*, 159 c) Putthanarat, S. Stribeck, N. Fossey, S.A. Eby, R.K. Adams, W.W. *Polymer,* **2001**, *41*, 7735 d) Zhang, F. Lu, Q. Ming, J. Dou, H. Liu, Z. Zuo, B. Qin, M. Li, F. Kaplan, D.L. Zhang, X. J. Mater. Chem. B. **2014**, *2*, 3879 e) Ling, S. Li, C. Jin, K. Kaplan, D.L. Buehler, M.J. *Advanced Materials*, **2016**, *28*, 7783 f) Ling, S. Jin, K. Kaplan, D.L. Buehler, M.J. *Nano Letters*, **2016**, *16*, 3795

[9] Y.G. Li, P. Zhang, and Z. J. Ding. *Scanning* **2013**, 35(2), 127

[10] R. C. Master, A. J. Pearson, T. S. Glen, F. C. Sasam, L. Li, M. Dapor, A. M. Donald, D. G. Lidzey, C. Rodenburg, *Nat. Commun.* **2015**, *6*, 6928

[11] a) N. Qin, S. Zhang, J. Jiang, S. G. Corder, Z. Qian, Z. Zhou, W. Lee, K. Liu, X. Wang, X. Li, Z. Shi, Y. Mao, H. A. Bechtel, M. C. Martin, X. Xia, B. Marelli, D. L. Kaplan, F. G. Omenetto, M. Liu, T. H. Tao, *Nat. Commun.* **2016**, *7*, 13079 b) M. Boulet-Audet, F. Vollrath, C. Holland, *J. Exp. Biol.* **2015**, *218*, 3138 c) P. Monti, P. Taddei, G. Freddi, T. Asakura, M. Tsukada, *J. Raman Spectrosc.* **2001**, *32*, 103 d) C. Riekel, F. Vollrath, *Int. J. Biol. Macromoecules.* **2001**, *29*, 203 e) D. Porter, F. Vollrath, *Adv. Mater.* **2009**, *21*, 487 f) Fang, G. Sapru, S. Behera, S. Yao, J. Shao, Z. Kundu, S. Chen, X, *J. Mater. Chem. B.* **2016**, *4*, 4337

[12] Q. Wan, R. C. Masters, D. Lidzey, K. J. Abrams, M. Dapor, R. A. Plenderleith, S. Rimmer, F. Claeyssens, C. Rodenburg, *Ultramicroscopy* **2016**, *171*, 126

[13]] a) Z. Shao, F. Vollrath, J. Sirichaisit, R. J. Young, *Polymer* **1999**, *40*, 2493 b) D.T. Grubb, G.D. Ji, *Int. J. Biol. Macromol.* **1999**, *24*, 203 c) T. Lefevre, M. E. Rousseau, M. Pezolet, *Biophys. J.* **2007**, *92*, 2885 d) Y. Kawahara, A. Nakayama, N. Matsumura, T. Yoshioka, M. J. Tsuji, *Appl. Polym. Sci.* **2008**, *107*, 3681

[14] a) S-J He, R. Valluzzi, S. P. Gido, *Macromolecules* **1999**, *24*, 187 b) M. Boulet-Audet, F. Vollrath, C. Holland, *J. Exp. Biol.* **2015**, *218*, 3138 c) D. Sapede, T. Seydel, V. T. Forsyth, M. M. Koza, R. Schweins, F. Vollrath, C. Riekel, *Macromol.* **2005**, *38*, 8447

[15] Y. Shen, M. A. Johnson, D. C. Martin, *Macromolecules* **1998**, *31*, 8857

[16] a) D. N. Breslauer, L. P. Lee, S. J. Muller, *Biomacromolecules* **2009**, *10*, 49-57 b) M. Boulet-Audet, F. Vollrath, C. Holland, *Phys. Chem. Chem. Phys.* **2011**, *13*, 3979 c) M. Boulet-Audet, A. E. Terry, F. Vollrath, C. Holland, *Acta Biomater.* **2014**, *10*, 776 d) C. Riekel, M. Mueller, F. Vollrath, *Macromolecules* **1999**, *32*, 4464 e) C. Holland, J. Urbach, D. Blair, *Soft Matter*, **2013**, *8*, 2590

[17] a) T. Asakura, K. Umemura, Y. Nakazawa, H. Hirose, J. Higham, D. Knight, *Biomacromolecules* **2007**, *8*, 175 b) T. Asakura, J. Yao, M. Yang, Z. Zhu, *Polymer* **2007**, *48*, 2064 c) K.H. Lee, *Macromol. Rapid Comm.* **2004**, *25*, 1792 d) C. S. Ki, I. C. Um, Y. H. Park, *Polymer* **2009**, *50*, 4618 e) M. Moriya, K. Ohgo, Y. Masubuchi, T. Asakura, *Polymer* **2008**, *49*, 952 f) M. Moriya, F. Reschzttadtz, Y. Nakahara, H. Saito, Y. Masubuchi, T. Asakura, *Biomacromolecules* **2009** *10*, 929 g) D. N. Breslauer, L. P. Lee, S. J. Muller, *Biomacromolecules* **2009**, *10*, 49 h) C. Holland, D. Porter, F. Vollrath, *Biopolymers* **2012**, *97*, 362 i) K. Tanaka, S. Mizuno, *Isect Biochem. Molec.* **2001**, *31*,. 665 j) Y. Liu, Z. Shao, F. Vollrath, *Nat. Mater.* **2005**, *4*, 901

[18] a) S. Keten, Z. Xu, B. Ihle, M. J. Buehler, *Nat. Mater.* **2010**, *9*, 359 b) A. Nova, S. Keten, N. M. Pugno,i A. Redaell, M. J. Buehler, *Nano Lett.* **2010**, *10*, 2626

[19] a) G. H. Michler, H-H. K-B. Von Schmeling, *Polymer* **2013**, *54*, 3131 b) Z. Huang, Y. Zhang, A. Motak, S. Ramakrishna, *Compos. Sci. Technol.* **2003**, *63*, 2223 c) J. Sandler, P. Werner, M. S. Shaffer, V. Demchuk, V. Altstadt, A. H. Windle, *Compos. Part A Appl. Sci. Manuf.* **2002**, *33*, 1033 d) K. Lozano, E. V. Barrera, *J. Appl. Polym. Sci.* **2001**, *79*, 125 e) S.W. Cranford, *J. R. Soc. Interface* **2013**, *10*, DOI: 10.1098/rsif.2013.0148 f) S. Isabelle, J. B. Markus, *Nanotechnology* **2016**, *27*, 302001

[20] R. M. Robson, *Int. J. Biol. Macromol.* **1999**, *24*, 145

[21] M. Kitagawa, T. Kitayama, *J. Mater. Sci.* **1997**, *32*, 2005

[22] D. C. Joy, M. S. Prasad, H. M. Meyer III, *J. Microsc.* **2004**, *215*, 77

[23] C. Rodenburg, M.A.E. Jepson, E.G.T. Bosch, M. Dapor, *Ultramicroscopy* **2010**, *110*, 1185

Supporting Information

0.   Overview

Here we describe several different avenues to ensure the validity of our data with regards to order/disorder.   First and foremost, it is vital to select a suitable SE energy range to map order /disorder only, which is done by direct comparison to low voltage BSE imaging (section 1). A well calibrated energy axis (section 2) is important too, as the materials exhibit a very large number of sharp peaks in close proximity. We inspect each of the peaks in terms for suitability to map order/disorder (section 3) and check for reproducibility of these peak positions and peak intensities (section 3). We identify a synthetic semi-crystalline system (section 4) that has order/disorder variations on both, length-scales accessible by Raman microscopy (tens of micrometers), but also on the nanoscale (25nm) and we used the SEHI to show order/disorder variations through the length scales on this system.   Next we explain how to proceed from a gray level SEHI to an order/disorder map (section 5).   To proceed from order/disorder maps to a feature sizes we interrogate line profiles from standard SEM (known to be dominated by topography) and the order/disorder maps and find further evidence that order/disorder maps do not reflect topography (section 6).   To obtain the correct area fractions for each phase for the *A. mylitta* samples the presence of vacuole, and the change in area taken up by the latter, has to be taken into account (section 7). Finally, we show that none of the features we described in the main article are artefacts generated either as result of electron beam or plasma exposure (section 8).

1.   Evidence of nano-scale density (order/disorder) variations by imaging with Back-Scatter Electrons (BSE)

The measurement of β-sheet crystallite sizes in longitudinal electron transparent sections obtained form a *B. mori* fiber by low voltage transmission electron microscopy exploiting density differences was previously reported, based on a *B. mori* silk fibroin densities of 1.35 g cm^{-3} in semi-crystalline films and 1.30 g cm^{-3} amorphous *B. mori* silk films[1]. A link between such sizes and the location of the section within the fiber diameter was not established.

The entirety of a fiber cross section becomes accessible through cryo-fracture as shown in **P3 figure 1** in the main article. However, as such fiber surfaces are not electron transparent, instead of low voltage transmission electron microscopy we employ **low voltage scanning electron microscopy low voltage (SEM)**. The SEM is equipped with several detector options that allow the collection of images using different signals:

Standard Secondary Electron (**SE**) images (used in Fig 1a main article) that mostly reflect the sample **topography** and are formed from all SE emitted from a sample surface; in this work Secondary Electron Hyperspectral Imaging (**SEHI**) series, where

each image is taken only from SE of a specific energy range, and finally Backscattered electron electron (**BSE**) images, that can be used to show topography or **density**, depending on imaging conditions.

It was shown that low voltage BSE images can reveal nanoscale density variations, for small density differences, as caused by ordered and disordered (amorphous) regions in semi-crystalline polymers but only if a specific combination of primary beam voltage, beam deceleration voltage and the signal collection angle, which is predicted by modelling,[2] is used for the BSE image collection. Therefore, we have modelled the BSE emission following the published procedure[2] with the input parameters provided in **P3 Table S1**.

P3 Table S1. Input parameters for BSE signal simulation

	Fibroin crystalline*	Fibroin matrix*
Unit composition§[3]	$C_{5.682}H_{12.567}N_{2.003}O_{4.339}$	$C_{4.2}H_{8.44}N_{1.24}O_{2.75}S_{0.004}$
Unit molecular mass	160.861	120.328
Density (g/cm^3)	1.35	1.3

*The crystalline fibroin here refers to the crystalline β-sheet section of the fibroin chains, not the experimental crystalline structures as the crystallinity of the structures varies in different fibers.

§The unit composition is calculated from the amino acid sequence of *B.mori* fibroin chains, we considered each Gly-X amino acid pair as a unit block of whole chain section. Composition here are averaged data of whole crystalline/matrix section.

The results of these calculations are presented in **P3 Figure S1** a) and demonstrate that the crystalline (ordered), and therefore denser material leads to the emission of a larger number of BSE compared to the less dense amorphous (disordered) material in a certain angular range only.
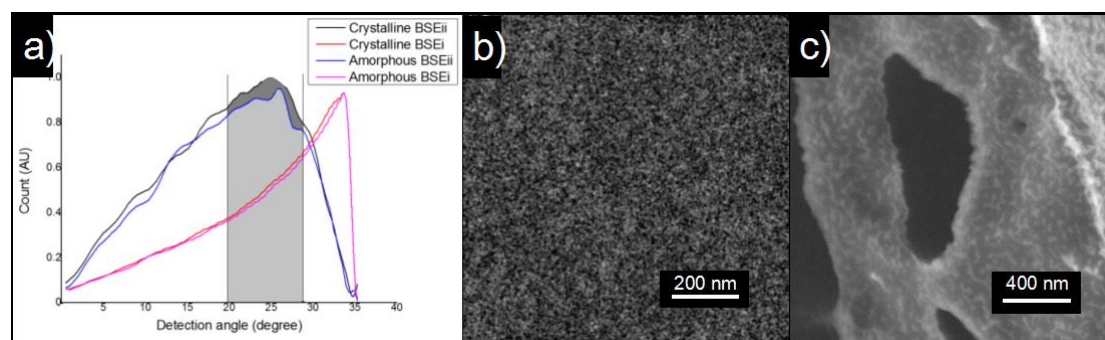
P3 Figure S1. The angular distribution of BSE signal on the detector plane for crystalline and amorphous fiber protein at 1 keV primary energy, 5 mm working distance and 4000 V deceleration voltage, the shaded area represents our selected experimental angle range. The BSE images collected in this range will provide a high degree of compositional (density) contrast. The image of *B. mori* silk cross-section b) and *A. mylitta* silk cross-section c) is collected in this range.

P3 Figure S1 b) and c) are the experimental BSE images taken from cross-sections using a 1 keV primary energy, 5 mm working distance and 4000 V deceleration voltage, which ensures detection of BSE in the angular range indicated in **P3 Figure S1** a). Therefore, we can establish with confidence that the brighter appearing

regions in the experimental BSE images in **P3 Figure S1** b**)**, c**)** reflect a local higher density and hence the location of more ordered material. It can be seen immediately from **P3 Figure S1** c), that the **well defined nano**structures appear bright and therefore represent the ordered phase, whereas the dark appearance of the matrix is indicative of its disorder and low**er** density. However, both signal to noise ratio and resolution in these BSE images are insufficient for any quantitative phase analysis as can be seen from **P3 Figure S1**b) which taken at higher magnification than S1 c).

2. Secondary electron (SE) spectrum collection and energy calibration

It was shown previously that both, phase contrast and resolution, of SE images can be obtained by selecting specific energy windows[4] for imaging.   SEHI allows the collection of SE spectra of the ordered nanostructures and matrix separately, as spectra could be derived for each location in an image from a series of images, were each of the images are formed by SE of a different energy range.   The practical implementation of SEHI can differ depending on the specifics of the detector design but the calibration of the energy scale is required and was conducted with the following procedure for any spectra used in the preparation of the main article.

SE spectra of a Cu grid at a range of stage bias values from -5 V to +5 V in 1 V steps were collected. The stage bias is a controllable parameter that can directly change the electron energy. If the stage bias is negative, the electron will be accelerated. The experimental results are shown in **P3 Figure S2** and show a linear relationship between microscope deflector bias and the change in energy cut-off and a conversion factor between deflector bias and SE energy is 2.84.
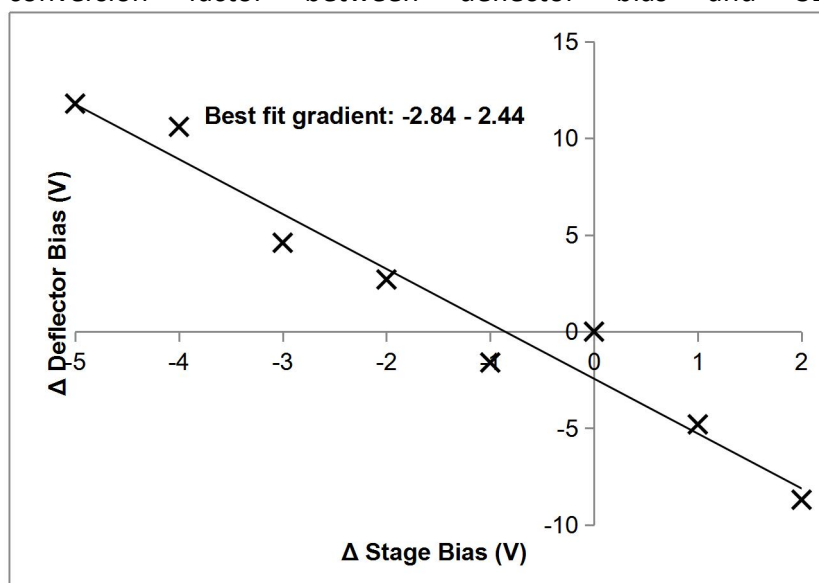

P3 Figure S2. The calibration for relationship between microscope parameter (deflector bias) and electron energy shift of the through lens detector in FEI Nova 450 SEM. (This plot is provided by R. Masters)

In order to carry out SEHI, a series of images series is collected from the same area, in which the change in cut-off energy from image to image is chosen. This allows SEHI images for a very narrow energy range to be obtained by subtracting two subsequent images in the image series.

3. Establishing the link between peaks in SE spectrum and order, excluding effects

of topology

As the link between density (hence order) is accepted in the context of BSE and we established from BSE images that nanostructures must be overall more ordered than the matrix (section 1), we can now compare the differences between the SE peaks found in the nanostructures and in the matrix, respectively, to establish if there is a link to order/disorder for any particular SE peak. SE spectra collected from the matrix and nanostructures in *A. mylitta* a) and *B. mori* b) silk fiber cross-sections are shown in **P3 Figure S3** a) and b) respectively, contain a large number (more than 11) of narrow sharp peaks.
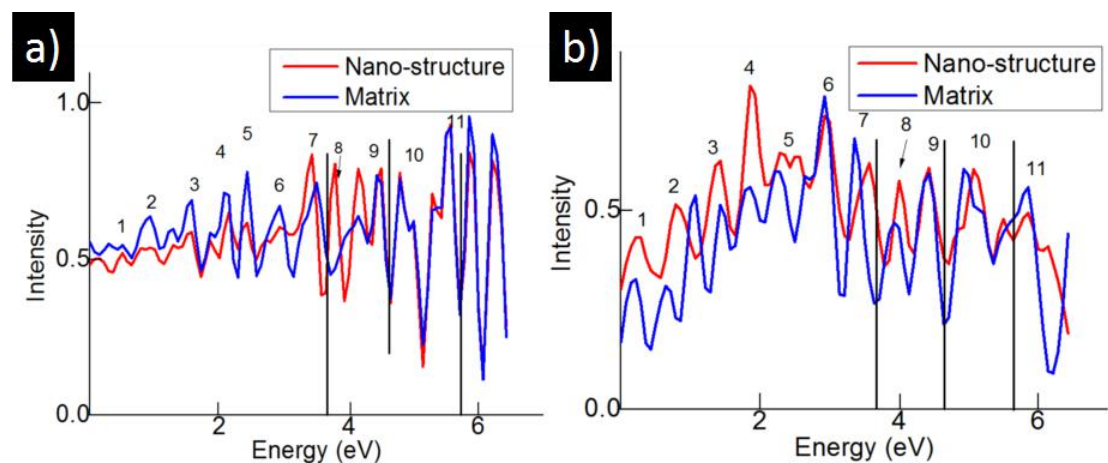
P3 Figure S3. The SE spectra of *A. mylitta* a), *B. mori* b) silk fiber

As with all spectroscopy we have to consider two parameters: (1) peak position and (2) peak intensity. From BSE imaging (section S1) we know that the nanostructures have higher density, hence higher order than the matrix. Therefore, we derived spectra for the nanostructures and matrix to establish which of the 11 peaks differ in matrix and nanostructures, either in position and/or intensity. We make this comparison for *A. mylitta* (**P3 Figure S3** a) and (*B. mori* **P3 Figure S3** b) on example spectra and have summarised the peak positions in **P3 Table S2**.

P3 Table S2. The average peak position of peaks

| Peak	1	2	3	4	5	6	7	8	9	10	11
Energy (eV)	0.4	0.9	1.7	2	2.6	3	3.3	3.9	4.2	4.8	5.6

In order to reduce the complexity of information but still demonstrate reproducibility, we have included **P3 Figure S4**. In **P3 Figure S4** a) we inspect each peak for consistency in peak position by plotting the deviation from the average peak position for each peak. The gap between the dashed lines at ±0.3eV represents the window widths of the energy window for imaging. Based on peak position alone peaks 1, 2, 5, 6, 7, 8, and 9 appear to consistent enough for imaging. In **P3 Figure S4** b) we consider peak intensity. There, are two conditions in relation to peak intensity to enable the mapping of high order nanostructures in a low order matrix:

(1) Consistency between intensity from nanostructures (established to be high order by BSE) relative to the peak intensity difference to the low order matrix.

If there is no difference, the peak might not be sensitive to order, or must be caused by a low density (disordered) fraction present in the nanostructure.

(2) The peak intensity for nanostructures itself, as well as the difference to the matrix, should be as high as possible in order to minimize the dose required for imaging.

From the data in **P3 Figure S4** it is apparent that only peak 1 and 8 fulfil peak position requirements as well as the intensity requirement (1). Peak 8 is the most suitable peak for mapping high order due to condition (2).
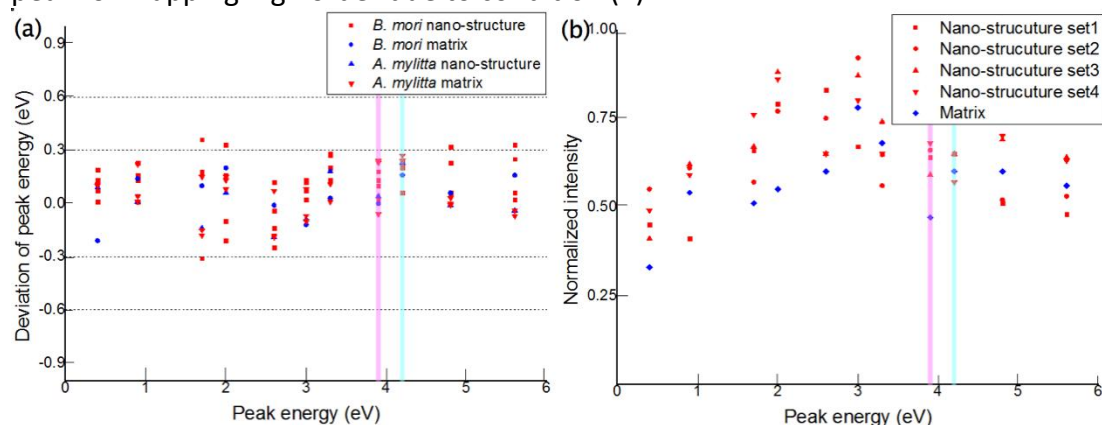
P3 Figure S4. Deviation of peak positions from average peak position for peaks 1-11 a) and intensity of peak in nanostructure and matrix respectively *B. mori*. b). The vertical lines indicate position of peak 8 (pink) and peak 9 (turquoise).

However, peak 9 (4.2 eV) is also of interest as the most consistent when considering both peak position and peak intensity. As there is no clear difference between the peak intensities from the matrix and the nanostructure, this peak is either not sensitive to order, or could be caused by a low density (disordered) fraction present in the nanostructure or a higher order component in the matrix. All this information was derived from spectroscopic information we now test if this is consistent with the images obtained from different peaks. To do this we have included **P3 Figure S5**.
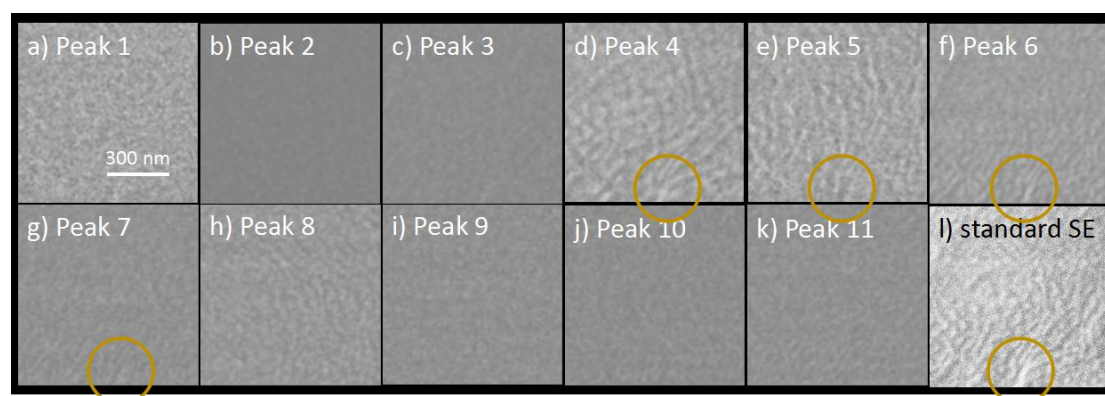
P3 Figure S5. The image array in a)-k) is collected from SE peaks (see **P3 Table S2** for peak energies) obtained from an *A. mylitta* cross-section sample. The image brightness was adjusted for better reproduction. The brightness in the original image is determined by the intensity in a particular peak, which varies substantially between different peaks and is much larger in the standard SE image (l), as the latter is formed from the signal emitted over the entire SE spectrum, yellow circle highlights topographical feature.

Note that all the images in **P3 Figure S5** were collected from exactly the same area, with the same electron dose (see details for dose in section 8) and contrast & brightness settings on the microscope, however we had to adjust the brightness in **P3 Figure S5** for reproduction purposes, as the maximum brightness of each image is dictated by the intensity in the respective peak, which varies between the different peaks and is substantially higher for the standard SE image.

The SEHI with the highest contrast are those taken from peak 4, 5 and 8.   However peak 4 and 5 contain a substantial contribution from topography contrast, while we can confirm that peak 8 is free from topography. Note, we identify the topographical feature as it appears in standard SEM (marked by yellow circle in **P3 Figure S5**) which is known to be dominated by topography contrast due to the edge effect (see more in section 6).

As predicted from spectroscopy peak 1 also has contrast of the same nature as peak 8 (bright nanostructures) as predicted from the analysis of the SE spectra, although this is quite difficult to see due to the much higher noise level in the image taken from peak 1. The latter was also predicted from the SE spectra analysis. Hence peak 8 (3.9 eV) remains the most suitable for imaging.

We further find contrast reversal between the images taken using the 3.9eV peak and 4.2eV peak. This is even more clearly shown in **P3 figure 3** in the main article. Again this is consistent with the prediction from spectroscopy that the 4.2eV peak is related to an overall lower order. **In summary both SE spectra and SEHI images consistently lead to the following conclusion:**

(1) high order can be imaged with the 3.9eV peak, low order with the 4.2eV peak as further demonstrated in **P3 figure 3** in the main article.
(2) the 3.9 eV peak is better suited for mapping order/disorder differences as it provides higher contrast due to the larger intensity difference between matrix and nanostructure at this peak position.

4. Further Validation of SEHI for mapping of nanoscale order in semi-crystalline polymers by comparison to Raman microscopy on the example of microporous polypropylene sample

Microporous polypropylene (MPP) was chosen as this material exhibits order variations on both nano and micron-scale. Mapping the latter in polypropylene is well established using Raman spectroscopy. The Raman bands of 809 cm^{-1} and 841 cm^{-1} are said to be spectral markers of crystallinity, that is, as the crystallinity increases the intensity of the 809 cm^{-1} peak increases with respect to the 841 cm^{-1} peak. Furthermore, Nielsen et al[5] concluded that the 809 cm^{-1} band corresponds to the longer helical chains associated with the 3D architecture and the 841 cm^{-1} band is a result of shorter helical chains associated with the amorphous or mesophase regions. A typical Raman spectrum of MPP is shown in **P3 Figure S6** a) with insert S6 b) showing an enlargement of the 809 cm^{-1} and 841 cm^{-1} peaks. The line scan intensity plots **P3 Figure S6** c) and d) show the average intensities for these two wavenumbers over a distance of 50 μm. It is quite clearly observed that the average level of crystallinity (the ratio of 809 cm^{-1} to 841 cm^{-1}) changes considerably over this distance and the values of these two peaks are closely related. **P3 Figure S6** e) is an SEHI image (0-6eV). The red dashed circle highlights a region that is composed

predominantly from the darker contrast regions, with the blue dashed circle highlighting a neighbouring region which is dominated by the porous region. These Raman maps and the SEHI image both reveal neighbouring areas of micron scale ordered/high crystallinity and disordered/low crystallinity regions but contributions from the nanostructures can not be resolved.
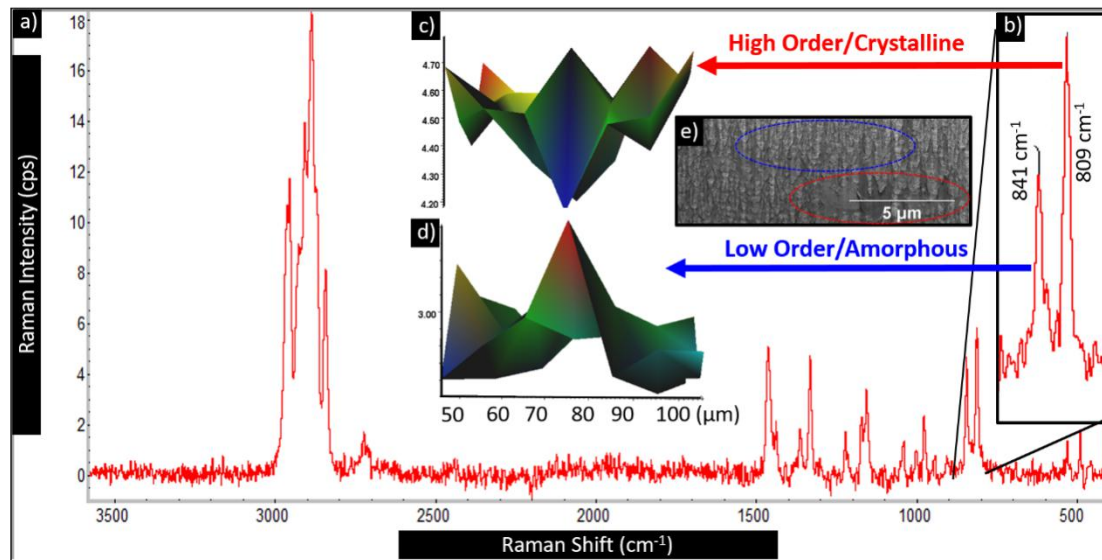
P3 Figure S6. a) A Raman spectrum from 300-3200 cm^{-1} showing Raman peaks in PP, b) An enlarged section showing peaks 809 cm^{-1} and 841 cm^{-1}, c) A 50 μm line map using the peak at 809 cm^{-1} d) The associated 50 μm line map using the peak 841 cm^{-1} e) Micron scale Low Voltage SEM micrograph (TLD 500V) (The data in this figure is provided by A. Talari and I. Rehman)

Higher magnification SEHI images, **P3 Figure S7** a) and S7 b), are required to show the typical lamella morphology (highlighted by the red arrows) interlaced with porous regions (highlighted by the blue arrows) at the nanoscale.
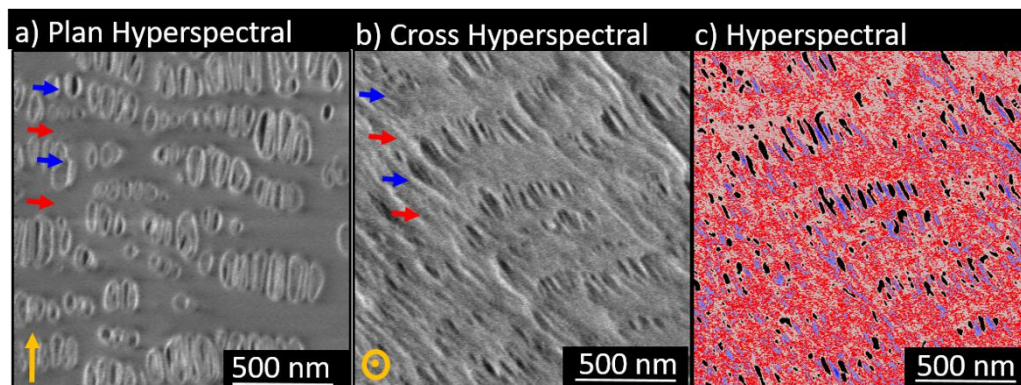
P3 Figure S7. a) Plan view hyperspectral SE image of MPP collected using the energy range 0-6eV, b) Cross-sectional hyperspectral SE of MPP cross-section using energy range 0-6eV c) Associated image of b) further filtered to isolate SE energies between 4.2 and 6eV (energy window of 1.8 eV.) Image has been color coded according to the individual gray levels to directly reflect the phases present. All images taken by acceleration voltage 500V and working distance of 4 mm. Orange arrow illustrates the film extrusion direction. (This figure is provided by K. Abrams)

The dark appearing lamellae are connected by bridges that separate pores which are elongated in the direction of film extrusion, ED (highlighted by the orange arrow and the orange circle when extrusion direction is into the film). According the published models for MPP[5], the material surrounding the pores (bridges) is more disordered than the lamella. These SEHI images produced by SE energies between 0 and 6 eV show clear contrast between the lamellae (darker) and the material surrounding the pores (brighter) and therefore it is concluded to be suitable to reveal the phases of different molecular order at this scale. Some literature describes the bridges as fibrils [7]. The average fibril width is 25 nm. A further reduction of the SE energy window down to a width of 1.8 eV in **P3 Figure S7** c) makes the bridges even more discernible from the crystalline lamella (colored red in **P3 Figure S7** c) by their increased secondary electron emission in this energy region (4.2-6 eV). The brighter phase (colored blue in **P3 Figure S6** c) highlights the bridge structures between the pores therefore this must be the aforementioned oriented amorphous phase. This contrast enhancement for the amorphous component at ~4.2eV correlates with analysis of the amorphous contribution in the silk (see main document **P3 figure 3**b) and d).)

We conclude that mapping of phases of different molecular order in MPP is possible on the nano- scale with SEHI in both plan view and cross-section.

SE spectra were measured using a FEI Helios UC G3 using a 500 V accelerating voltage at 4mm working distance. An iFast recipe (Developer Kit version 3) automatically changes the mirror voltage through -15 to +15 V with 0.5 V steps to collect the whole electron energy range. Images collected at each step were collected and processed in Image J to determine the mean intensity. Same brightness and contrast settings were used to ensure that the same range of grey levels were used for each image. Final SE spectra were obtained from the differentiation (processed by Origin 8.5.1) of the mean values of the MV sweep.

5. Establishing number of phases present in silks by SEHI and quantification of relative phase fractions

Above we have established on two different materials systems that SEHI is suitable for the mapping of molecular order. For the silks we identified the 3.9eV peak as most suitable to map high order material. In an ideal two phase system, collecting the signal using this SE peak should result in a binary image, in which the ordered phase appears bright and the disordered phase black and the histogram would contain two well separated peaks. This is clearly not the case in the histograms in **P3 Figure S8** a) and b) where we try to fit two phases (thus two peaks). Based on these histograms one could conclude that there is no phase separation. However, this is not observed in the SEHI images, as shown in two original gray level images in **P3 Figure S8** c), d). Pixel with the highest gray levels are clearly only found within the well defined nanostructures. The nanostructures also contain a large number of pixels (resolution of the image shown here is 3 nm/ pixel) thus these observations cannot be a simple noise artefact. Careful inspection of **P3 Figure S8** c), d) shows that there are actually three distinct gray levels present. This is expected if the ordered phase is not entirely crystalline and there exist oriented structures even within a disordered phase. Note that in section 3 we found, based on SE spectra of matrix and nanostructure and similarity in intensity in peak 9, that the nanostructures might

contain a disordered component or some of the matrix could contain more ordered components. From the spectra alone we could not say which is the case.
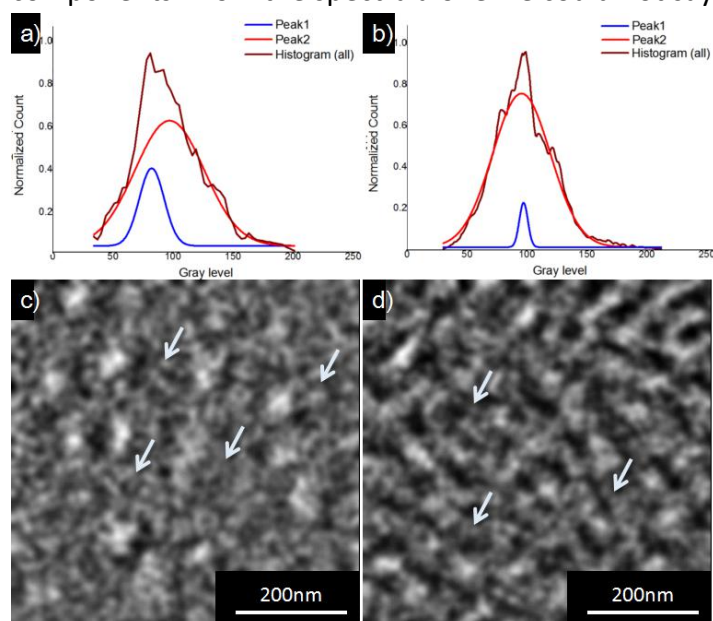
P3 Figure S8. If two peak fitting is attempted (to represent ordered and disordered phases only), the fitting of the histograms obtained from SEHI images of *B. mori* a) and *A. mylitta* b) cannot clearly represent any phase separation. Original SEHI images of *B. mori* silk c) and *A. mylitta* silk d) is shown with oriented amorphous phase, which is meta brightness area between bright ordered structures, highlighted by arrows.

However, such variations in overall order would be reflected in the brightness of each pixel in the SEHI image, which is highest for the most ordered locations only when imaging is carried out using the 3.9eV SE peak. Less well ordered, often call oriented amorphous areas appearing darker and the amorphous phase being the darkest. Therefore, the histograms in **P3 figure 2** e), f) in the main article, were fitted with three Gaussian peaks. The fitting was carried out using Origin. The fitting function was set to find positive peak only using "residual after 1st derivative" method. The parameters of the fitted Gaussian function of each peak in the histogram is listed in **P3 Table S3**. These peaks form the basis for the false color used to represent the three phases.

The histogram area was selected relative to the size of the nanoscale features, in order to obtain a fair representation of the all phases in the histogram (500 nm × 500 nm for *B. mori* silk and 300 nm × 300 nm for later *A. mylitta*). Otherwise the latter is so strongly dominated by the matrix gray levels, that is becomes hard to identify the correct peak positions for the two minor phases.

**P3 Table S3**. The Gaussian fitted function parameters of histogram in **P3 figure 2** in main article

	y_0^*	x_c^*	A^*	w^*
B. mori				
Disordered	5.74	85	3271	39
Oriented	5.74	119	817	24.5

amorphous				
ordered	5.74	139	360	16.5
A. mylitta				
Disordered	4.53	87.5	5411	42.6
Oriented amorphous	4.53	98	569	12.9
ordered	4.53	122	1796	30.7

*The fitting function used is $y = y_0 + \dfrac{A}{w\sqrt{\dfrac{\pi}{4\ln 2}}} e^{-4\ln 2 \times \frac{(x-x_c)^2}{w^2}}$

The link between peak fitting and thresholding is demonstrated in **P3 Figure S9**. The area fractions obtained from the thresholded image is slightly different from the peak area fraction obtained by the histogram fitting. As shown in **P3 Figure S9** a), the slashed area is the amount of pixels above the selected threshold, which is chosen by excluding the gray level containing the oriented amorphous phase. This thresholded area is shown in **P3 Figure S9** b). If we exclude the objects with diameter smaller than 10 nm in the image (which is far below the size of nanofibrils), the area fraction obtained from the Gaussian peak fitting is equal to the nanostructure fraction obtained from the thresholded image.
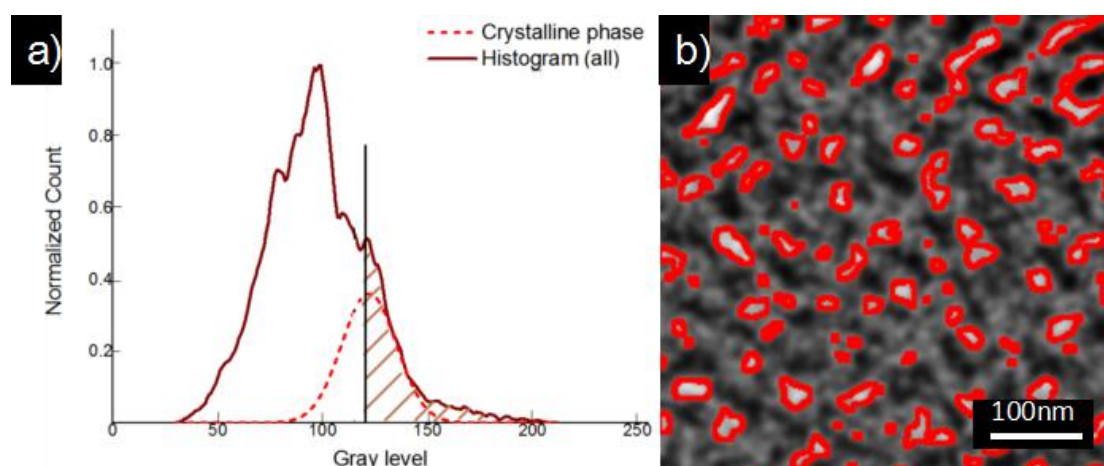
P3 Figure S9. The dashed area in a) represents the fraction calculation obtained from thresholding compared to the red peak area from the fitting. This area fraction is equal to the highlighted area shown on the SEHI image b).

6. Measurement of dimensions of phases based on SEHI topography free images

Images were processed using ImageJ v1.48 for the purposes of feature size analysis. The images were filtered from 9 nm to 120 nm with band pass filter to minimize the effect of noise. The feature size distribution is analyzed by using the threshold gray level values selected in the histogram as shown in **P3 figure 2** e) and 2 f) (main article). Since the feature size is analyzed in this way, a topography related edge effect[8] will generally increase the brightness of the edge and thus increase the size of measured feature. This effect is clearly visible in the nanostructure in *A. mylitta* silk shown in **P3 P3 Figure S10** a), when we analyze this standard SE image by line

profiles (**P3 P3 Figure S10** b)). Such edge effect is very well known to influence nanoscale critical dimension measurements and is hard to account for as it is feature size and shape dependent[9]. The edge effect is recognised by a bloom[9], that increases the intensity at edges and can lead to tens of nanometers of ambiguity. This edge effect is clearly absent in the line profile taken from the same structure but from the 3.9 eV SEHI image (**P3 P3 Figure S10** c)). Furthermore, profile plots extracted from standard SE image yields a diameter of 48 nm while the SEHI image of the same feature gives a diameter of only 36 nm as shown in figure S 10 b), c).
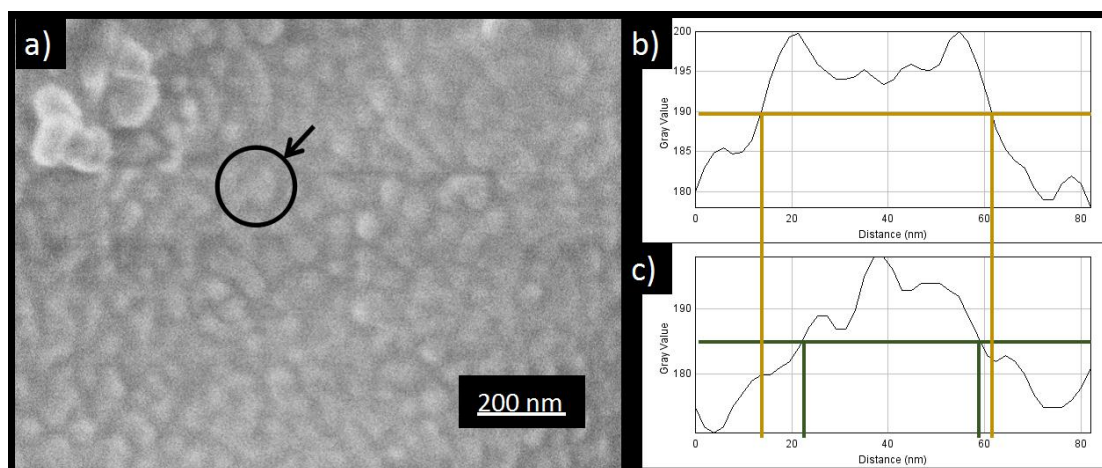

Figure S 10. A nano-structure within the image of *A. mylitta* silk cross-section in a), and profile plot of the highlighted nanostructure in standard SE b) and hyperspectral SE c). The yellow and green lines in the profile plots is the threshold cut off of the ordered phase in each respective image. Note the profile in c) is normalized for comparison purposes.

The above observation is not specific to the particular nanostructure analyzed in **P3 P3 Figure S10**. The images in **P3 P3 Figure S11** shows more *B. mori* samples (S11 a), b)) and *A. mylitta* silk (S11 d), e). The average size and distribution of different samples shows very similar trend: the shape of nano-structures are rather uniform for both species and the smaller nanostructures in *A. mylitta* silk shows a much denser distribution. The detailed measurement by different SEM techniques are shown for *B. mori* silk (**P3 P3 Figure S11** c)) and *A. mylitta* silk (**P3 P3 Figure S11** f)). All measurements carried out using SEHI yield a smaller diameter, ~40 nm for *B. mori* silk and ~ 33 nm for *A. mylitta* silk since the SEHI has higher resolution due to a suppressed edge effect. The absence of an edge effect in the SEHI further confirms that the information is not topographical. From **P3 P3 Figure S11** f) we also confirm that neither standard low voltage SE nor BSE imaging are able to resolve the smaller structures that only become clearly visible by SEHI.
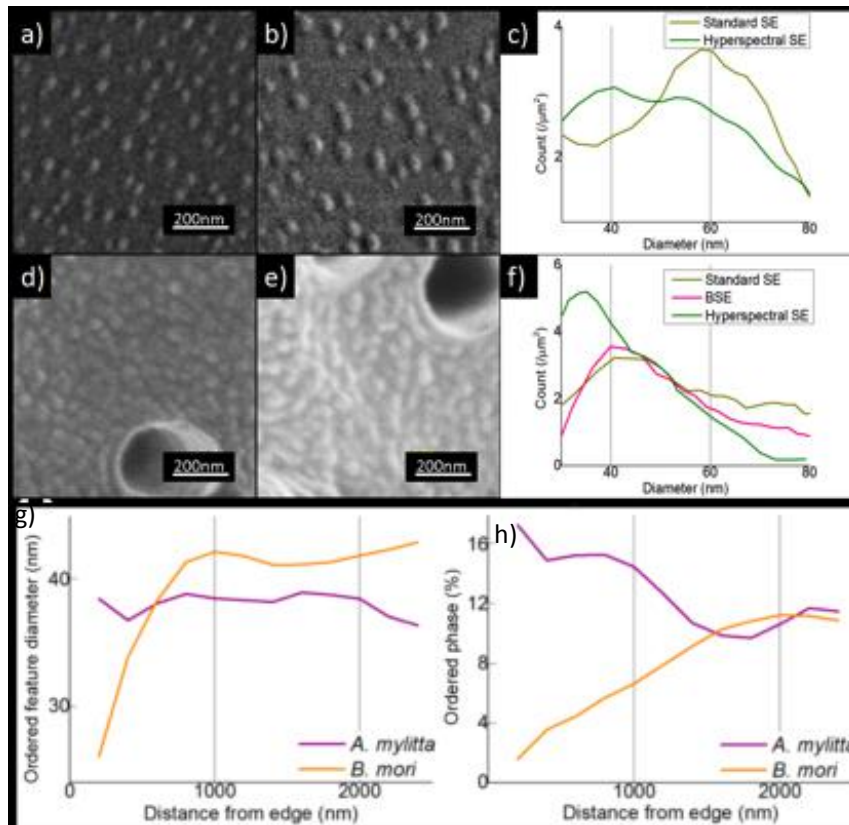
P3 P3 Figure S11. Standard SE images of *B. mori* a), b) and *A. mylitta* d), e) silk. Note due to the sample not being perpendicular to the electron beam the nano-structure in a), b) appear elliptical in shape. The nanostructure size distribution is provided using different SEM techniques in c) for *B. mori* silk and f) for *A. mylitta* silk. The variation of the diameter of ordered structures as extracted from SEHI is shown in g) and the variation of order phase fraction is presented in h).

7. **Elongated tubular vacuole and microscale related features in silk fiber longitudinal section**

A large number of elongated tubular vacuoles can be observed in either longitudinal section or cross-section of *A. mylitta* silk. In order to calculate the distribution density of the nano-structures, we need to exclude the area occupied by vacuoles in the *A. mylitta* silk fiber cross-section images. The distribution shown in **P3 P3 Figure S12** is calculated by summarizing the vacuoles in 200 nm wide rings and the *x*-axis is the difference between selected ring and the fiber radius, thus also the distance from fiber edge to vacuole. The volume fraction of vacuoles is normalized for the area of the ring, this is done to enable the data collection from silk fibers of different radii.
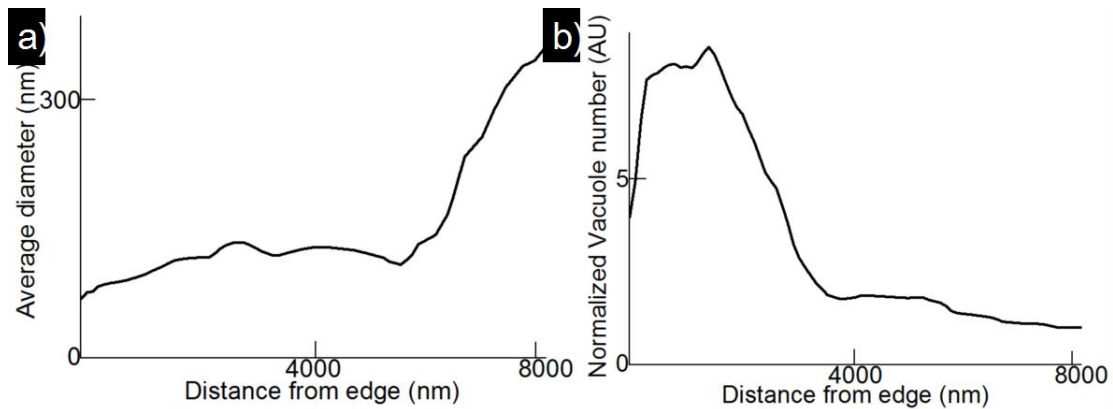
P3 P3 Figure S12. The vacuole diameter a) and average normalised fraction b) distribution of vacuoles versus distance from the fiber edge. The fraction is averaged from three different fibers and it is normalized for different datasets depending on the diameter differences of those fiber samples.

The vacuoles exhibit at a size at ~150 nm, except in the center of the silk fiber. The number of the vacuole is much large in the outer part of the fiber. We noticed a large number of small vacuoles present in the ring zone 0-2000 nm from fiber edge, this is also the zone that yields a larger number of nanostructures discussed in manuscript. The longitudinal section also shows the microfiber bundles and a specific nano-pattern on *B. mori* silk. A standard SEM image of *B. mori* silk longitudinal section is presented in figures S13 a) and a pattern suggesting the appearance of "V-shape" features can be observed. There is a large angle between this pattern and the hundred nanometer fibers as seen clearly in the color coded area in **P3 P3 Figure S13** b). Considering the appearance of this nano-pattern, the V-shapes are expected to be parallel to each other in longitudinal direction along micrometer length of fiber, thus similar to the "cup-shaped" features described in the literature[10].
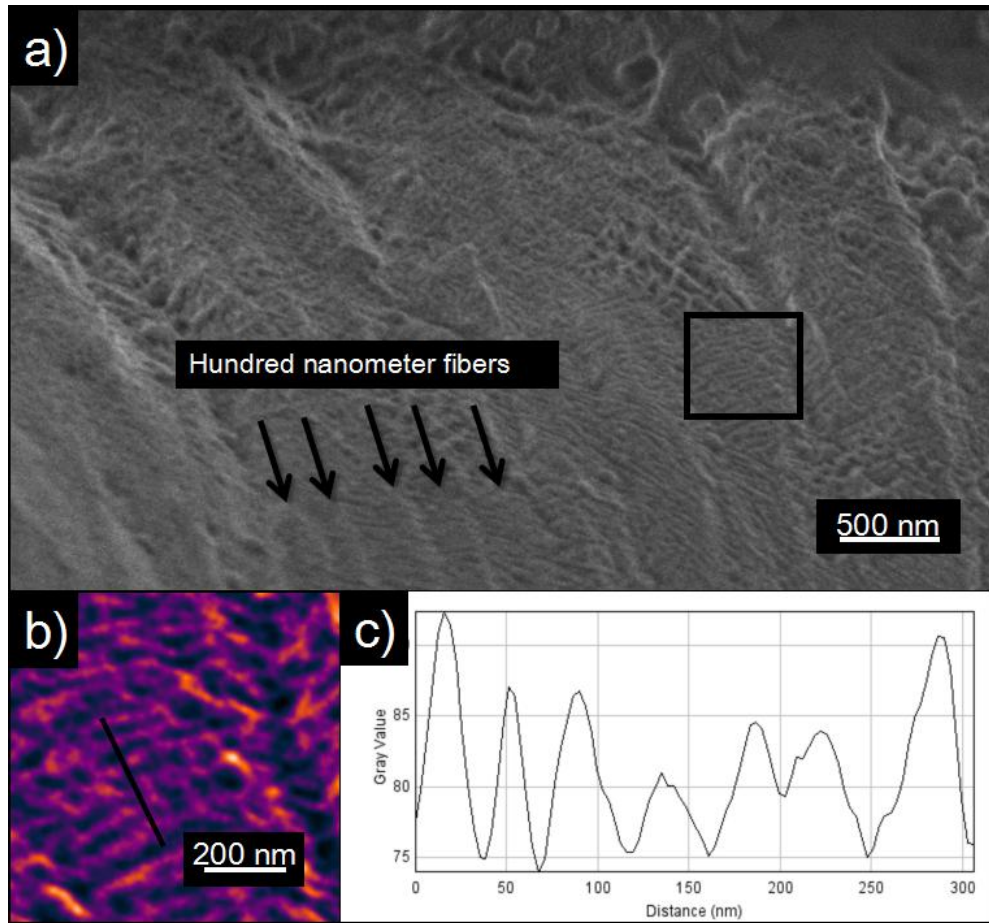
P3 P3 Figure S13. Image a) is the high magnification view of **P3 figure 1** d, the arrow highlights the hundred nanometer microfibers and the image b) is the zoomed in view of the highlighted area, showing the nano patterns in longitudinal section. The line profile of the line in b) is shown in c), yielding a uniform 50 nm width for this pattern. Note the color coding in b) is only topographical, and is not based on crystallinity/order information.

However, due to the limitation of sample area and the lack of prominent features to identify the direction in *B. mori* silk longitudinal section, the direction of this pattern in whole fiber cannot be confirmed from this image. The line profile in **P3 P3 Figure S13** c) is from the line marked in the zoom in vision **P3 P3 Figure S13** b), the nano-pattern yields a rather uniform repeat distance of ~50 nm in longitudinal direction.

8. Excluding Beam damage and plasma etching artefact

Since natural silk is a beam sensitive material, the damage from the electron beam in SEM and the possible artefacts created by plasma etching during sample preparation was investigated in order to ensure that the data presented in the main article are free from artefacts.
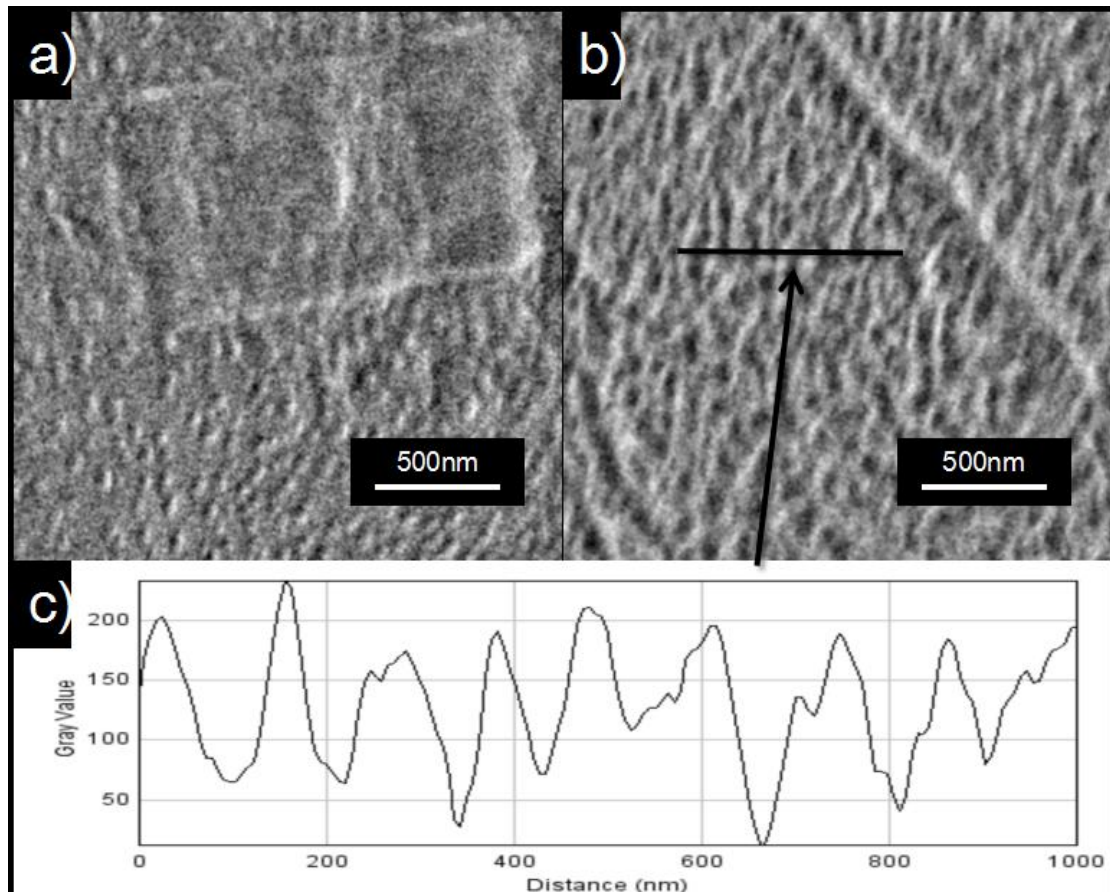
P3 P3 Figure S14. A square beam damaged area on a *B. mori* silk cross-section is shown in a). A plasma etching artefact pattern using the same etching setting in our sample preparation on a flat sericin surface is shown in b). c) is the profile line of the black line highlighted in b), showing the scale of the repeating plasma artefact pattern.

Lower magnification images (3 nm/pixel) and high magnification image (1.5 nm/pixel) were collected with an electron dose per scan of 0.053 mC/cm^2 and 0.213 mC/cm^2 respectively. To test for the effects of electron beam damage we increased the electron dose to dose 51.12 mC/cm^2 (e.g. 1000 times that of a low magnification image) by exposing an 800 nm × 1400 nm square area on the *B. mori* silk cross-section for 240 scans in 1.5 nm/pixel resolution to obtain some clearly visible electron beam damage as shown in figure S 14 a). The nanostructure in the beam damaged area is obviously not as well defined as the undamaged area. Since this damage effect does not create additional nanosize artefacts and will be easily seen during imaging, it proves that the nanostructures observed in our imaging were not created, or heavily affected, by beam damage.

In order to identify the artefacts created by plasma cleaning, we exposed a silk sericin surface to the same plasma conditions and duration. If the plasma exposure leads to artefacts that are unrelated to original existing nanostructures present in the fibroin, the pattern created should be very similar to the pattern created on this sericin surface. As shown in **P3 P3 Figure S14** b), c), the plasma generated pattern in sericin is an inter-connected repeat pattern at about 100-200 nm scale. This is much

larger than the nanostructures we observe on the fibroin, and it also has significant different surface morphology. Thus we can confirm the nanostructure we observed is not simply random artefacts created by plasma etching.

References

[1] L. F. Drummy, B. L. Farmer and R. R. Naik, *Soft Matter*, 2007, 3, 877

[2] Q. Wan, R. C. Masters, D. Lidzey, K. J. Abrams, M. Dapor, R. A. Plenderleith, S. Rimmer, F. Claeyssens, C. Rodenburg, *Ultramicroscopy* **2016**, *171,* 126

[3] C. Z. Zhou, F. Confalonieri, M. Jacquet, R. Perasso, Z. G. Li, J. Janin, *Proteins: Struct., Funct., Genet.* **2001**, *44*, 119

[4] R.C. Masters, A.J. Pearson, T.S. Glen, F.C. Sasam, L. Li, M. Dapor, A.M. Donald, D.G. Lidzey, and C. Rodenburg, *Nature communications*, *6,* **2015***,* 6928

[5] A. S. Nielson, D. N. Batchelder, R. Pyrz, *Polymer* **2002**, *43*, 2671

[5] a) R. J. Xu, C. Lei, Q. Cai, B. Hu, W. Shi, H. Mo, C. Chen, *Plast., Rubber Compos.* **2014**, *43*, 257 b) A. Saffar, A. Ajji, P. J. Carreau, M. R. Kamal, *Polymer* **2014**, *55*, 3156 c) S. H. Tabatabaei, P. J. Carreau, A. Ajji, *Polymer* **2009**, *50*, 3981

[7] J. Qiu, Z. Wang, L. Yang, J. Zhao, Y. Niu, BS Hsiao, *Polymer* **2007**, *48*, 6934

[8] D. C. Joy, C. S. Joy, *Micron* **1996**, *27*, 247

[9] Y.G. Li, P. Zhang, and Z. J. Ding. *Scanning* **2013**, 35(2), 127

[10] S. Yu, M. A. Johnson, D. C. Martin, *Macromolecules* **1998**, 31, 8857

4.3 Validation of SE spectrum for other bio-polymer composites: silkworm silk artificial films and spider silk fibers

4.3.1 Validation of SE spectrum on silkworm silk artificial films and comparison with UV technique data

In section 4.2 the morphology analysis of silk hierarchical structure is presented using SEHI. The SE spectra of fibroin is very complex. Although there is proof that the spectra are not a result of errors or artifacts, little of its physical meaning for protein materials is understood. Thus the SEHI technique was applied on artificial silk films to validate our SE spectra. The effect of material shape, beam penetration and contamination build up can be best controlled in artificial silk structures. Two silk samples are used for our SE spectra validation, including a silk fibroin artificial film with higher crystallinity artificial features and a set of silk thin film (~10nm) spin coated from silkworm gland cross-section solution.
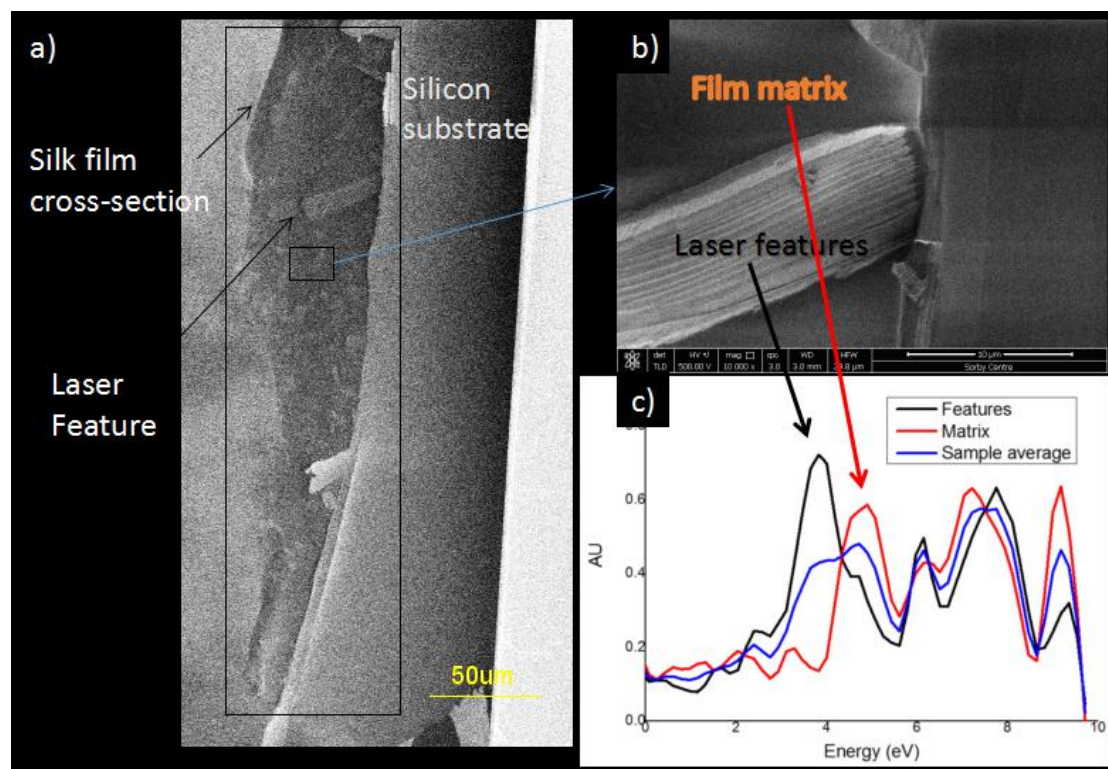

Figure 4.3.1. The cryo-snapped cross-section of a artificial silk film is shown in a), with the higher crystallinity feature highlighted. The image b) is the zoomed in area of cross-section shown in a). The SE spectra of features and matrix is collected separately and compared with the average spectra of sample in c).

The first silk film sample is composed of the film matrix and the artificial line features "embed" in the film. A crystallinity difference between the feature and matrix allow them to behave differently in the fracturing process. Thus using the cryo-snap technique as mentioned in 4.2, the phase separation between matrix and laser exposed feature on the film cross-section can be observed. This is shown in figure 4.3.1 a, b), based on the SE image the laser exposed features can be located and SE spectra from these features and film matrix can be collected. The individual spectra of feature and film matrix, respectively are shown in figure 4.3.1 c). The most part of SE spectra of both laser exposed feature and matrix is very similar, except the size difference of the 3.8eV (cannot confirm due to energy resolution not high enough to separate 3.8eV and 4.0eV peak) and 4.4eV peak. The laser exposed feature yields a much larger 3.8eV peak than matrix but a smaller 4.4eV peak. The error of peak position due to the energy step size (0.16eV for these spectra) needs to be considered. Thus if we assume the 3.8eV peak and 4.4eV peak here equal to the 3.9eV crystalline fibroin peak and 4.2eV amorphous fibroin peak used for natural fiber in 4.2, this peak difference shows the feature's crystallinity is higher than that of the matrix.
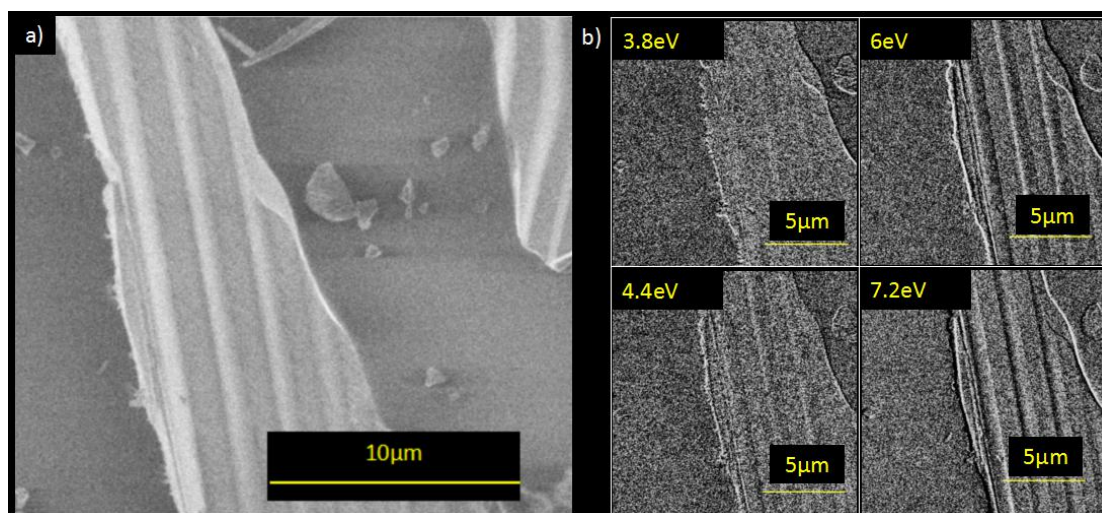

Figure 4.3.2. A SE image of a higher crystallinity feature on film matrix is shown in a), this feature is also imaged by SEHI using SE peak 3.8eV, 4.4eV, 6eV and 7.2eV in b).

Further evidence is shown in the SEHI image array in figure 4.3.2. A SE image of one laser feature (figure 4.3.2 a)) is compared with the SEHI images of the same feature collected using 3.8eV, 4.4eV, 6eV and 7.2eV peaks (peak width 0.6eV according to SE spectra) on the silk film SE spectra. The 3.8eV peak in the SE spectrum obviously yields contrast only depending on the composition difference (note it cannot be confirmed this is only caused by crystallinity due to lack further evidence for this specific material), since the topographical line features yield little signal in SEHI image. The laser feature appear brighter than matrix phase in this energy window, as it yields more signal in crystalline fibroin peak. There is no longer a clear contrast between two phases for images collected using the 4.4eV peak. Topography contrast becomes dominant in images collected with the 6eV and 7.2eV peak, respectively.

This is shown by the strong edge effect of laser feature in figure 4.3.2 b) as well as the noticeable inverse topography contrast yielded by 6eV and 7.2eV peak. This shows the formation of SE topography contrast also involves multiple peaks in SE spectra.

Compared with the SE spectra collected on natural fibers in 4.2, much signal is lost in the lower energy region (0-3eV) but still kept a number of low energy peaks. This may be because the overall shape of the low energy region could be affected by the shape of sample surface. More evidence that this overall shape change along with the surface inclination angle with respect to electron beam is shown in section 4.3.2. The origin of small peaks in this region is not a result of topography, since many of these peaks are repeatable for different complex shaped natural fibers at the same energy value. On the other hand, the peaks in higher energy region (6eV or higher) are much more unstable and only repeatable on artificial silk films. As shown in the SI 2 of 4.2, the SE peaks in higher energy region in natural fiber can not be repeated in different samples. This can be explained by the fact that the higher energy SE peaks are actually topography peaks. Thus, those peaks can only be repeated on samples with regular or flat surface, for example the artificial films.
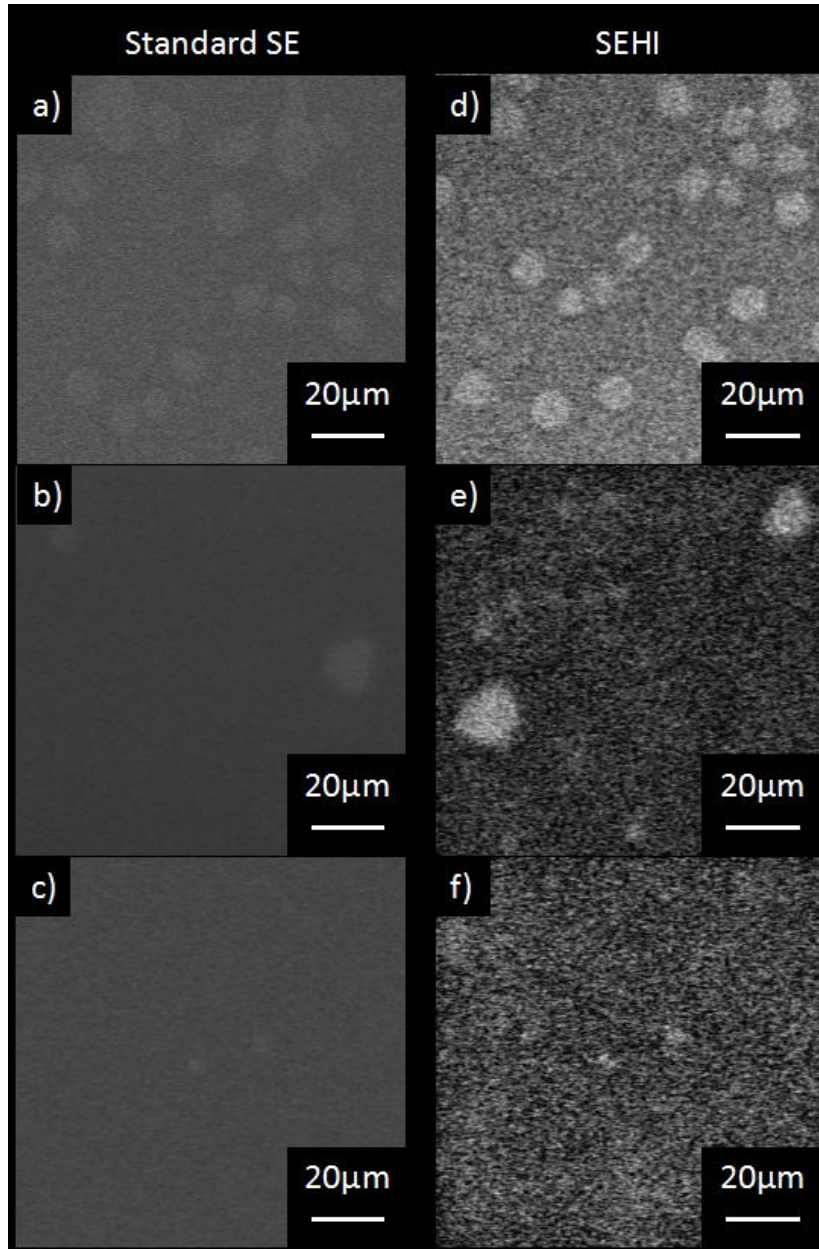
Figure 4.3.3. The SE image and SEHI image of one set of silk gland cross-section spin coated films. The energy window for the SEHI images is 0-2eV.

As concluded above the SE peaks in energy region > 6eV are topography signals, I applied our SEHI technique on a thin silk film (spin coated using dissolved silkworm gland) to study the effect of composition on the lower energy region peaks. One set of thin silk film in different location of the gland was used and each cross-section contain different fraction of sericin and fibroin. There is no phase separation in the fibroin since the silk gland has not crystallized in those cross-sections of gland and silk III is not a stable form. Only amorphous fibroin and sericin exists in this part of silkworm gland. Thus only two micrometer-scale phases exist in those gland films, which are the sericin phase and amorphous fibroin phase. According to the SE spectra collected from the two phases (figure 4.3.4), the major phase yield very

similar peaks as the natural fibril despite the crystalline peak. Combined with the sample information, it can be concluded the major phase is fibroin phase and its spectra show significant difference with the minor sericin phase at 0-2eV. The SE images and SEHI images collected in this window showed the same phase distribution. Thus the phase identity of the minor phase can be confirmed to be sericin and its decreased prevalence in the silk gland cross-sections is shown in the images of a series of cross-sections as shown in figure 4.3.3.
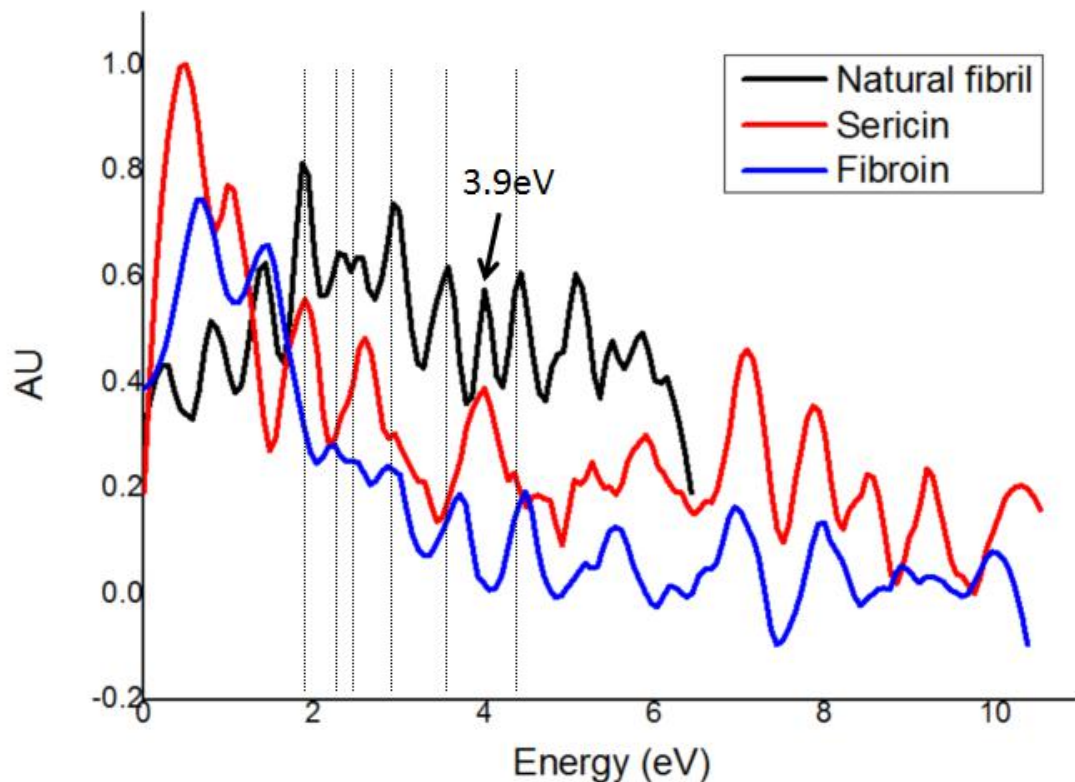

Figure 4.3.4. The SE spectra collected from the sericin and fibroin phase on the silk gland film, comparing with the spectra collect from the natural fiber nano-fibrils.

The SE spectra collect on sercin phase and fibroin phase of silk gland film are compared with the the spectra of natural silk nano-fibril as shown in Fig 3.3.4. The sercin and fibroin yield similar peaks in > 6eV energy region. This is expected since two phases are both located within a thin and flat film and as a result do not have much topography difference. On the other hand, the other part of SE spectra are very different for   the two phases. First, many of SE peaks in <6 eV region are different for sericin and fibroin, the shape and location of those peaks cannot be matched at all. Second, the sericin yields a larger peak at the onset of spectra, showing the highest contrast between the two phases in an energy region < 2eV. This difference may be due to the electron affinity (work function) difference between two proteins and I used this energy window for SEHI of these two phases.
The large difference between peaks yielded from sericin and fibroin, respectively indicates that the peaks <6eV are related to certain protein structures. In order to

identify these SE peaks, comparison of the spectra of silk thin film fibroin and natural fiber nanofibril in figure 4.3.4 is made. The nanofibril represents the crystalline fibroin in a natural fiber in this comparison. First, if we compare the 3.9eV and 4.2eV peaks, the gland fibroin only yield the 4.2eV amorphous peak but lacks the 3.9eV crystalline peak. This matches the fact that gland fibroin did not crystallize[210] and therefore is not expected to yield crystalline peak. Second, most of the SE peaks <6 eV occur at the same energy for both gland fibroin and natural fibroin. This includes the 1.7eV, 3eV, 3.6eV peaks and the double peak at ~2.4eV. A 2eV peak in gland fibroin spectra is not seen but can be covered by the long shoulder of 1.7eV peak. In conclusion, almost all the SE peaks in 1-5eV region can be matched for gland fibroin and natural fiber fibroin, despite the very different overall shape of the spectrum in this lower energy region.

Combining the above with the comparison between sericin and fibroin, the SE spectra can be understood as follows: 1) The higher energy (> 6eV) SE peaks correspond to topography, which is inline with literature data on inorganic materials[211]. 2) The overall shape of SE spectra <3 eV may be affected by the sample surface inclination with respect to the incident electron beam. 3) SE peaks in lower energy region correspond to the protein structure.

According to the mechanism of electron emission, each SE emission peak corresponds to energy difference between certain electron energy bands of the sample molecules. Thus other types of spectroscopy should also show certain structures or peaks at those energy values. Since the energy region is below 6eV as discussed above, the UV light technique also covers similar energy region.

Since the artificial silk film with laser feature also contain riboflavin, the UV absorption spectra of whole film is calculated by subtracting with the spectra of riboflavin. Thus we can compare the spectra change from 3eV to 5.5eV before and after the UV laser exposure. The UV absorption data show a similar trend of 4.0eV peak increase as shown in figure 4.3.1 a).

This similar trend suggest a possible match between SE spectra and UV spectra. There is a set of UV absorption/fluorescence data of silk fibroin solution before/after UV light exposure[212] published by other researchers. Although our artificial silk film is not UV exposed in solution state, the effect of UV exposure on silk fibroin should be comparable. We can compare the SE peaks in spectra of artificial silk film matrix(non-exposure)/laser feature(exposed), silk thin film fibroin (regenerated fibroin)/sericin (regenerated sericin) and natural silk fibril to compare with UV spectroscopy data. This is shown in table 4.3.1. Since any structure in UV spectra (not only major peaks) correspond to energy absorption thus energy bands, all the energy value where UV spectra show obvious structure is compared to SE peaks. Note the UV data only extend from 2eV to 5eV.

Table 4.3.1 The comparison between the structure energy values of electron and UV spectra from 2eV to 5eV

Energy (eV)	UV N-exp	UV exp	SE-AF N-exp	SE-AF exp	TF fibroin	TF sericin	Natural fibril
2.0	Y	N	Y	N	***	Y	Y
2.6	Y	Y	Y	Y	Y	Y	Y
2.88	Y	Y	***	Y	Y	**	Y
3.8	N	N	N	*	*	N	Y
4.0	N	Y	N	Y	*	Y	Y
4.4	Y	Y	Y	Y	Y	N	Y

UV is UV spectroscopy, SE is SE spectra, AF is artificial film, TF is thin spin coated film, N-exp is not exposed to UV (UV laser) radiation, exp is exposed to UV (UV laser) radiation.

* the regenerated fibroin lack crystalline peak, as well as the literature UV data. The fibril do have one more peak, but if this is 3.8eV or 4eV remains unclear

** the sericin show a slight shoulder at ~3.0eV, not sure if it is the same peak

*** means the peak is not in expected location but yield an unexpected peak within 0.25eV, may be shifted

First it can be noticed UV data agree with SE spectra in almost all energy values for artificial film matrix/laser feature except a shifted 2.88eV peak. Second the sericin spectra lack a 4.4eV peak, which is a major absorption peak in UV data of fibroin solution and obviously exist in all fibroin spectra. This suggests a major energy band difference between fibroin and sericin molecules, which also confirms the agreement between UV and electron techniques. Third, as discussed in 4.2, 3.8eV SE peak is highly related to crystalline fibroin. Here only the natural fibril, which is the only highly crystalline fibroin sample in this table, shows this crystalline peak clearly. However, the artificial silk film laser feature has a large peak with over 1eV peak width covering this whole energy region. And the 4.0eV and 3.8eV peak is very close in SE spectra, thus higher energy resolution may be required to separate these two peaks clearly. Last, all the fibroin without UV exposure yield a 2.0eV peak in either UV or SE spectra. This peak disappears after UV exposure in both technique, also showing the agreement for the two techniques.

Despite some of the peaks in SE and UV spectra occupying similar energy region, the

shape of those peaks are quite different. The UV bands from 2.88eV to 4eV are only observed as shoulders in the UV absorption spectra. They are noticed as bands because they show a different trend compared with other part of UV spectra when the UV radiation changes. But it is hard to define the start and end of those bands. The main UV absorption at 4.4eV is very broad compared with any SE peaks. Since the main amino acid of fibroin yield UV absorption at very close energy (4eV and 4.2eV), it is impossible for us to decide the change of conformation by calculating the intensity of these close peaks.

Additional complexity of such agreement between different spectra is caused by the orientation of protein molecules. Such orientation variation can produce shifts in the Monte Carlo simulation of SE spectra, and if spectra from different oriented protein superposition, large amount of sharp SE peaks can be expected. This type of effect is not observable in UV absorption and it is hard to decide which SE peak is produced by such mixture of orientation rather than protein conformation.

In conclusion, the literature UV data show some level of agreement with peak position in our SE spectra in 2-5eV energy region. This suggests our spectra fine structure in the 2-5eV range may be reflected in other characterization techniques and correspond to certain energy bands. However no reference is available to show the exact molecule structure such energy bands related to. Research in the fine SE peaks in this energy region will require higher energy resolution and further work to build a relationship between molecule structure and energy bands.
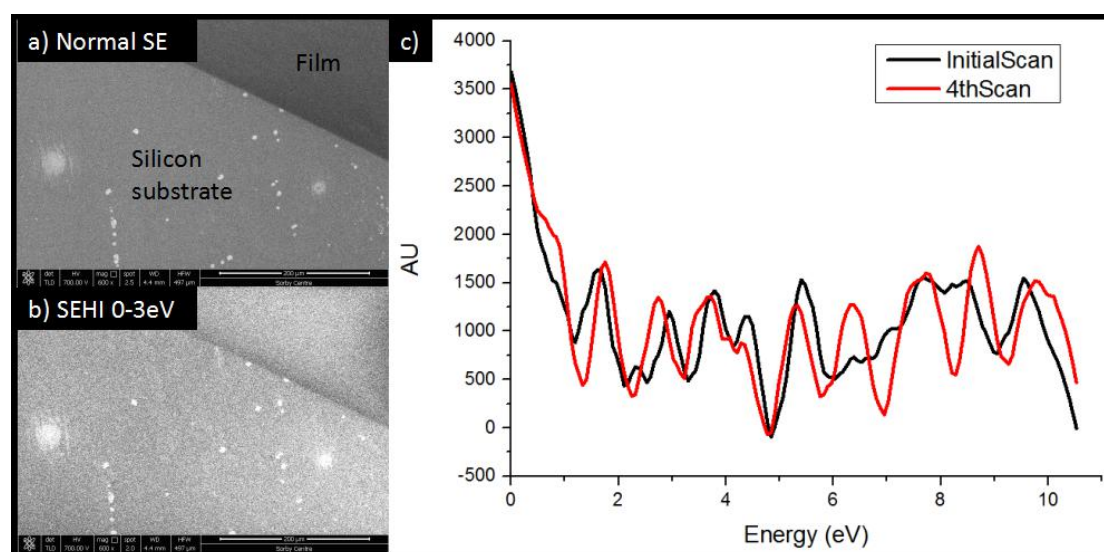
Figure 4.3.5. The beam penetration on the silk gland film is verified by checking for substrate features in SE and SEHI images a) and b). The SE spectra of gland film in first spectra collection and 4th spectra collection in shown in c).

Due to the complexity of our spectra, the beam penetration and damage effect on the thin film sample need to be considered to confirm our data. The thin film applied here is <10 nm thick, if the beam penetration is too deep signal from the substrate beneath our sample would be collected. Thus, we can compare the SE and SEHI

image of the edge of the gland film sample. The features on silicon substrate did not appear in the area our film covered in both images as shown in figure 4.3.5 a, b). Hence it is confirmed our spectra collected on gland film samples at 700V beam voltage is not affected by the substrate. This matches the simulated signal escape depth of 700eV incident electron, which is about 10nm.

The contamination build up can also introduce potential errors for complex protein spectra, so we need to compare the SE spectra collected from a first set of scanning with the ones collected after multiple scanning on the same sample area. The first scan spectra and the spectra after 120μs per pixel radiation by 239μA emission current beam are compared in figure 4.3.5 c). The spectra are slightly shifted for ~0.5eV compared to figure 4.3.4 due to charging effects build up during repeat scanning, but most peaks did not show obvious change < 6eV. Thus the contamination build up on silk samples can be safely excluded in below 6 eV energy region.

4.3.2 Nano-structure mapping and "ageing" features in spider silk

In the study of silkworm silk materials, characterization of the nano-structure and crystallinity variation in hierarchical fiber was done with our SEM techniques. The SE spectrum of complex protein material systems was also explored. The spider silk was chosen for further application of our techniques. The spider silk is not only a very interesting material with remarkable properties, but also composed of hydrogen bonded β-sheet crystals and nano-scale fibril structure, hence is similar to silkworm silk. By studying the similar nano-structure build up by different proteins, the aim is to gain more insight in spider silk itself as well as the application of SEHI on complex protein/polymer system.
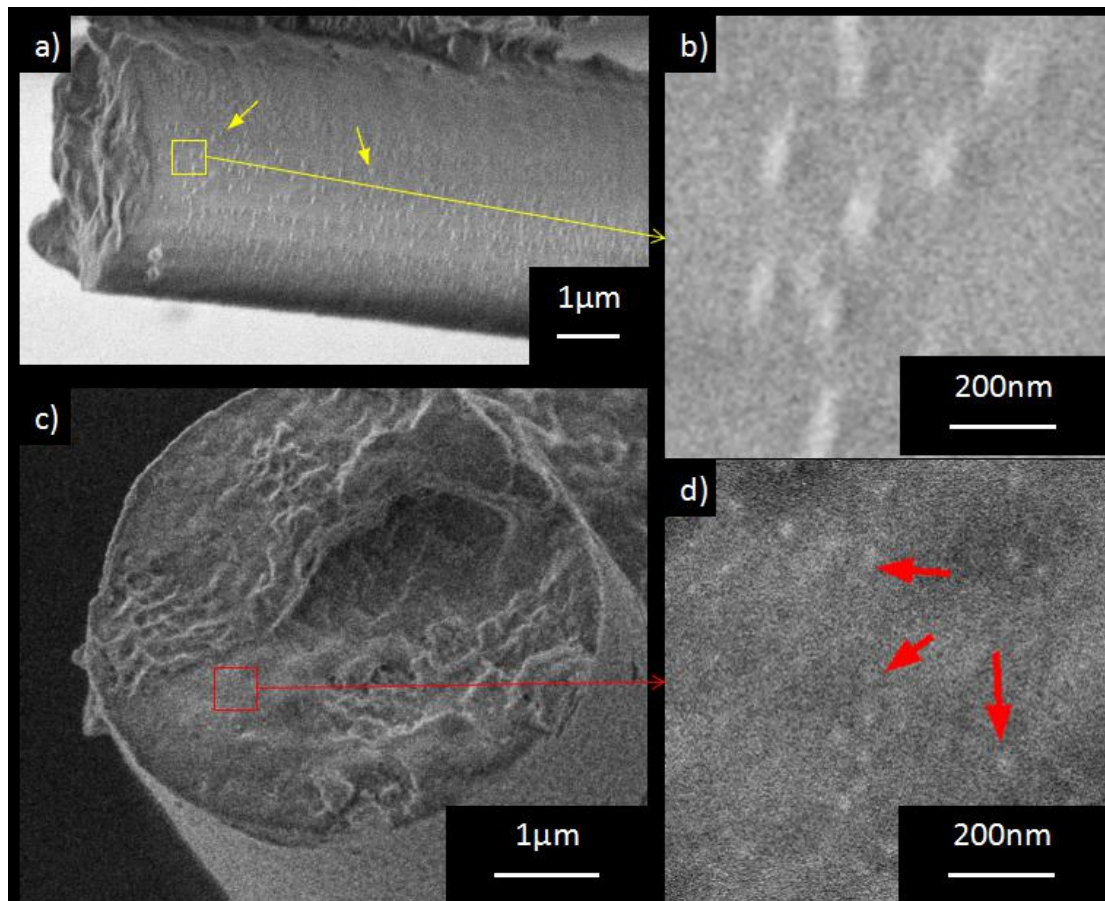
Figure 4.3.6. The outside "skin" of a spider silk fiber is shown in a), the "nano-papillaes" are observed and the image b) shows the zoomed in view. The image c) shows the cryo-snapped cross-section of a spider silk fiber, on which large amount of nano-structures are observed as highlighted in d).

The SE imaging of spider silk has revealed a few different nano-structures, including a ~50nm nano-structure on the "skin" outside fiber and a nano-structure diameter ranging from 20-60nm on the cryo-snapped cross-section of silk fiber. The former is similar to the "nano-papillaes" that exists on the silk band as described by literature[213]. This structure is speculated to contribute to the adhesive properties of certain spider silks. It is noticeable that the nano-structure on the outside of the fiber is larger than those reported ones. However no other similar nano-structures have been reported on spider silk skins, but different species may lead to different nano-structure sizes. The nano-structure on the fiber cross-section, on the other hand, can only be related with the fibril structure in spider silk fiber.

The fibril in spider silk is the major structural component regarding mechanical property formation. AFM studies have shown the fibril adopt a "core-shell" structure, with higher crystalline spidroin1 forming the fibril shell and lower crystalline spideroin2 forming the fibril core[214]. The diameter of whole fibril ranges from 80-100nm while the diameter of fibril core is around 60nm. This scale also agrees to the distribution of spidroin2 protein as nano-groups described by other technique[198]. Here if we assume the size variation of nano-structure in our sample cross-section

follow the same trend as shown by nano-fibril in silkworm silks in 4.2, the nano-structure in our sample cross-section can be matched with the fibril core described in literature[208].
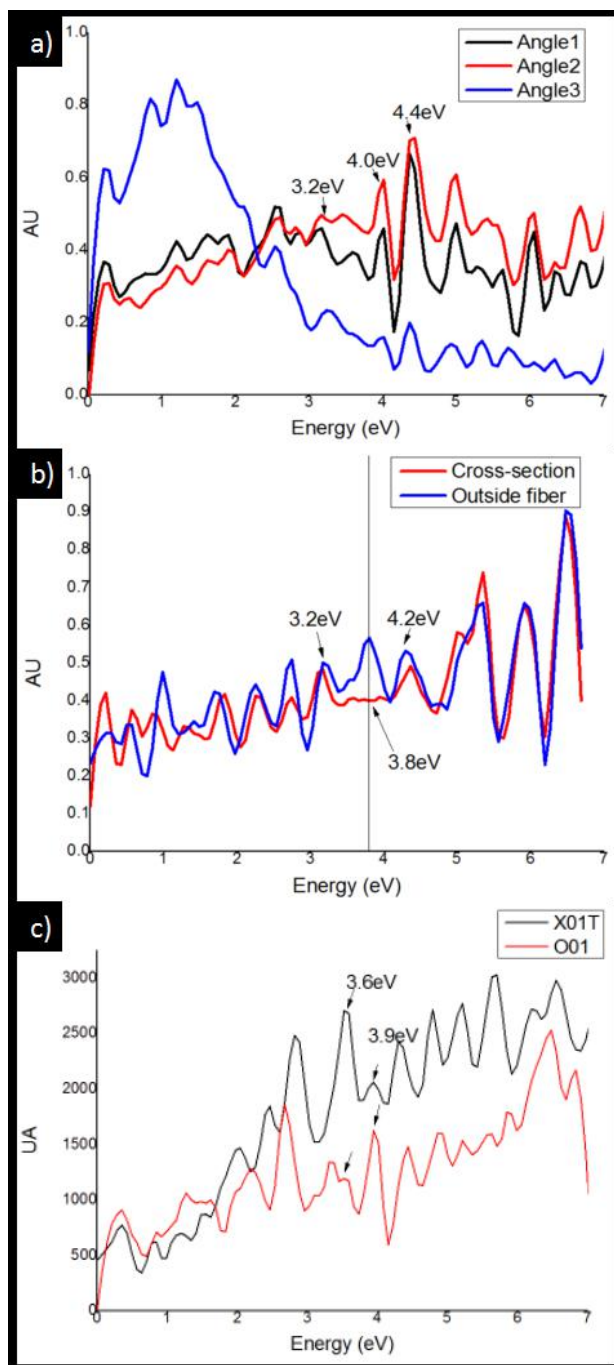
Figure 4.3.7. The SE spectra collected from a spider silk "skin" with different surface inclination angle is shown in a). Two sets of SE spectra of spider silk "skin" and cross-section is compared in b) and c).

We collected the SE spectra of spider silk fiber based on our knowledge of its structure. First, I noticed the SE spectra overall shape changes drastically when the surface inclination angle with respect to the electron beam changes (figure 4.3.7 a)).

This is likely to be result of the detection efficiency of SEM system changing with surface inclination. On the other hand, tilting the angle of sample surface is equal to changing the molecule orientation of whole material together. There is literature reporting a change of SE yield when the orientation of a crystal changes[215]. The change of overall spectra shape here suggests the ratio between certain SE peaks may reflect the orientation of whole material system.

Nevertheless, the SE peaks below 5 eV remain repeatable regardless, as shown in figure 4.3.7. Second, the SE spectra of the silk "skin" yield a 3.8-4.0 eV peak, which is very small in spectra of silk cross-section (figure 4.3.7 b, c)). Since the silk cross-section contain both conformation of spidroin protein, this missing peak suggests the lack of a certain composition or conformation inside silk fiber compared with the "skin". Third, the cross-section spectra yield a 3.6 eV peak in some situations but silk "skin" spectra yield very little signal in this energy range in all samples. Since the spidroin2 is reported to be concentrated in the center region of silk fiber and do not exist at fiber edge, it can be assumed that this 3.6 eV peak can be related to the spidroin2 protein.

Overall, if the 3.6 eV peak is related to spidroin2, SEHI should yield contrast for fibril cores using this energy window. However, well defined SEHI image for fibril core has not been collected successfully. This is due to the signal in this energy window is very weak, leading to high-level noise in imaging. Thus the SE peaks on our spectra cannot be fully identified and will require future work on SEHI using fine peak structure in SE spectrum.

Now we can summarize the factors affecting SE spectra according to our experiments on different silk materials. There is still little work on complex polymer SE spectra carried out in SEM according to literature reports, however, the theoretical approach applied in Monte Carlo simulation can still provide information of such factors.

First, the SE spectra are formed by electrons scattered from every atom in the electron implantation path, thus the atom numbers and the material density obviously affect the SE spectra. Different composition or crystallinity lead to different spectra, and this is shown in the characterization of sericin/fibroin and crystalline/amorphous fibroin phase in silk materials.

Second, the scattering of electron in molecule materials is not only decided by atomic electron properties, but also the electron cloud of whole molecule. Simulation of electrons interacting with large molecular electron cloud is still not available but it is reasonable to assume such effect play a role in electron spectra formation. In terms of material systems, this means large molecules like proteins would produce different SE spectra when there is different conformation. This effect is observed in the characterization of different types of silk fibroin in natural and artificial silk materials.

Third, a noticeable factor in SE spectra formation is the orientation of molecules. The theoretical simulation shows when crystal structures orientation changes, the number of atom electrons encounters in interaction changes as well. Such effect produce shifting or other kind of feature in SE spectra. However, this is more

complicated for large molecules with long chains. For example, an electron pass through a long chain molecule in the longitudinal axis may encounter thousands of repeating unit, but if it pass through the cross-section there may be only one repeating unit. The existence of such effect appeared when we collect spectra on same sample with different tilting angle on spider silk.

Overall, composition, density/crystallinity, molecule conformation and molecule orientation are the main factors in the formation of SE spectra in our experiment. Further study of each factors may start on simpler materials to isolate changing factors in the future.
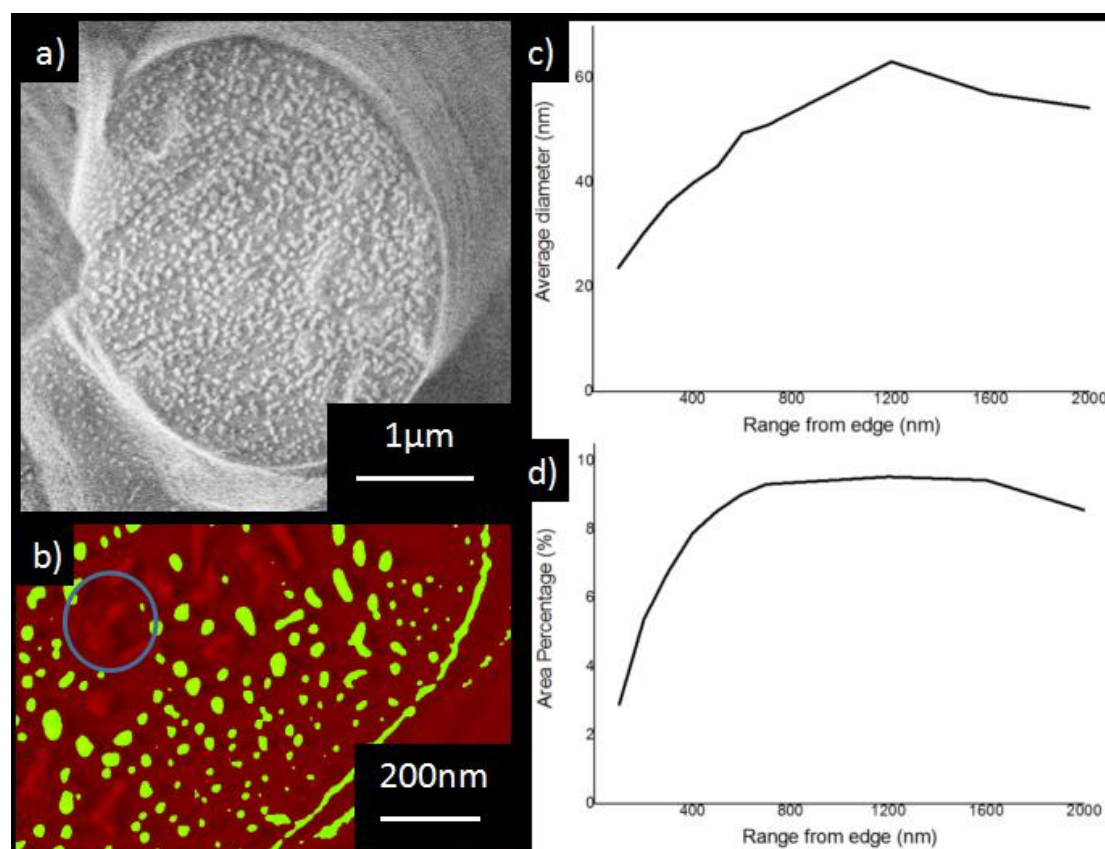

Figure 4.3.8. The fibril core distribution on the spider silk cross-section is shown in image a), note there are also large irregular shape objects on sample cross-section as highlighted in b). Those objects are not counted as fibril core. The diameter/fraction of fibril core changing with its range from fiber edge are plotted in c,d).

We noticed the nano-structures on the spider silk cross-section also show a size/fraction variation across the fiber diameter in figure 4.3.8 a), which is comparable to the silkworm silk fibers. However, there are also some large irregular shape objects on the cross-section surface. These object can be as large as 100nm and clearly are not fibril cores as shown in figure 4.3.8 b). Thus these object need to be excluded when characterizing the fibril core distribution. Using the same analysis methods in 4.2, we can measure the average size and area fraction of nano-structures in concentric rings corresponding to the chosen range to fiber edge.

Thus the nano-structure size/fraction variation can be plotted as shown in figure 4.3.8 c, d).

The diameter of nano-structure increase rapidly from 20nm to 50nm in first 800nm from edge, and it continues to increase to 60nm before dropping slightly in the fiber center. The fraction of nano-structure shows a similar trend, reaching a maximum of ~9% between 800-1600nm from edge before dropping in the fiber center. Such trend is very similar to the B. mori silkwom silk nano-fibrils, however the meaning of such trend is not the same. The nano-fibril in silkworm silk directly represents the crystallinity of the whole fiber, while the fibril core in spider silk is more amorphous. Although increasing fibril size also lead to large crystalline fibril shell, the local crystallinity in spider silk does not form a simple relationship with fibril core parameters. Overall, the fibril core variation shows a similar gland flow field to the one of silkworm silk mentioned in 4.2. But the change of trend in the fiber center suggests the flow field in the center of the silk gland is not an even one, which was assumed by literature in modelling[216].
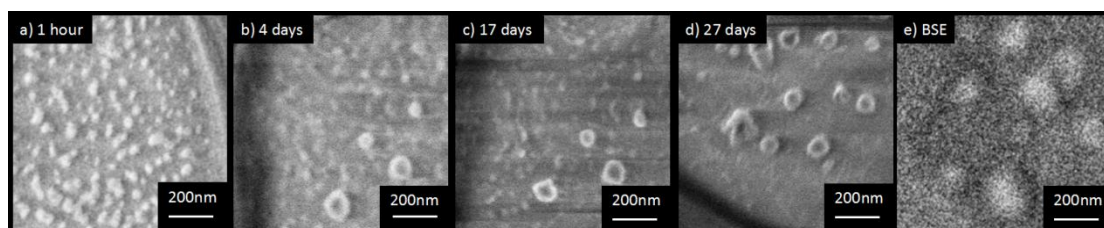

Figure 4.3.9. The image array a) to d) shows the change of a fiber cross-section from 1 hour to 27 days after cryo-snap. The BSE image e) is taken on the 27 days after the cryo-snap.

The irregular shape large objects on the fiber cross-section appears in most of cryo-snapped samples. Those objects grow rapidly in the first few days after sample preparation and slowly shrink and eventually fracture in the following time as shown in figure 4.3.9. These objects are not observed on the outside the silk fiber and thus are not simply a result of contamination. The spider silk is also known to be rather stable over a few years and the ageing is only reported for several year time scales[218]. Thus it can be speculated such objects are leeching out of fiber cross-section after the cryo-snap. Since those objects show a much stronger BSE signal than the silk they potentially contain heavier elements such as metals. As ice is formed on fiber cross-section in the cryo-snap process (since our sample is not transported in vacuum after snapping, detail of experimental see 3.2). The water can play a role in dissolving material such as salts in the fiber. The water can cause super contraction in spider silk, which will reduce the local orientation[219], and water will be absorbed into low crystallinity region[220]. When fiber structure is weakened by super contraction, those salts may reach cross-section surface through water. Thus such composition can precipitate in the first few days after the cryo-snap and form salt crystals on the fiber cross-section. However, the chemical characterization data of these objects and the their effect on the silk fiber is still required. Future work is
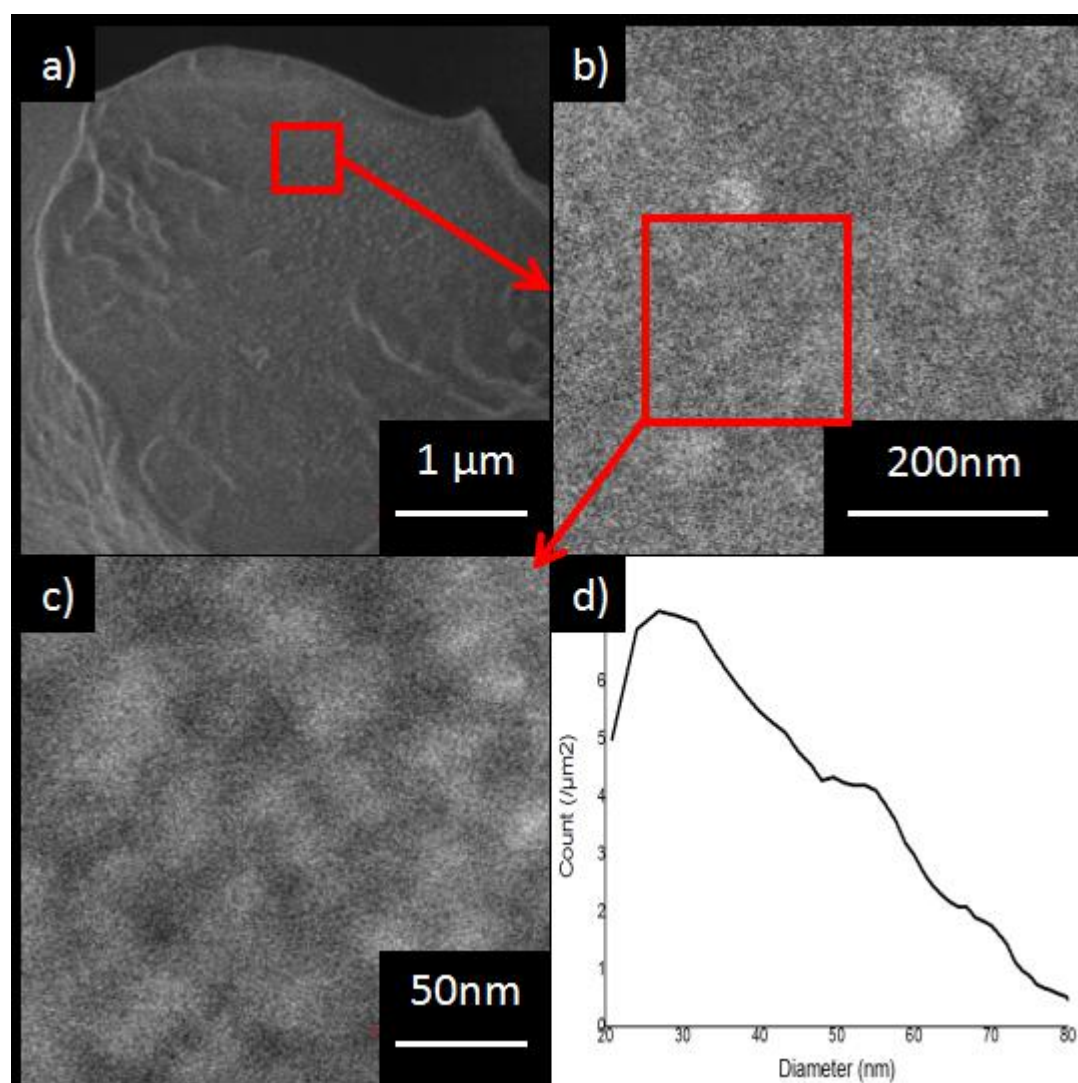
required to study the origin of those objects.

Figure 4.3.10. The image a) shows the normal fibril core size nano-structures on the silk fiber cross-section. The image a, b, c) shows a densely distributed nano-structure with diameter down to ~10nm besides the larger ~50nm diameter nano-structures. The size distribution of nano-objects on the fiber cross-section is shown in plot d).

As mentioned above in figure 4.3.6, I assumed all nano-structures ranging from 20-60nm diameter are silk fibril cores. However, not all the nano-structures can be simply described as fibril core. As shown in figure 4.3.10 a), fibril core sized nano-structures can be seen on the fiber cross-section. Additional smaller nano-objects can be noticed in the same area, which is shown in zoomed in view in figure 4.3.10 b, c), the zoomed in area is highlighted in lower magnification images. Those smaller objects are distributed in a very dense manner and the diameter is far smaller than the reported data. Their diameter can be down to ~10nm, which is close to the size of β-sheet crystals in the longitudinal axis[202]. These small nano-objects are challenging to image due to limit of the NOVA-SEM resolution and surface charging. But their large number can still be reflected in the nano-object size

123

distribution on fiber cross-section in plot figure 4.3.10 d). It is possible for those nano-structures being the nodes in the fishnet model of silk described in literature[44], or serving other structural roles. This will also require future work in sub-nanometer resolution characterization of spider silk fibers.

5. Conclusion

The electron-solid interaction theoretical interpretation suggested the possibility of exploiting the electron spectrum in SEM techniques. This is made possible by the recent development of BSE and SE detection systems. Using such detection systems, the BSE and SE signal in SEM was optimized for the purpose of nano-resolution chemical characterization of bio-composites in this project.

The BSE signal was separated depending on its angular distribution, which is related to the origin of different BSE signals. This angular distribution was simulated through Monte Carlo computing program with calculated input material parameters, and transferred into microscope parameters. The SEM settings were adjusted accordingly to optimize the chemical contrast between given material phases. This is validated by comparing calculated contrast data with experimental contrast data. The phase separation in a series of PNIPAM composite materials were analyzed using the optimized SEM settings.

For a more complex natural silk fiber material, multiple phases with very similar composition and density exist in nano-structures. The exact composition of each phase are not clearly defined due to complex protein behavior and direct theoretical interpretation of such complex system is not available. Thus the phases were identified by combining the BSE and SE filtering technique. The well-studied high-order crystalline fibrils were identified through the BSE technique. The SE spectra was measured for different nano-phases and compared with each other, the major spectra difference for ordered and disordered phases yielded the SE energy window for protein order-level. Using such specific energy windows, the hyperspectral SE image provided the phase mapping of silk fiber based on the local crystallinity. The characterization data of local crystallinity across the fiber cross-section was summarized and the organization of nano-repeating unit in silk fiber was revealed.

The SE spectra measured on silk fiber yielded a very complex peak structure. The SE spectra of artificial silk films was measured in order to validate and compare with such peak structures. The spectra and the hyperspectral imaging using artificial silk material yielded repeatable result comparing to the natural fibers. Hence the peak fine structure in the SE spectra low energy region is repeatable for same protein even in different material systems. This low energy region below 6eV was compared to UV spectroscopy, and some of the fine SE peaks appears in the similar energy zone to specific UV energy band. However, there are still gaps to be filled between electron spectra and UV spectra: First the SE peaks are much sharper compared to UV bands and it is hard to decide if they belong to a same energy region. Second, we only have some level of agreement between two techniques using limited sets of experimental data. Since the physics behind transferring photon absorption electron absorption (for example, different effect of molecule orientation on photon and electron) is not considered in detail, going directly to conclusion using experimental data may lead to

over simplification and misinterpretation. Hence, for now the conclusion can be made is that such fine structure in SE spectra shows a certain level of relationship to certain proteins and protein conformations. This still requires more systematic study in the future but it reveals the potential for further SE spectra based imaging application in complex system protein mapping and identification.

The SE filtering technique was further applied on spider silk fibers. Different scale nano-structures range from 10nm to 70nm was observed on spider silk cross-section. The distribution of the fibril core on fiber cross-section showed similar trend compared to the nano-fibril in silkworm ones. The scale and fraction of the fibril core increase rapidly in the first micrometer inside fiber edge, which is predicted by the model of silk flow field in the gland. But these parameters drop slightly when approaching the fiber center, suggesting the flow field in the gland center may not be completely uniform as supposed in theoretical models. However due to the low signal to noise ratio, the hyperspectral imaging of nano-structures require more definitive result. Further high-resolution hyperspectral imaging along with the study of possible water soluble material contributing to observed ageing effect will require future work in improved SEM systems (probably cryo-SEM).

In summary, we have applied the angle selective BSE and energy filtered SE technique and characterized the nano PNIPAM phase in PEGDA matrix and the nano structure with different level of crystallinity in natural silk fiber and artificial silk. Such nano-composite systems matched our project aim: chemical characterization of nano-scale, beam sensitive, varied local composition in polymer system. The relationship between fine structure observed in SE spectra and molecule conformation/orientation was explored. Such relationship was suggested by the imaging of different silk samples and related UV absorption data in literature. The further understanding of fine structures in SE spectra would require more systematic research combined with theoretical guidance in the future.

Acknowledgment

I would like to thank the following people and groups for their input:

References

[1]Siegel, R. W., Chang, S. K., Ash, B. J., Stone, J. A. P. M., Ajayan, P. M., Doremus, R. W., & Schadler, L. S. (2001). Mechanical behavior of polymer and ceramic matrix nanocomposites. *Scripta Materialia*, *44*(8), 2061-2064.

[2] Jordan, J., Jacob, K. I., Tannenbaum, R., Sharaf, M. A., & Jasiuk, I. (2005). Experimental trends in polymer nanocomposites—a review. *Materials science and engineering: A*, *393*(1), 1-11.

[3] Shia, D., Hui, C. Y., Burnside, S. D., & Giannelis, E. P. (1998). An interface model for the prediction of Young's modulus of layered silicate-elastomer nanocomposites. *Polymer Composites*, *19*(5), 608-617.

[4] Cho, J., Joshi, M. S., & Sun, C. T. (2006). Effect of inclusion size on mechanical properties of polymeric composites with micro and nano particles. *Composites Science and Technology*, *66*(13), 1941-1952.

[5] Smith, G. D., Bedrov, D., Li, L., & Byutner, O. (2002). A molecular dynamics simulation study of the viscoelastic properties of polymer nanocomposites. *The Journal of chemical physics*, *117*(20), 9478-9489..

[6] Koo, C. M., Kim, M. J., Choi, M. H., Kim, S. O., & Chung, I. J. (2003). Mechanical and rheological properties of the maleated polypropylene–layered silicate nanocomposites with different morphology. *Journal of applied polymer science*, *88*(6), 1526-1535.

[7] Chan, C. M., Wu, J., Li, J. X., & Cheung, Y. K. (2002). Polypropylene/calcium carbonate nanocomposites. *polymer*, *43*(10), 2981-2992.

[8] Yang, F., Ou, Y., & Yu, Z. (1998). Polyamide 6/silica nanocomposites prepared by in situ polymerization. *Journal of Applied Polymer Science*, *69*(2), 355-361.

[9]Cheung, H. Y., Lau, K. T., Lu, T. P., & Hui, D. (2007). A critical review on polymer-based bio-engineered materials for scaffold development. *Composites Part B: Engineering*, *38*(3), 291-300.

[10] Oosterhout, S. D., Wienk, M. M., Van Bavel, S. S., Thiedmann, R., Koster, L. J. A., Gilot, J., ... & Janssen, R. A. (2009). The effect of three-dimensional morphology on the efficiency of hybrid polymer solar cells. *Nature materials*, *8*(10), 818.

[11] Slivka, M. A., Leatherbury, N. C., Kieswetter, K., & Niederauer, G. G. (2001). Porous, resorbable, fiber-reinforced scaffolds tailored for articular cartilage repair. *Tissue engineering*, *7*(6), 767-780.

[12]Lee, S. M., Cho, D., Park, W. H., Lee, S. G., Han, S. O., & Drzal, L. T. (2005). Novel silk/poly (butylene succinate) biocomposites: the effect of short fibre content on their mechanical and thermal properties. *Composites Science and Technology*, *65*(3), 647-657.

[13] Zein, I., Hutmacher, D. W., Tan, K. C., & Teoh, S. H. (2002). Fused deposition modeling of novel scaffold architectures for tissue engineering applications. *Biomaterials*, *23*(4), 1169-1185.

[14] Olson, D. C., Piris, J., Collins, R. T., Shaheen, S. E., & Ginley, D. S. (2006). Hybrid photovoltaic devices of polymer and ZnO nanofiber composites. *Thin solid films*, *496*(1), 26-29.

[15] Gautieri, A., Vesentini, S., Redaelli, A., & Buehler, M. J. (2011). Hierarchical structure and nanomechanics of collagen microfibrils from the atomistic scale up. *Nano letters*, *11*(2), 757-766.

[16] Martínez-Sanz, M., Gidley, M. J., & Gilbert, E. P. (2015). Application of X-ray and neutron small angle scattering techniques to study the hierarchical structure of plant cell walls: a review. *Carbohydrate polymers*, *125*, 120-134.

[17] Bhattacharya, D., Germinario, L. T., & Winter, W. T. (2008). Isolation, preparation and characterization of cellulose microfibers obtained from bagasse. *Carbohydrate Polymers*, *73*(3), 371-377.

[18] Riekel, C., Burghammer, M., Dane, T. G., Ferrero, C., & Rosenthal, M. (2016). Nanoscale Structural Features in Major Ampullate Spider Silk. *Biomacromolecules*, *18*(1), 231-241.

[19] Efremov, E. V., Ariese, F., & Gooijer, C. (2008). Achievements in resonance Raman spectroscopy: Review of a technique with a distinct analytical chemistry potential. *analytica chimica acta*, *606*(2), 119-134.

[20] Goormaghtigh, E., Cabiaux, V., & RUYSSCHAERT, J. M. (1990). Secondary structure and dosage of soluble and membrane proteins by attenuated total reflection Fourier-transform infrared spectroscopy on hydrated films. *The FEBS Journal*, *193*(2), 409-420.

[21] Taddei, P., & Monti, P. (2005). Vibrational infrared conformational studies of model peptides representing the semicrystalline domains of Bombyx mori silk fibroin. *Biopolymers*, *78*(5), 249-258.

[22] Kauppinen, J. K., Moffatt, D. J., Mantsch, H. H., & Cameron, D. G. (1981). Fourier self-deconvolution: a method for resolving intrinsically overlapped bands. *Applied Spectroscopy*, *35*(3), 271-276.

[23] Reinstädler, D., Fabian, H., Backmann, J., & Naumann, D. (1996). Refolding of thermally and urea-denatured ribonuclease A monitored by time-resolved FTIR spectroscopy. *Biochemistry*, *35*(49), 15822-15830.

[24]Chen, X., Knight, D. P., Shao, Z., & Vollrath, F. (2002). Conformation transition in silk protein films monitored by time-resolved Fourier transform infrared spectroscopy: effect of potassium ions on Nephila spidroin films. *Biochemistry*, *41*(50), 14944-14950.

[25] Nafie, L. A. (2016). Recent advances in linear and non-linear Raman spectroscopy. Part X. *Journal of Raman Spectroscopy*.

[26] Martel, A., Burghammer, M., Davies, R. J., Di Cola, E., Vendrely, C., & Riekel, C. (2008). Silk fiber assembly studied by synchrotron radiation SAXS/WAXS and Raman spectroscopy. *Journal of the American Chemical Society*, *130*(50), 17070-17074..

[27] Lekprasert, B., Korolkov, V., Falamas, A., Chis, V., Roberts, C. J., Tendler, S. J., & Notingher, I. (2012). Investigations of the supramolecular structure of individual diphenylalanine nano-and microtubes by polarized Raman microspectroscopy. *Biomacromolecules*, *13*(7), 2181-2187.

[28] Colomban, P. (2012). Understanding the nano-and macromechanical behaviour, the failure and fatigue mechanisms of advanced and natural polymer fibres by Raman/IR microspectrometry. *Advances in natural sciences: nanoscience and nanotechnology*, *4*(1), 013001.

[29] Hu, X., Kaplan, D., & Cebe, P. (2006). Determining beta-sheet crystallinity in fibrous proteins by thermal analysis and infrared spectroscopy. *Macromolecules*, *39*(18), 6161-6170.

[30] Mastel, S., Govyadinov, A. A., de Oliveira, T. V., Amenabar, I., & Hillenbrand, R. (2015). Nanoscale-resolved chemical identification of thin organic films using infrared near-field spectroscopy and standard Fourier transform infrared references. *Applied Physics Letters*, *106*(2), 023113.

[31] Huth, F., Govyadinov, A., Amarie, S., Nuansing, W., Keilmann, F., & Hillenbrand, R. (2012). Nano-FTIR absorption spectroscopy of molecular fingerprints at 20 nm spatial resolution. *Nano letters*, *12*(8), 3973-3978.

[32] Qin, N., Zhang, S., Jiang, J., Corder, S. G., Qian, Z., Zhou, Z., ... & Shi, Z. (2016). Nanoscale probing of electron-regulated structural transitions in silk proteins by near-field IR imaging and nano-spectroscopy. *Nature communications*, *7*.

[33] Binnig, G., Quate, C. F., & Gerber, C. (1986). Atomic force microscope. *Physical review letters*, *56*(9), 930.

[34] Butt, H. J., Cappella, B., & Kappl, M. (2005). Force measurements with the atomic force microscope: Technique, interpretation and applications. *Surface science reports*, *59*(1), 1-152.

[35]Jalili, N., & Laxminarayana, K. (2004). A review of atomic force microscopy imaging systems: application to molecular metrology and biological sciences. *Mechatronics*, *14*(8), 907-945.

[36] Raab, A., Han, W., Badt, D., Smith-Gill, S. J., Lindsay, S. M., Schindler, H., & Hinterdorfer, P. (1999). Antibody recognition imaging by force microscopy. *Nature biotechnology*, *17*(9).

[37] Niedermann, P., Hänni, W., Blanc, N., Christoph, R., & Burger, J. (1996). Chemical vapor deposition diamond for tips in nanoprobe experiments. *Journal of Vacuum Science & Technology A: Vacuum, Surfaces, and Films*, *14*(3), 1233-1236.

[38] Miyahara, K., Nagashima, N., Ohmura, T., & Matsuoka, S. (1999). Evaluation of mechanical properties in nanometer scale using AFM-based nanoindentation tester. *Nanostructured Materials*, *12*(5-8), 1049-1052.

[39] Briscoe, B. J., Fiori, L., & Pelillo, E. (1998). Nano-indentation of polymeric surfaces. *Journal of Physics D: Applied Physics*, *31*(19), 2395.

[40] Brown, C. P., Rosei, F., Traversa, E., & Licoccia, S. (2011). Spider silk as a load bearing biomaterial: tailoring mechanical properties via structural modifications. *Nanoscale*, *3*(3), 870-876.

[41] Geisler, M., Pirzer, T., Ackerschott, C., Lud, S., Garrido, J., Scheibel, T., & Hugel, T. (2008). Hydrophobic and Hofmeister effects on the adhesion of spider silk proteins onto solid substrates: an AFM-based single-molecule study. *Langmuir*, *24*(4), 1350-1355.

[42] Zhang, W., Xu, Q., Zou, S., Li, H., Xu, W., Zhang, X., ... & Gaub, H. E. (2000). Single-molecule force spectroscopy on Bombyx mori silk fibroin by atomic force microscopy. *Langmuir*, *16*(9), 4305-4308.

[43] Shang, S., Zhu, L., & Fan, J. (2013). Intermolecular interactions between natural polysaccharides and silk fibroin protein. *Carbohydrate polymers*, *93*(2), 561-573.

[44] Liu, R., Deng, Q., Yang, Z., Yang, D., Han, M. Y., & Liu, X. Y. (2016). "Nano-Fishnet" Structure Making Silk Fibers Tougher. *Advanced Functional Materials*, *26*(30), 5534-5541.

[45] Hansma, H. G., Kim, K. J., Laney, D. E., Garcia, R. A., Argaman, M., Allen, M. J., & Parsons, S. M. (1997). Properties of biomolecules measured from atomic force microscope images: a review. *Journal of structural biology*, *119*(2), 99-108.

[46] Yan, H., Park, S. H., Finkelstein, G., Reif, J. H., & LaBean, T. H. (2003). DNA-templated self-assembly of protein arrays and highly conductive nanowires. *science*, *301*(5641), 1882-1884.

[47] Schäfer, A., Vehoff, T., Glišović, A., & Salditt, T. (2008). Spider silk softening by water uptake: an AFM study. *European Biophysics Journal*, *37*(2), 197-204.

[48] Scheer, E., Agraït, N., Cuevas, J. C., & Yeyati, A. L. (1998). The signature of chemical valence in the electrical conduction through a single-atom contact. *Nature*, *394*(6689), 154.

[49] Lloyd, G. E. (1987). Atomic number and crystallographic contrast images with the SEM: a review of backscattered electron techniques. *Mineralogical Magazine*, *51*(359), 3-19.

[50] Kanaya, K., & Okayama, S. (1972). Penetration and energy-loss theory of electrons in solid targets. *Journal of Physics D: Applied Physics*, *5*(1), 43.

Kanaya, K., & Okayama, S. (1972). Penetration and energy-loss theory of electrons in solid targets. *Journal of Physics D: Applied Physics*, *5*(1), 43.

[51] Reimer, L. (2000). Scanning electron microscopy: physics of image formation and microanalysis.

[52] Yubero, F., & Tougaard, S. (1992). Model for quantitative analysis of reflection-electron-energy-loss spectra. *Physical Review B*, *46*(4), 2486.

[53] Wolff, P. A. (1954). Theory of secondary electron cascade in metals. *Physical Review*, *95*(1), 56.

[54] Raether, H. (2006). *Excitation of plasmons and interband transitions by electrons* (Vol. 88). Springer.

[55] Ding, Z. J., & Shimizu, R. (1996). A Monte Carlo modeling of electron interaction with solids including cascade secondary electron production. *Scanning*, *18*(2), 92-113.

[56] Egerton, R. F. (2011). *Electron energy-loss spectroscopy in the electron microscope*. Springer Science & Business Media.

[57] Wagner, C. D., Davis, L. E., & Riggs, W. M. (1980). The energy dependence of the electron mean free path. *Surface and Interface Analysis*, *2*(2), 53-55.

[58] Freund, R. S., Wetzel, R. C., Shul, R. J., & Hayes, T. R. (1990). Cross-section measurements for electron-impact ionization of atoms. *Physical Review A*, *41*(7), 3575.

[59]Lucas, A. A., Henrard, L., & Lambin, P. (1994). Computation of the ultraviolet absorption and electron inelastic scattering cross section of multishell fullerenes. *Physical Review B*, *49*(4), 2888.

[60] Cumpson, P. J. (2001). Estimation of inelastic mean free paths for polymers and other organic materials: use of quantitative structure–property relationships. *Surface and interface analysis*, *31*(1), 23-34.

[61] Thwaites, D. I. (1983). Bragg's rule of stopping power additivity: A compilation and summary of results. *Radiation Research*, *95*(3), 495-518.

[62] Powell, C. J., & Jablonski, A. (1999). NIST Electron Inelastic-Mean-Free-Path Database 71, Version 1.0. *Nat'l Std. Ref. Data Series (NIST NSRDS)-*.

[63] Tanaka, T., Montanari, G. C., & Mulhaupt, R. (2004). Polymer nanocomposites as dielectrics and electrical insulation-perspectives for processing technologies, material characterization and future applications. *IEEE transactions on Dielectrics and Electrical Insulation*, *11*(5), 763-784.

[64] Chantler, C. T., & Bourke, J. D. (2014). Electron inelastic mean free path theory and density functional theory resolving discrepancies for low-energy electrons in copper. *The Journal of Physical Chemistry A*, *118*(5), 909-914.

[65] French, R. H., Müllejans, H., & Jones, D. J. (1998). Optical Properties of Aluminum Oxide: Determined from Vacuum Ultraviolet and Electron Energy-Loss Spectroscopies. *Journal of the American Ceramic Society*, *81*(10), 2549-2557.

[66] Tanuma, S., Powell, C. J., & Penn, D. R. (1991). Calculations of electorn inelastic mean free paths. II. Data for 27 elements over the 50–2000 eV range. *Surface and Interface Analysis*, *17*(13), 911-926.

[67] Dapor, M. (2004). An analytical approximation of the differential elastic scattering cross-section for electrons in selected oxides. *Physics Letters A*, *333*(5), 457-467.

[68] Ono, S., & Kanaya, K. (1979). The energy dependence of secondary emission based on the range-energy retardation power formula. *Journal of Physics D: Applied Physics*, *12*(4), 619.

[69] Chung, M. S., & Everhart, T. E. (1974). Simple calculation of energy distribution of low-energy secondary electrons emitted from metals under electron bombardment. *Journal of Applied Physics*, *45*(2), 707-709.

[70] Schwarz, S. A. (1990). Application of a semi-empirical sputtering model to secondary electron emission. *Journal of Applied Physics*, *68*(5), 2382-2391.

[71] Kieft, E., & Bosch, E. (2008). Refinement of Monte Carlo simulations of electron–specimen interaction in low-voltage SEM. *Journal of Physics D: Applied Physics*, *41*(21), 215310.

[72] Shimizu, R., & Ze-Jun, D. (1992). Monte Carlo modelling of electron-solid interactions. *Reports on Progress in Physics*, *55*(4), 487.

[73] Ibach, H., & Mills, D. L. (2013). *Electron energy loss spectroscopy and surface vibrations*. Academic press.

[74] Dapor, M. (2004). An analytical approximation of the differential elastic scattering cross-section for electrons in selected oxides. *Physics Letters A*, *333*(5), 457-467.

[75] Dapor, M. (2006). Energy loss spectra of low primary energy (E 0⩽ 1keV) electrons backscattered by silicon dioxide. *Surface science*, *600*(20), 4728-4734.

[76] Kwei, C. M., Wang, C. Y., & Tung, C. J. (1998). Surface excitation parameters of low-energy electrons crossing solid surfaces. *Surface and interface analysis*, *26*(9), 682-688.

[77] Dapor, M. (2011). Secondary electron emission yield calculation performed using two different Monte Carlo strategies. *Nuclear Instruments and Methods in Physics Research Section B: Beam Interactions with Materials and Atoms*, *269*(14), 1668-1671.

[78] Taioli, S., Simonucci, S., Calliari, L., & Dapor, M. (2010). Electron spectroscopies and inelastic processes in nanoclusters and solids: Theory and experiment. *Physics Reports*, *493*(5), 237-319.

[79] Ding, Z. J., & Shimizu, R. (1996). A Monte Carlo modeling of electron interaction with solids including cascade secondary electron production. *Scanning*, *18*(2), 92-113.

[80] Dapor, M. (1992). Monte Carlo simulation of backscattered electrons and energy from thick targets and surface films. *Physical Review B*, *46*(2), 618.

[81] Ding, Z. J., & Li, H. M. (2005). Application of Monte Carlo simulation to SEM image contrast of complex structures. *Surface and interface analysis*, *37*(11), 912-918.

[82] Demers, H., Brodusch, N., Woo, P., & Gauvin, R. (2015). Origins and Contrast of the Electron Signals at Low Accelerating Voltage and with Energy-Filtering in the FE-SEM for High Resolution Imaging. *Microscopy and Microanalysis*, *21*, 705.

[83] Schreiber, E., & Fitting, H. J. (2002). Monte Carlo simulation of secondary electron emission from the insulator SiO 2. *Journal of Electron Spectroscopy and Related Phenomena*, *124*(1), 25-37.

[84] Halbritter, J. (1982). On conditioning: Reduction of secondary-and rf-field emission by electron, photon, or helium impact. *Journal of Applied Physics*, *53*(9), 6475-6478.

[85] Hessel, R., & Gross, B. (1992). Escape depth of secondary electrons from electron-irradiated polymers. *IEEE transactions on electrical insulation*, *27*(4), 831-834.

[86] Cazaux, J. (2005). A new model of dependence of secondary electron emission yield on primary electron energy for application to polymers. *Journal of Physics D: Applied Physics*, *38*(14), 2433.

[87] Peters, K. R. (1981). Conditions required for high quality high magnification images in secondary electron-I scanning electron microscopy. *Scanning electron microscopy*, (Pt 4), 1359-1372.

[88] Baumann, W., & Reimer, L. (1981). Comparison of the noise of different electron detection systems using a scintillator-photomultiplier combination. *Scanning*, *4*(3), 141-151.

[89] Joy, D. C. (1984). Beam interactions, contrast and resolution in the SEM. *Journal of Microscopy*, *136*(2), 241-258.

[90] Kaminskyj, S. G., & Dahms, T. E. (2008). High spatial resolution surface imaging and analysis of fungal cells using SEM and AFM. *Micron*, *39*(4), 349-361.

[91] Koshikawa, T., & Shimizu, R. (1974). A Monte Carlo calculation of low-energy secondary electron emission from metals. *Journal of Physics D: Applied Physics*, *7*(9), 1303.

[92] Lin, Y., & Joy, D. C. (2005). A new examination of secondary electron yield data. *Surface and Interface Analysis*, *37*(11), 895-900.

[93] Seiler, H. (1983). Secondary electron emission in the scanning electron microscope. *Journal of Applied Physics*, *54*(11), R1-R18.

[94] Cazaux, J. (2005). A new model of dependence of secondary electron emission yield on primary electron energy for application to polymers. *Journal of Physics D: Applied Physics*, *38*(14), 2433.

[95] Ono, S., & Kanaya, K. (1979). The energy dependence of secondary emission based on the range-energy retardation power formula. *Journal of Physics D: Applied Physics*, *12*(4), 619.

[96] Thieberger, P., Hanson, A. L., Steski, D. B., Zajic, V., Zhang, S. Y., & Ludewig, H. (2000). Secondary-electron yields and their dependence on the angle of incidence on stainless-steel surfaces for three energetic ion beams. *Physical Review A*, *61*(4), 042901.

[97] Yong, Y. C., Thong, J. T. L., & Phang, J. C. H. (1998). Determination of secondary electron yield from insulators due to a low-kV electron beam. *Journal of Applied Physics*, *84*(8), 4543-4548.

[98] Seiler, H. (1967). Some problems of secondary electron emission. *Z. angew. Phys*, *22*, 249-263.

[99] Dionne, G. F. (1975). Origin of secondary-electron-emission yield-curve parameters. *Journal of Applied Physics*, *46*(8), 3347-3351.

[100] Schwab, A., Bretschneider, J., Buque, C., Blochwitz, C., & Holste, C. (1996). Application of electron channelling contrast to the investigation of strain localization effects in cyclically deformed fcc crystals. *Philosophical magazine letters*, *74*(6), 449-454.

[101] Pfeiffer, H. C. (1982). CONTACTLESS ELECTRICAL TESTING WITH MULTIPLE ELECTRON-BEAMS. *Scanning Electron Microscopy*, 581-589.

[102] Menzel, E., & Kubalek, E. (1981). Electron beam test techniques for integrated circuits. *Scanning Electron Microsc.*, (1), 305-322.

[103] Aristov, V. V., Kokhanchik, L. S., & Voronovskii, Y. I. (1984). Voltage contrast of ferroelectric domains of lithium niobate in SEM. *physica status solidi (a)*, *86*(1), 133-141.

[104] Joy, D. (1985). Low Voltage SEM. *Journal of Microscopy*, *140*(3), 282-282.

[105] Joy, D. C. (1989). Control of charging in low-voltage SEM. *Scanning*, *11*(1), 1-4.

[106] Boyes, E. D. (1998). High-Resolution and Low-Voltage SEM Imaging and Chemical Microanalysis. *Advanced Materials*, *10*(15), 1277-1280.

[107] Butler, J. H., Joy, D. C., Bradley, G. F., & Krause, S. J. (1995). Low-voltage scanning electron microscopy of polymers. *Polymer*, *36*(9), 1781-1790.

[108] Hovington, P., Drouin, D., & Gauvin, R. (1997). CASINO: A new Monte Carlo code in C language for electron beam interaction—Part I: Description of the program. *Scanning*, *19*(1), 1-14.

[109] Egerton, R. F., Li, P., & Malac, M. (2004). Radiation damage in the TEM and SEM. *Micron*, *35*(6), 399-409.

[110] Henderson, R., & Glaeser, R. M. (1985). Quantitative analysis of image contrast in electron micrographs of beam-sensitive crystals. *Ultramicroscopy*, *16*(2), 139-150.

[111] Donald, A. M. (2003). The use of environmental scanning electron microscopy for imaging wet and insulating materials. *Nature materials*, *2*(8), 511.

[112]Cameron, N. R., Sherrington, D. C., Albiston, L., & Gregory, D. P. (1996). Study of the formation of the open-cellular morphology of poly (styrene/divinylbenzene) polyHIPE materials by cryo-SEM. *Colloid & Polymer Science*, *274*(6), 592-595.

[113] Win, K. Y., & Feng, S. S. (2005). Effects of particle size and surface coating on cellular uptake of polymeric nanoparticles for oral delivery of anticancer drugs. *Biomaterials*, *26*(15), 2713-2722.

[114] Apkarian, R. P., Wright, E. R., Seredyuk, V. A., Eustis, S., Lyon, L. A., Conticello, V. P., & Menger, F. M. (2003). In-lens cryo-high resolution scanning electron microscopy: methodologies for molecular imaging of self-assembled organic hydrogels. *Microscopy and Microanalysis*, *9*(4), 286-295.

[115] Henderson, R. (1990). Cryo-protection of protein crystals against radiation damage in electron and X-ray diffraction. *Proceedings: Biological Sciences*, 6-8.

[116] Ueno, N., Seki, K., Sugita, K., & Inokuchi, H. (1991). Nature of the temperature dependence of conduction bands in polyethylene. *Physical Review B*, *43*(3), 2384.

[117] Nagoshi, M., Aoyama, T., & Sato, K. (2013). Extraction of topographic and material contrasts on surfaces from SEM images obtained by energy filtering detection with low-energy primary electrons. *Ultramicroscopy*, *124*, 20-25.

[118] Rasch, R., Stricher, A., & Truss, R. W. (2014). Energy filtered low voltage "in lens detector" SEM and XPS of natural fiber surfaces. *Journal of Applied Polymer Science*, *131*(9).

[119] de Abajo, F. G., & Howie, A. (1998). Relativistic electron energy loss and electron-induced photon emission in inhomogeneous dielectrics. *Physical Review Letters*, *80*(23), 5180.

[120] Cohen, M. R., & Merrill, R. P. (1990). Adsorption of pyridine on Ni (111): A high-resolution electron energy loss spectroscopy, angular-resolved UV photoemission, and x-ray photoelectron spectroscopy study. *Langmuir;(USA)*, *6*(7).

[121] Ueno, N., Sugita, K., & Kiyono, S. (1981). Change of secondary electron emission spectra of n-C44H90 due to crystal-melt phase transition. *Chemical Physics Letters*, *82*(2), 296-300.

[122] Bruining, H. (2013). *Die sekundär-elektronen-emission fester körper* (Vol. 5). Springer-Verlag.

[123] Modinos, A. (1984). Secondary electron emission spectroscopy. In *Field, Thermionic, and Secondary Electron Emission Spectroscopy* (pp. 327-345). Springer US.

[124] Sakai, Y., Yamada, T., Suzuki, T., Sato, T., Itoh, H., & Ichinokawa, T. (1998). Contrast mechanisms in scanning ion microscope imaging for metals. *Applied physics letters*, *73*(5), 611-613.

[125] Joy, D. C., Prasad, M. S., & Meyer, H. M. (2004). Experimental secondary electron spectra under SEM conditions. *Journal of microscopy*, *215*(1), 77-85.

[126] Tsurumi, D., Hamada, K., & Kawasaki, Y. (2010). Energy-filtered imaging in a scanning electron microscope for dopant contrast in InP. *Journal of electron microscopy*, *59*(S1), S183-S187.

[127] Agemura, T., Iwai, H., & Sekiguchi, T. (2017). Development of fountain detectors for spectroscopy of secondary electron in SEM. *physica status solidi (c)*.

[128] Schönjahn, C., Humphreys, C. J., & Glick, M. (2002). Energy filtered imaging in a FEG-SEM for enhanced dopant contrast. *Microscopy and Microanalysis*, *8*(S02), 718-719.

[129] Young, R., Bosch, E., Uncovsky, M., & Tuma, L. (2009). Low-energy secondary electron filtering with immersion lens SEM. *Microscopy and Microanalysis*, *15*(S2), 222.

[130] Kazemian, P., Mentink, S. A. M., Rodenburg, C., & Humphreys, C. J. (2007). Quantitative secondary electron energy filtering in a scanning electron microscope and its applications. *Ultramicroscopy*, *107*(2), 140-150.

[131] Rodenburg, C., Jepson, M. A. E., Inkson, B. J., Bosch, E. G. T., & Humphreys, C. J. (2010). Energy filtered scanning electron microscopy: applications to characterisation of semiconductors. In *Journal of Physics: Conference Series* (Vol. 241, No. 1, p. 012074). IOP Publishing.

[132] Dapor, M., Inkson, B. J., Rodenburg, C., & Rodenburg, J. M. (2008). A comprehensive Monte Carlo calculation of dopant contrast in secondary-electron imaging. *EPL (Europhysics Letters)*, *82*(3), 30006.

[133] Rodenburg, C., Jepson, M. A. E., Bosch, E. G. T., & Dapor, M. (2010). Energy selective scanning electron microscopy to reduce the effect of contamination layers on scanning electron microscope dopant mapping. *Ultramicroscopy*, *110*(9), 1185-1191.

[134] Masters, R. C., Pearson, A. J., Glen, T. S., Sasam, F. C., Li, L., Dapor, M., ... & Rodenburg, C. (2015). Sub-nanometre resolution imaging of polymer-fullerene photovoltaic blends using energy-filtered scanning electron microscopy. *Nature communications*, *6*.

[135] Murata, K. (1974). Spatial distribution of backscattered electrons in the scanning electron microscope and electron microprobe. *Journal of Applied Physics*, *45*(9), 4110-4117.

[136] Egerton, R. F. (2011). *Electron energy-loss spectroscopy in the electron microscope*. Springer Science & Business Media.

[137] Kim, K. W., & Jaksch, H. (2009). Compositional contrast of uncoated fungal spores and stained section-face by low-loss backscattered electron imaging. *Micron*, *40*(7), 724-729.

[138] Hermann, R., Walther, P., & Müller, M. (1996). Immunogold labeling in scanning electron microscopy. *Histochemistry and cell biology*, *106*(1), 31-39.

[139] Niedrig, H., & Rau, E. I. (1998). Information depth and spatial resolution in BSE microtomography in SEM. *Nuclear Instruments and Methods in Physics Research Section B: Beam Interactions with Materials and Atoms*, *142*(4), 523-534.

[140] Luo, T., & Khursheed, A. (2007). Imaging with surface sensitive backscattered electrons. *Journal of Vacuum Science & Technology B: Microelectronics and Nanometer Structures Processing, Measurement, and Phenomena*, *25*(6), 2017-2019.

[141] Merli, P. G., Morandi, V., & Corticelli, F. (2003). Backscattered electron imaging and scanning transmission electron microscopy imaging of multi-layers. *Ultramicroscopy*, *94*(2), 89-98.

[142] Lloyd, G. E. (1987). Atomic number and crystallographic contrast images with the SEM: a review of backscattered electron techniques. *Mineralogical Magazine*, *51*(359), 3-19.

[143] Wells, O. C. (1986). Low-loss electron images of uncoated photoresist in the scanning electron microscope. *Applied physics letters*, *49*(13), 764-766.

[144] Marini, A., Del Sole, R., & Rubio, A. (2003). Bound excitons in time-dependent density-functional theory: Optical and energy-loss spectra. *Physical review letters*, *91*(25), 256402.

[145] Reimer, L. (1993). *Image formation in low-voltage scanning electron microscopy* (Vol. 12). SPIE Press.

[146] Lloyd, G. E. (1987). Atomic number and crystallographic contrast images with the SEM: a review of backscattered electron techniques. *Mineralogical Magazine*, *51*(359), 3-19.

[147] Niedrig, H., & Rau, E. I. (1998). Information depth and spatial resolution in BSE microtomography in SEM. *Nuclear Instruments and Methods in Physics Research Section B: Beam Interactions with Materials and Atoms*, *142*(4), 523-534.

[148] Rau, E., Hoffmeister, H., Sennov, R., & Kohl, H. (2002). Comparison of experimental and Monte Carlo simulated BSE spectra of multilayered structures andin-depth'measurements in a SEM. *Journal of Physics D: Applied Physics*, *35*(12), 1433.

[149] Seiter, J., Müller, E., Blank, H., Gehrke, H., Marko, D., & Gerthsen, D. (2014). Backscattered electron SEM imaging of cells and determination of the information depth. *Journal of microscopy*, *254*(2), 75-83.

[150] Cazaux, J., Kuwano, N., & Sato, K. (2013). Backscattered electron imaging at low emerging angles: A physical approach to contrast in LVSEM. *Ultramicroscopy*, *135*, 43-49.

[151] Masters, R. C., Wan, Q., Zhou, Y., Sandu, A. M., Dapor, M., Zhang, H., ... & Rodenburg, C. (2015). Application of low-voltage backscattered electron imaging to the mapping of organic photovoltaic blend morphologies. In *Journal of Physics: Conference Series* (Vol. 644, No. 1, p. 012017). IOP Publishing.

[152] Garitagoitia Cid, A., Sedighi, M., Löffler, M., van Dorp, W. F., & Zschech, E. (2016). Energy-Filtered Backscattered Imaging Using Low-Voltage Scanning Electron Microscopy: Characterizing Blends of ZnPc–C60 for Organic Solar Cells. *Advanced Engineering Materials*, *18*(6), 913-917.

[153] Wandrol, P., Va 拧 ina, R., Sandu, A., Vesseur, E. J., & Tuma, L. (2016). Selective Detection of Backscattered Electrons in the Compound Lens Equipped UHR SEM. *Microscopy and Microanalysis*, *22*(S3), 576-577.

[154] Kim, K. W., & Jaksch, H. (2009). Compositional contrast of uncoated fungal spores and stained section-face by low-loss backscattered electron imaging. *Micron*, *40*(7), 724-729.

[155] Jaksch, H. (2011). The contrast mechanisms of LL-BSE electrons in FE-SEM characterization of polymer, single proteins, and oxidization states of elements. *Microscopy and Microanalysis*, *17*(S2), 902.

[156] Richards, R. G., Owen, G. R., & Ap Gwynn, I. (1999). Low voltage backscattered electron imaging (< 5 kV) using field emission scanning electron microscopy. *Scanning Microsc*, *13*(1), 55-60.

[157] Aoyama, T., Nagoshi, M., Nagano, H., Sato, K., & Tachibana, S. (2011). Selective backscattered electron imaging of material and channeling contrast in microstructures of scale on low carbon steel controlled by accelerating voltage and take-off angle. *ISIJ international*, *51*(9), 1487-1491.

[158] Wells, O. C. (1971). Low-loss image for surface scanning electron microscope. *Applied Physics Letters*, *19*(7), 232-235.

[159] Rau, E. I., Khursheed, A., Gostev, A. V., & Osterberg, M. (2002). Improvements to the design of an electrostatic toroidal backscattered electron spectrometer for the scanning electron microscope. *Review of scientific instruments*, *73*(1), 227-229.

[160] Reimer, L., Riepenhausen, M., & Schierjott, M. (1986). Signal of backscattered electrons at edges and surface steps in dependence on surface tilt and take-off direction. *Scanning*, *8*(4), 164-175.

[161] Müllerová, I., & Konvalina, I. (2007). Acquisition of the angular distribution of backscattered electrons at low energies. *Materials transactions*, *48*(5), 940-943.

[162] Cazaux, J., Kuwano, N., & Sato, K. (2013). Backscattered electron imaging at low emerging angles: A physical approach to contrast in LVSEM. *Ultramicroscopy*, *135*, 43-49.

[163] Halperin, A., Kröger, M., & Winnik, F. M. (2015). Poly (N-isopropylacrylamide) Phase Diagrams: Fifty Years of Research. *Angewandte Chemie International Edition*, *54*(51), 15342-15367.

[164]Ono, Y., & Shikata, T. (2006). Hydration and dynamic behavior of poly (N-isopropylacrylamide) s in aqueous solution: a sharp phase transition at the lower critical solution temperature. *Journal of the American Chemical Society*, *128*(31), 10030-10031.

[165] Heskins, M., & Guillet, J. E. (1968). Solution properties of poly (N-isopropylacrylamide). *Journal of Macromolecular Science—Chemistry*, *2*(8), 1441-1455.

[166] Schmidt, S., Motschmann, H., Hellweg, T., & von Klitzing, R. (2008). Thermoresponsive surfaces by spin-coating of PNIPAM-co-PAA microgels: A combined AFM and ellipsometry study. *Polymer*, *49*(3), 749-756.

[167] Varga, I., Gilányi, T., Meszaros, R., Filipcsei, G., & Zrínyi, M. (2001). Effect of cross-link density on the internal structure of poly (N-isopropylacrylamide) microgels. *The Journal of Physical Chemistry B*, *105*(38), 9071-9076.

[168] Ohya, S., & Matsuda, T. (2005). Poly (N-isopropylacrylamide)(PNIPAM)-grafted gelatin as thermoresponsive three-dimensional artificial extracellular matrix: molecular and formulation parameters vs. cell proliferation potential. *Journal of Biomaterials Science, Polymer Edition*, *16*(7), 809-827.

[169] Sun, S., & Wu, P. (2011). A one-step strategy for thermal-and pH-responsive graphene oxide interpenetrating polymer hydrogel networks. *Journal of Materials Chemistry*, *21*(12), 4095-4097.

[170] Karg, M., Pastoriza-Santos, I., Liz-Marzán, L. M., & Hellweg, T. (2006). A versatile approach for the preparation of thermosensitive PNIPAM core–shell microgels with nanoparticle cores. *ChemPhysChem*, *7*(11), 2298-2301.

[171] Sun, S., & Wu, P. (2011). A one-step strategy for thermal-and pH-responsive graphene oxide interpenetrating polymer hydrogel networks. *Journal of Materials Chemistry*, *21*(12), 4095-4097.

[172] Wong, J. E., Gaharwar, A. K., Müller-Schulte, D., Bahadur, D., & Richtering, W. (2008). Dual-stimuli responsive PNiPAM microgel achieved via layer-by-layer assembly: Magnetic and thermoresponsive. *Journal of colloid and interface science*, *324*(1), 47-54.

[173] Li, P. F., Xie, R., Jiang, J. C., Meng, T., Yang, M., Ju, X. J., ... & Chu, L. Y. (2009). Thermo-responsive gating membranes with controllable length and density of poly (N-isopropylacrylamide) chains grafted by ATRP method. *Journal of Membrane Science*, *337*(1), 310-317.

[174] Hebeish, A., Farag, S., Sharaf, S., & Shaheen, T. I. (2014). Thermal responsive hydrogels based on semi interpenetrating network of poly (NIPAm) and cellulose nanowhiskers. *Carbohydrate polymers*, *102*, 159-166.

[175] Zhang, J., & Ma, P. X. (2010). Host–guest interactions mediated nano-assemblies using cyclodextrin-containing hydrophilic polymers and their biomedical applications. *Nano Today*, *5*(4), 337-350.

[176] Zhou, H., Liu, F., Wang, X., Yan, H., Song, J., Ye, Q., ... & Xu, J. (2015). Aggregation induced emission based fluorescence pH and temperature sensors: probing polymer interactions in poly (N-isopropyl acrylamide-co-tetra (phenyl) ethene acrylate)/poly (methacrylic acid) interpenetrating polymer networks. *Journal of Materials Chemistry C*, *3*(21), 5490-5498.

[177] Radecki, M., Spěváček, J., Zhigunov, A., Sedláková, Z., & Hanyková, L. (2015). Temperature-induced phase transition in hydrogels of interpenetrating networks of poly (N-isopropylacrylamide) and polyacrylamide. *European Polymer Journal*, *68*, 68-79.

[178] He, Y., Geng, L., Tong, C., Liu, L., & Lü, C. (2014). Regulation of micromorphology and proton conductivity of sulfonated polyimide/crosslinked PNIPAm semi-interpenetrating networks by hydrogen bonding. *Polymer International*, *63*(10), 1806-1815.

[179] Schmaljohann, D. (2006). Thermo-and pH-responsive polymers in drug delivery. *Advanced drug delivery reviews*, *58*(15), 1655-1670.

[180] Schmidt, S., Zeiser, M., Hellweg, T., Duschl, C., Fery, A., & Möhwald, H. (2010). Adhesion and mechanical properties of PNIPAM microgel films and their potential use as switchable cell culture substrates. *Advanced Functional Materials*, *20*(19), 3235-3243.

[181] Guan, Y., & Zhang, Y. (2011). PNIPAM microgels for biomedical applications: from dispersed particles to 3D assemblies. *Soft Matter*, *7*(14), 6375-6384.

[182] Mondal, M. (2007). The silk proteins, sericin and fibroin in silkworm, Bombyx mori Linn.,-a review. *Caspian Journal of Environmental Sciences*, *5*(2), 63-76.

[183] Chu, K. Y., & Provost, J. R. (1987). The dyeing and printing of silk fabrics. *Coloration Technology*, *17*(1), 23-28.

[184] Shao, Z., & Vollrath, F. (2002). Materials: Surprising strength of silkworm silk. *Nature*, *418*(6899), 741-741.

[185] Etienne, O., Schneider, A., Kluge, J. A., Bellemin-Laponnaz, C., Polidori, C., Leisk, G. G., ... & Egles, C. (2009). Soft tissue augmentation using silk gels: an in vitro and in vivo study. *Journal of periodontology*, *80*(11), 1852-1858.

[186] Lawrence, B. D., Marchant, J. K., Pindrus, M. A., Omenetto, F. G., & Kaplan, D. L. (2009). Silk film biomaterials for cornea tissue engineering. *Biomaterials*, *30*(7), 1299-1308.

[187] Altman, G. H., Diaz, F., Jakuba, C., Calabro, T., Horan, R. L., Chen, J., ... & Kaplan, D. L. (2003). Silk-based biomaterials. *Biomaterials*, *24*(3), 401-416.

[188] Cai, Z. X., Mo, X. M., Zhang, K. H., Fan, L. P., Yin, A. L., He, C. L., & Wang, H. S. (2010). Fabrication of chitosan/silk fibroin composite nanofibers for wound-dressing applications. *International journal of molecular sciences*, *11*(9), 3529-3539.

[189] Hofmann, S., Foo, C. W. P., Rossetti, F., Textor, M., Vunjak-Novakovic, G., Kaplan, D. L., ... & Meinel, L. (2006). Silk fibroin as an organic polymer for controlled drug delivery. *Journal of Controlled Release*, *111*(1), 219-227.

[190] Kujala, S., Mannila, A., Karvonen, L., Kieu, K., & Sun, Z. (2016). Natural silk as a photonics component: A study on its light guiding and nonlinear optical properties. *Scientific reports*, *6*, 22358.

[191] Qian, J., Liu, Y., Liu, H., Yu, T., & Deng, J. (1997). Immobilization of horseradish peroxidase with a regenerated silk fibroin membrane and its application to a tetrathiafulvalene-mediating H 2 O 2 sensor. *Biosensors and Bioelectronics*, *12*(12), 1213-1218.

[192] Simmons, A. H., Michal, C. A., & Jelinski, L. W. (1996). Molecular orientation and two-component nature of the crystalline fraction of spider dragline silk. *Science*, *271*(5245), 84-87.

[193] Lakes, R. (1993). Materials with structural hierarchy. *Nature*, *361*(6412), 511-515.

[194] Fratzl, P., & Weinkamer, R. (2007). Nature's hierarchical materials. *Progress in Materials Science*, *52*(8), 1263-1334.

[195] Thiel, B. L., Guess, K. B., & Viney, C. (1997). Non-periodic lattice crystals in the hierarchical microstructure of spider (major ampullate) silk. *Biopolymers*, *41*(7), 703-719.

[196] Hayashi, C. Y., Shipley, N. H., & Lewis, R. V. (1999). Hypotheses that correlate the sequence, structure, and mechanical properties of spider silk proteins. *International Journal of Biological Macromolecules*, *24*(2), 271-275.

[197] Asakura, T., Yang, M., Kawase, T., & Nakazawa, Y. (2005). 13C Solid-State NMR Study of Structural Heterogeneity in Peptides Containing Both Polyalanine and Repeated GGA Sequences as a Local Structural Model of Nephila c lavipes Dragline Silk (Spidroin 1). *Macromolecules*, *38*(8), 3356-3363.

[198] Sponner, A., Unger, E., Grosse, F., & Weisshart, K. (2005). Differential polymerization of the two main protein components of dragline silk during fibre spinning. *Nature materials*, *4*(10), 772.

[199] Willcox, P. J., Gido, S. P., Muller, W., & Kaplan, D. L. (1996). Evidence of a cholesteric liquid crystalline phase in natural silk spinning processes. *Macromolecules*, *29*(15), 5106-5110.

[200] Grubb, D. T., & Ji, G. (1999). Molecular chain orientation in supercontracted and re-extended spider silk. *International journal of biological macromolecules*, *24*(2), 203-210.

[201] Asakura, T., Ashida, J., Yamane, T., Kameda, T., Nakazawa, Y., Ohgo, K., & Komatsu, K. (2001). A repeated β-turn structure in poly (Ala-Gly) as a model for silk I of Bombyx mori silk fibroin studied with two-dimensional spin-diffusion NMR under off magic angle spinning and rotational echo double resonance. *Journal of molecular biology*, *306*(2), 291-305.

[202] Liu, Y., Shao, Z., & Vollrath, F. (2005). Relationships between supercontraction and mechanical properties of spider silk. *Nature materials*, *4*(12), 901.

[203] Um, I. C., Ki, C. S., Kweon, H., Lee, K. G., Ihm, D. W., & Park, Y. H. (2004). Wet spinning of silk polymer: II. Effect of drawing on the structural characteristics and properties of filament. *International journal of biological macromolecules*, *34*(1), 107-119.

[204] Putthanarat, S., Stribeck, N., Fossey, S. A., Eby, R. K., & Adams, W. W. (2000). Investigation of the nanofibrils of silk fibers. *Polymer*, *41*(21), 7735-7747.

[205] Zhang, F., Lu, Q., Ming, J., Dou, H., Liu, Z., Zuo, B., ... & Zhang, X. (2014). Silk dissolution and regeneration at the nanofibril scale. *Journal of Materials Chemistry B*, *2*(24), 3879-3885.

[206] Keten, S., Xu, Z., Ihle, B., & Buehler, M. J. (2010). Nanoconfinement controls stiffness, strength and mechanical toughness of [beta]-sheet crystals in silk. *Nature materials*, *9*(4), 359.

[207] Keten, S., Xu, Z., Ihle, B., & Buehler, M. J. (2010). Nanoconfinement controls stiffness, strength and mechanical toughness of [beta]-sheet crystals in silk. *Nature materials*, *9*(4), 359.

[208] Nova, A., Keten, S., Pugno, N. M., Redaelli, A., & Buehler, M. J. (2010). Molecular and nanostructural mechanisms of deformation, strength and toughness of spider silk fibrils. *Nano Letters*, *10*(7), 2626-2634.

[209] Vollrath, F., Madsen, B., & Shao, Z. (2001). The effect of spinning conditions on the mechanics of a spider's dragline silk. *Proceedings of the Royal Society of London B: Biological Sciences*, *268*(1483), 2339-2346.

[210] Vollrath, F., & Knight, D. P. (2001). Liquid crystalline spinning of spider silk. *Nature*, *410*(6828), 541.

[211] Kumar, V., Schmidt, W. L., Schileo, G., Masters, R. C., Wong-Stringer, M., Sinclair, D. C., ... & Rodenburg, C. (2017). Nanoscale Mapping of Bromide Segregation on the Cross Sections of Complex Hybrid Perovskite Photovoltaic Films Using Secondary Electron Hyperspectral Imaging in a Scanning Electron Microscope. *ACS Omega*, *2*(5), 2126-2133.

[212] Sionkowska, A., & Planecka, A. (2011). The influence of UV radiation on silk fibroin. *Polymer degradation and stability*, *96*(4), 523-528.

[213] Schniepp, H. C., Koebley, S. R., & Vollrath, F. (2013). Brown recluse spider's nanometer scale ribbons of stiff extensible silk. *Advanced Materials*, *25*(48), 7028-7032.

[214] Brown, C. P., MacLeod, J., Amenitsch, H., Cacho-Nerin, F., Gill, H. S., Price, A. J., ... & Rosei, F. (2011). The critical role of water in spider silk and its consequence for protein mechanics. *Nanoscale*, *3*(9), 3805-3811.

[215] Gonzalez, L. A., Larciprete, R., Cimino, R. (2016), The effect of structural disorder on the secondary electron emission of graphite. *AIP Advances*, *6*, 095117

[216] Breslauer, D. N., Lee, L. P., & Muller, S. J. (2008). Simulation of flow in the silk gland. *Biomacromolecules*, *10*(1), 49-57.

[218] Agnarsson, I., Boutry, C., & Blackledge, T. A. (2008). Spider silk aging: initial improvement in a high performance material followed by slow degradation. *Journal of Experimental Zoology Part A: Ecological Genetics and Physiology*, *309*(8), 494-504.

[219] Liu, Y., Shao, Z., & Vollrath, F. (2005). Relationships between supercontraction and mechanical properties of spider silk. *Nature materials*, *4*(12), 901.

[220] Jelinski, L. W., Blye, A., Liivak, O., Michal, C., LaVerde, G., Seidel, A., ... & Yang, Z. (1999). Orientation, structure, wet-spinning, and molecular basis for supercontraction of spider dragline silk. *International Journal of Biological Macromolecules*, *24*(2), 197-201.